Local interaction of light
with
periodic photonic structures

Samenstelling van de promotiecommissie:

prof.dr. P.J. Gellings (voorzitter)	University of Twente
prof.dr. N.F. van Hulst	University of Twente
prof.dr. L. Kuipers	University of Twente
prof.dr. A. Dereux	University of Bourgogne
prof.dr. T.F. Krauss	University of St. Andrews
prof.dr. W.L. Vos	University of Twente
prof.dr.ing. D.H.A. Blank	University of Twente
prof.dr. K.J. Boller	University of Twente

ISBN: 90-365-1929-2

Printed in the Netherlands

LOCAL INTERACTION OF LIGHT WITH PERIODIC PHOTONIC STRUCTURES

PROEFSCHRIFT

ter verkrijging van
de graad van doctor aan de Universiteit Twente,
op gezag van de rector magnificus,
prof.dr. F.A. van Vught,
volgens besluit van het College voor Promoties
in het openbaar te verdedigen
op vrijdag 20 juni 2003 om 15.00 uur

door

Eliane Flück

geboren op 5 juni 1973
te Zürich, Zwitserland

Dit proefschrift is goedgekeurd door:

promotor: prof.dr. N.F. van Hulst
promotor: prof.dr. L. Kuipers

Contents

Introduction

In this thesis we will take a detailed look inside a novel type of optical materials, photonic crystal structures, using near-field optical techniques.

Although the concept of near-field optics was already proposed in 1928, experiments only became possible after the invention of scanning probe microscopy in the eighties. Bringing a sharp tapered probe, with a sub-wavelength aperture at its nanometric apex, in close proximity to a sample allows imaging with an optical resolution better than the diffraction limit. As a result, it becomes possible to study the local properties of light inside optical structures. A good introduction to the wide area of applications and into the different instrumental approaches can be found in a *J. Microscopy* (e.g., [1], [2]) and in the book *Nano-optics* by Kawata [3].

Photonic crystals are one-, two- or three-dimensional composites of periodically alternated dielectric materials. The periodicity has to be of the order of the relevant wavelengths. The typical character of such a composite is that light of a certain range of frequencies cannot propagate along certain directions inside the crystal. The forbidden ranges are called stopgaps. In multi-dimensional crystals, stopgaps along different crystalline directions can overlap. When an overlap exists in all possible crystalline directions for a certain range of optical frequencies, this resulting forbidden range of frequencies is called the photonic bandgap. The photonic bandgap strongly affect the optical properties of the crystal. Defects introduced on purpose into a photonic crystal can result in a localised photon state inside the stop- or bandgap. A point defect can thus act as a high-quality resonator and a line defect can be used as an optical waveguide. The existence of a photonic bandgap in three-dimensional crystals will eliminate quantum vacuum fluctuations at the frequencies in the gap. A wide review of theoretical and experimental results can be found in the books of Joannopoulos [4], Sakoda [5] and in a recent Nato Conference Proceedings [6].

The high potential of interesting quantum physics and the exciting possible applications of photonic crystals has motivated researchers to investigate a huge variety of ideas. Some promising highlights of the field are investigations on trapped photons in a two-dimensional photonic crystal [7], control over spontaneous emission of laser dyes located inside three-dimensional air-sphere crystals [8], highly efficient LED's [9] and white light generation in photonic fibres [10].

The subtle manipulation of optical interference effects is crucial in photonic crystals. As a result small variations, intended or not, in the geometry result in large effects on the light propagation. It is therefore desirable to investigate the nanoscale local optical properties inside the structure and directly relate them to the geometry. Conventional far-field methods, such as reflectivity and transmission experiments only provide global averaged information. In contrast, a near-field optical microscope has the potential to reveal local details on the relevant length scale. The insights gained will help to understand the complex materials better and to optimise the crystal design in the near future.

In this thesis we present different approaches to investigate photonic crystals. Near-field optical microscopy as well as far-field reflectivity investigations reveal interesting and novel details of photonic crystal structures. Local phase-sensitive measurements are performed on one-dimensional structures. Losses of the structure are determined and networks of phase singularities are observed. For the first time, the reversal of dispersive line shapes of resonance features, occurring in the reflectivity spectra obtained on two-dimensional photonic crystal slabs, is observed and analysed. Moreover, we present the first near-field investigations on three-dimensional photonic crystals. The coupling of light coming from the fibre probe to the crystal indicates effects related to intricate photonic stopgaps.

Outline of this Thesis

In chapter 1, a theoretical introduction on photonic crystals is given. The dispersion relation, which describes the optical properties of a photonic crystal, is discussed for the one-, two- and three-dimensional case. In the second part of the chapter, we discuss the processes used for fabrication of the investigated one-, two- and three-dimensional structures. The material details and the geometrical dimensions of these structures are presented.

In chapter 2, the different far-field and near-field characterisation methods that have been used are explained. First, technical details on the near-field probe fabrication are discussed. Then, a photon scanning tunnelling microscope (PSTM), which is a near-field scanning optical microscope (NSOM) in collection mode, and a NSOM in illumination mode are elucidated. Both measurement setups are equipped with a three-dimensional measurement mode. In the second part of the chapter far-field reflectivity is briefly discussed. To understand the measurements on resonant modes of a photonic crystal slab, we explain the technique of specular reflectivity (angle-dependent reflectivity) measurements and the physical principle of the interaction of light with the crystal structure.

Different one-dimensional photonic structures are investigated with a PSTM and the results are presented in chapter 3. The technique allows not only probing of the optical amplitude of light, but simultaneously detects the phase information of light. We discuss the evolution of scattered light and phase singularities.

Chapter 4 deals with far-field investigations on two-dimensional photonic crystal slabs. First, the stopgaps are determined with in-plane reflectivity measurements. Then, angle-dependent reflectivity spectra are obtained to determine the dispersion of resonant modes. We also investigate the line shapes of the resonance features in detail.

In chapter 5, near-field investigations on three-dimensional photonic crystals are presented. For different optical frequencies we investigate the coupling of light from a near-field probe through a crystal. We present the effect of surface defects on the light transfer. Moreover, approach curves obtained on the opals for different optical frequencies indicate the presence of the first order Γ - L stopgap.

Chapter 1

Photonic crystal structures

Photonic crystals should enable the possibility of designed guiding of light or inhibiting the spontaneous emission of fluorescent molecules. Controlling the propagation of light or manipulating the emission properties of a light emitter with photonic crystal structures has many novel, high-potential applications, e.g., low threshold lasers or miniaturised all optical circuits. In this chapter, we give a short introduction on the principle of photonic crystals. Afterwards, the specific photonic crystal structures investigated in this thesis are discussed theoretically. In the second part of this chapter, fabrication methods used to create the photonic crystal structures are explained and details concerning the investigated crystals are provided.

1.1 Theoretical aspects

Photonic crystals offer a huge potential for applications, since they enable the control and manipulation of light. On purpose designed defects allow tailoring the light propagation. In a one-dimensional structure, a defect state acts as a bandpass filter [11]. For two- and three-dimensional crystals, point defects act as high-quality resonators [12], whereas line defects guide light of the allowed optical states through the crystal [13]. Especially this unique possibility to control light has encouraged a large research activity that aims for a miniaturisation and optimisation of integrated optics and telecommunication networks [14], [15].

Some selected examples to illustrate the exciting physics and important applications are, e.g., the superprism phenomena in planar photonic crystal [16], which should enable wavelength-division multiplexing or white light generation in photonic fibres that will provide new light sources [10]. Moreover, highly efficient LED's can be fabricated [9]. It is obvious that the photonic crystal are promising new materials, which merit exploration in greater detail.

1.1.1 General introduction

When light interacts with materials of different refractive indices scattering and diffraction occurs. If the variation of the refractive indices is periodic (in one-, two- or three-dimensions) light reflected from a set of parallel planes can interfere constructively, which is called Bragg-diffraction. A composite of different periodically arranged dielectrics is called a photonic crystal, if the periodicity is of the order of the wavelength of light [6], [17], [18], [19].

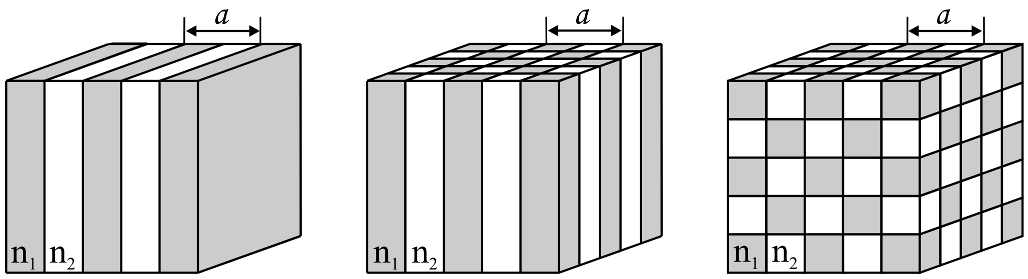

Figure 1.1: Schematic illustrations of one-, two- and three-dimensional photonic crystals. The crystals consist of two different dielectric materials with refractive indices n_1 and n_2. The period a of the arrangements is proportional to half of the wavelength of interest, thus on the sub-wavelength scale.

Figure 1.1 depicts schematically examples of one-, two- and three-dimensional photonic crystals. The sketch on the left side shows a one-dimensional crystal consisting of dielectric planes of two different refractive indices n_1 and n_2, which are alternated with a period a. If a second periodic variation is introduced, as shown in the sketch in the middle of Fig. 1.1, the crystal is two-dimensional. In the representation on the right side, a three-dimensional crystal with periodicity in all three dimensions is depicted. For such periodic composites of different materials light of certain frequencies is forbidden to propagate along certain directions in the crystal. In the following we illustrate the theoretical description of the presence of such a stopgap for a one-dimensional example.

The optical properties of a photonic crystal are described by the dispersion relation that expresses the optical frequency ω as a function of the wavevector k of the propagating waves in the material. For a homogeneous dielectric material (dielectric constant ε), the dispersion of light is a straight line given by

$$\omega = \frac{c}{\sqrt{\epsilon}} \cdot k \ , \tag{1.1}$$

where c is speed of light in vacuum. Note that in general the dielectric constant is frequency dependent: $\varepsilon = \varepsilon(\omega)$. By introducing a periodic refractive index variation to the material, the dispersion relation is greatly affected. Figure 1.2 depicts schematically both the dispersion of a homogeneous material and the dispersion of a one-dimensional photonic crystal. On the vertical axis the dimensionless frequency ω is given in units of $[\frac{2\pi c}{a}]$. On the horizontal axis, the wavevector k is given in units $[\frac{2\pi}{a}]$. The dispersion of the one-dimensional photonic crystal shows a curvature around the wavevector 0.5 (the edge of the Brillouin zone [20], [21]). There, a gap of frequencies opens up, for which no corresponding real wavevector can be found. Light of these frequencies cannot propagate in the crystal. The corresponding wavevectors have only an imaginary part and thus decay exponentially inside the crystal. These range of frequencies, which cannot propagate and are forbidden, is called a stopgap. For multi-dimensional crystals, stopgaps can exist along several directions. When stopgaps along all the various crystalline directions overlap, a photonic bandgap is present, for which the optical frequencies are forbidden in all directions.

The refractive index $\mathrm{n} = \sqrt{\varepsilon}$ of a material is given by the slope of the dashed line in the dispersion relation (Eq. 1.1). For a photonic crystal, the refractive index changes when approaching the Brillouin zone edge. An increase of the refractive index is found at the low frequency side of the stopgap. There, the power of the E-field is located mainly in the high index material. At the high frequency side of the stopgap, a decrease in refractive index implies that the power of the E-field is mainly present in the low index material. For a photonic crystal a good

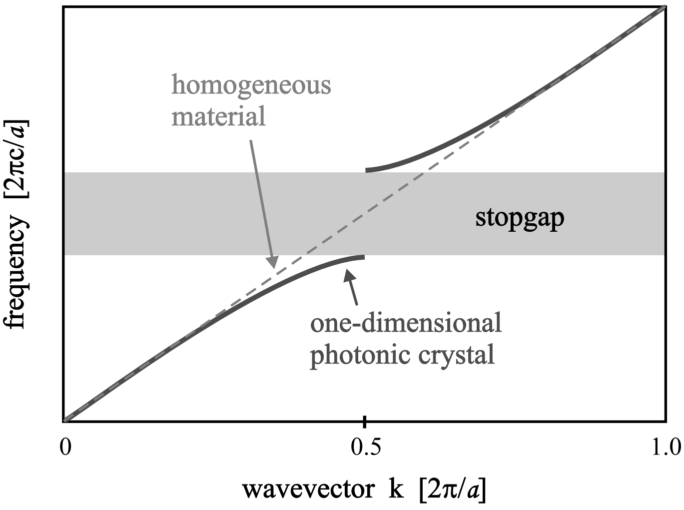

Figure 1.2: Schematic representation of a dispersion relation of a homogeneous dielectric material with a refractive index n and of an infinitive one-dimensional photonic crystal with an effective refractive index of n. The slope of the dashed line is 1 / n. For the photonic crystal, the bands curve at the edge of the Brillouin zone and a stopgap, a gap of forbidden frequencies, opens up. Frequencies lying in the stopgap have a purely imaginary wavevector, the real part of the wavevector is zero. Thus, light of this frequencies is evanescent and decays exponentially into the crystal.

approximation for the effective refractive index is

$$\varepsilon_{eff} = \phi_1 \cdot \varepsilon_1 + \phi_2 \cdot \varepsilon_2 \ , \tag{1.2}$$

where ϕ_1 is the volume fraction of the high index material of a dielectric constant ε_1, and ϕ_2 is the volume fraction of the low index material of a dielectric constant ε_2. The assumption of an effective refractive index reduces the crystal to a homogeneous material of the effective dielectric constant ε_{eff}. With ε_{eff}, the centre frequency of the stopgap can be calculated [22]. Mostly, this approach provides a first step to design a photonic crystal.

Photonic crystals attract a lot of interest, since they offer the potential of a huge control over light. Propagation control is achieved by deliberate introduction of defects into the perfectly periodic crystal. As a result, a highly localised frequency state appears in the forbidden range of the stop- or bandgap. An array of defects should in principle transmit light of the localised frequency state without any losses, as the light is forbidden elsewhere in the crystal. Moreover, the complete lack of photon states in the bandgap of a photonic crystals can be used to control spontaneous emission of an emitter inside the crystal [23]. If the emission wavelength lies within the photonic bandgap, inhibition of emission takes place.

1.1.2 Two-dimensional photonic crystal slabs

A photonic crystal slab consists of a guiding layer of a high index material that confines light in the z-direction by total internal reflection. Into this slab, a periodic variation between two dielectric materials is introduced, e.g., by drilling a square or triangular lattice of air rods. Figure 1.3 schematically depicts a photonic crystal slab, which consists of a dielectric slab surrounded by air that contains an arrangement of air rods. In contrast to the two-dimensional photonic crystal depicted in Fig. 1.1, the photonic crystal slab is not infinitely extended in the z-direction. For such a special case of a two-dimensional photonic crystal with a triangular lattice of air rods, the calculated dispersion relation is depicted in Fig. 1.4. The inset shows the crystal lattice in real space (left) and the different crystalline directions along the symmetry axis in the reciprocal space (right). The points Γ, M and K are the centre and end points of the first Brillouin zone, respectively. The parameters of the crystal used for this calculation are the periodicity a, the radius of the air rods $\mathrm{r} = 0.32{\cdot}a$ and the thickness of the slab $\mathrm{h} = 0.35{\cdot}a$. For the slab material, a dielectric constant of $\varepsilon = 4.6656$ was used, which corresponds to silicon-rich silicon nitride (Si_3N_4), as was used for the fabrication of the photonic crystal slabs investigated in chapter 4.

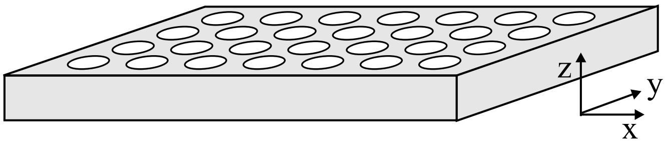

Figure 1.3: Two-dimensional photonic crystal slab consisting of a dielectric slab in which a lattice of air rods is introduced. If the slab is suspended in air the highest possible index contrast is achieved.

The modes of the dispersion relation are represented in two different ways, by open circles for even modes and by filled dots for odd modes. Translational symmetry is found inside the slab (x- and y-direction). This translational symmetry is broken in the z-direction due to the existence of the slab. There, a symmetry axis for mirror symmetry bisects the slab. The labelling of the modes (even and odd) is defined by a mirror symmetry argument applied to the polarisation of the light

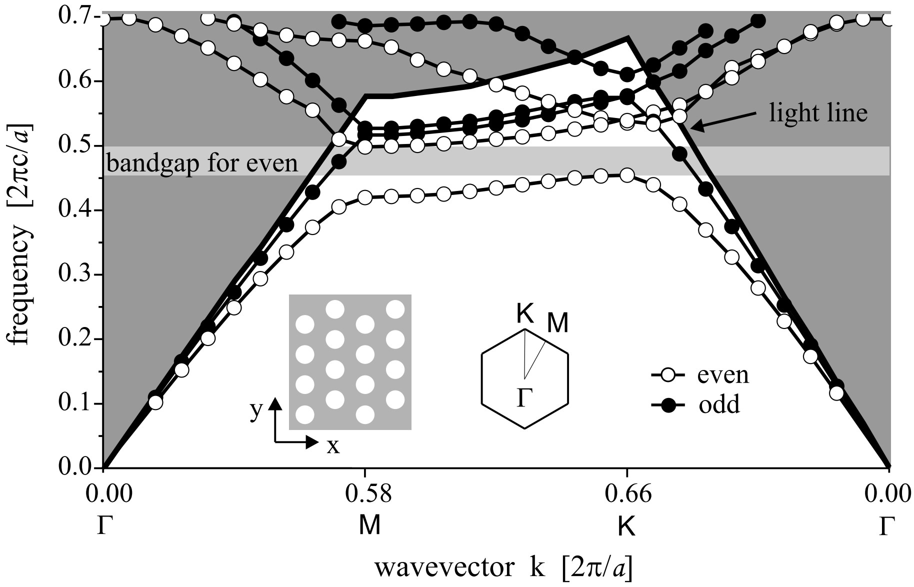

Figure 1.4: Calculated dispersion relation for a two-dimensional photonic crystal slab as shown in Fig. 1.3. The inset depicts the real space lattice and the Brillouin zone in reciprocal space. Γ, M and K are the high symmetry points of the Brillouin zone along the main crystallographic directions. The so-called light line gives the border between guided light in the slab and non-guided light. For this three-dimensional finite difference time domain calculation a dielectric constant $\epsilon = 4.6656$ is used. The triangular lattice has a period a and the radius of the air rods is $r = 0.32 \cdot a$. The thickness of the slab is $h = 0.35 \cdot a$.

in the z-direction. Even modes show a mirror symmetric polarisation distribution within the amplitude mode profile of the field and odd modes an asymmetric mode profile. As a result, the zero order modes of the slab of transverse electric (TE) polarised light correspond to the even modes, where the electric field component lies within the slab plane (x-y plane). The transverse magnetic (TM) polarised light, corresponds to the odd modes, with the magnetic field component in the x-y plane.

The existence of the slab has other consequences as well. In the slab, light is confined by index guiding in the z-direction. Outside of the slab, a continuum of modes (shadowed area) is present. A black line, called the light line, represents the border between guided light (below the light line) and the continuum and the non-guided light (above the light line) of the slab. The bands of even and odd modes that are located in the continuum can couple to modes of the continuum and are therefore called resonant modes (also called leaky modes). Those modes can be accessed directly by far-field methods from above or below the slab and are topic of the investigations in section 4.1.2. The properties of guided modes below the light line can be investigated by far-field reflection or transmission measurements performed in the plane of the slab. The nature of these modes is an interesting topic for local investigations performed, e.g., with near-field methods.

From the calculations shown in Fig. 1.4, we find the following relevant stopgaps and a bandgap. A two-dimensional bandgap is calculated for frequencies between 0.45 and 0.50 for even modes and indicated by a light gray region. Along the Γ - K direction a stopgap is present ranging from 0.45 to 0.53. For the Γ - M direction a stopgap is found between 0.42 and 0.50. For odd modes the calculated stopgap in the Γ - M direction ranges from 0.52 to 0.53 and along the Γ - K direction from 0.57 to 0.61.

1.1.3 Three-dimensional photonic crystals

The three-dimensional photonic crystals investigated in this thesis consist of polystyrene spheres. The arrangement of the spheres is a close-packed hexagonal order, which is in our case a face centred cubic (fcc) lattice of a volume fraction $\phi_{polystyrene} = 0.74$. Figure 1.5 depicts the band diagram calculated for such polystyrene opals. The calculations have been done with a H-field inverted matrix method [24], [25]. The inset on the right side depicts the Brillouin zone of the fcc lattice and its high symmetry points [21]. The calculation show various stopgaps along different crystalline directions. We determine a first order stopgap along Γ - L that ranges from 0.58 - 0.62 in frequency. For the crystalline Γ - U (symmetry equivalent to Γ - K) direction, a stopgap between 0.70 and 0.77 is found. For the Γ - W direction a stopgap for frequencies between 0.74 and 0.82 is determined. In the Γ - L direction, a range of second order Bragg diffraction is indicated by a gray area in Fig. 1.5. The corresponding frequency range from 1.13 to 1.24 is delimited by bands with a lope roughly equal to the average index n_{eff}.

1.2 Fabrication of photonic structures

The fabrication of photonic crystals has improved rapidly. For one- and two-dimensional crystals, mostly lithographic methods are used. Very flexible approaches are direct sequential writing with e-beam [26] or direct writing with a focused ion beam (see chapter 1.2.1). These two methods give the highest flexibility in the design as any arbitrary feature shape can easily be implemented. However, for the purpose of large one- and two-dimensional structures, methods like X-ray lithography [27], deep UV lithography [28] or laser interference lithography [29]

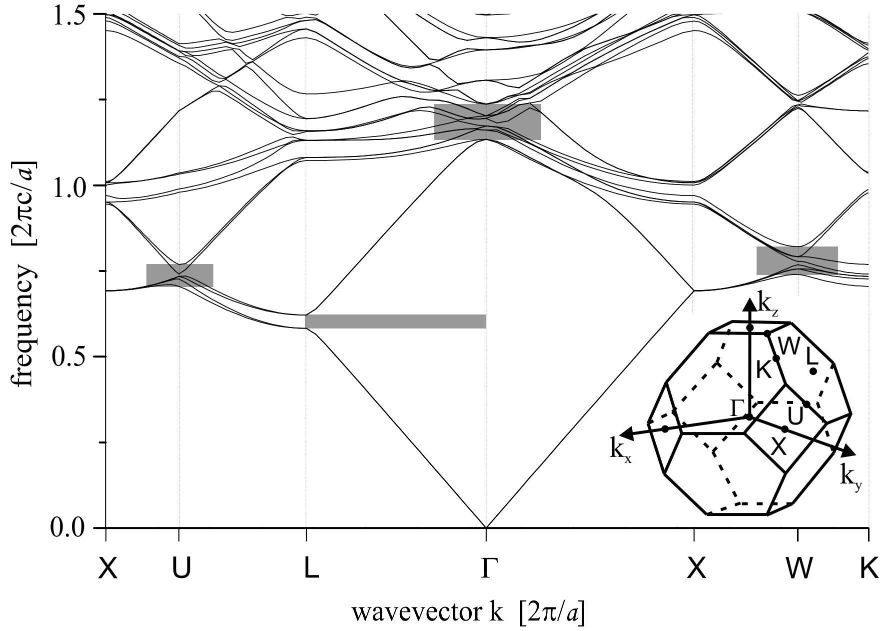

Figure 1.5: Calculated dispersion relation for a three-dimensional artificial opal of polystyrene spheres. The spheres are arranged in a face centred cubic (fcc) lattice and close-packed with a volume fraction of 74 %. As dielectric constant for polystyrene $\varepsilon = 2.53$ was used. The inset shows the fcc unit cell in reciprocal space for such a crystal. The gray areas indicate stopgaps along different crystalline directions.

are more appropriate. For the design of three-dimensional structures lithographic methods are available as well [19], [30]. However, holographic methods [31] or self-assembling processes are less time consuming (e.g., [18], [32] and [33]).

To control the flow of light, defects have to be introduced on purpose. This is easiest for one- and two-dimensional crystals and more difficult in a three-dimensional crystal, where work is in progress [34]. The materials used for photonic crystals are mainly dielectrics to reduce absorption as much as possible, since a photonic bandgap results from multiple scattering. Some more exotic crystals are made of magnetically active material [35] or carbon nanotubes [36]. An other way to modulate light in waveguides are plasmonic structures (e.g., [37], and references therein). Small metal particles on waveguides offer an alternative to the photonic crystal air rod structures.

1.2.1 One-dimensional periodic arrays fabricated with focused ion beam milling

For the fabrication of one-dimensional periodic structures on the nanometre scale a fast and flexible approach is described in this section. As a basis for all structures investigated in chapter 3, we us a silicon-nitride (Si_3N_4) channel waveguide on top of a 3.2 μm SiO_2 layer on a Si-substrate. The 55 nm thick Si_3N_4 layer is deposited by low-pressure chemical vapour deposition (LPCVD). By reactive ion etching (RIE) a waveguide ridge is etched into the Si_3N_4 layer with a height and width of 11 nm and 1.5 μm, respectively. Thus, a slab layer of 44 nm thickness surrounds the waveguide ridge. Figure 1.6 depicts the cross-section of the waveguide structure used.

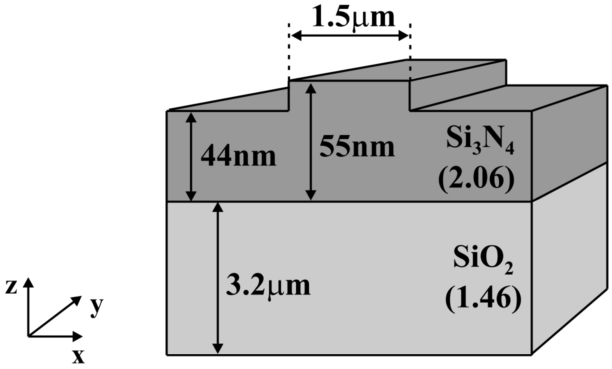

Figure 1.6: Illustration of the cross-section of the channel waveguide, which is used as a basis of all our one-dimensional photonic crystal structures. The guiding layer is silicon-nitrice (Si_3N_4), which is grown on top of a siliondioxide SiO_2 layer. The geometrical dimensions and the refractive indices of the material are given in the figure.

With a focused ion beam machine (FIB, 200 FEI) we have fabricated nanometer-size structures in the channel waveguides. Gallium-ions of an energy of 30 keV are used to sputter material from the sample. The beam current can be varied in discrete steps between 1 pA and 70 pA. Different structures have been fabricated of arbitrary shapes. The structures discussed in this thesis consist of nanometer scale air rods and slits. The smallest possible feature that can be fabricated in these waveguides was found to be an air rod of 30 nm in diameter.

Figure 1.7 shows two examples of structures produced with the FIB. The images were obtained by scanning electron microscopy (SEM), to prevent unintentional damage that results from imaging with the FIB. In both images, the channel waveguide, running in the vertical direction, is clearly visible. Figure 1.7 a shows

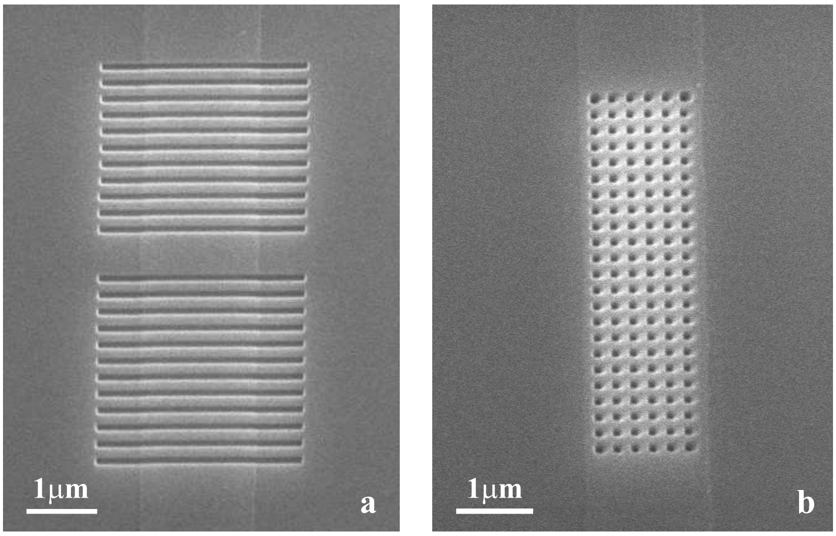

Figure 1.7: Two examples of periodic structures fabricated by focus ion beam milling in a Si_3N_4 channel waveguide. a) 23 slits in a periodic array, where two slits are missing in the centre of the array. The missing slits represents a cavity in the periodic structure, where light can be localised. b) Quasi-two dimensional structure of an array of 138 air rods.

a periodic arrangement ($a = 220\,\mathrm{nm}$) of slits ($110\,\mathrm{nm} \times 3.0\,\mu\mathrm{m}$). In the centre of the array, a defect is introduced by leaving two slits out. Figure 1.7 b shows a quasi-two dimensional photonic structure, where a two-dimensional array of 138 air rods (diameter $\mathrm{d} = 110\,\mathrm{nm}$) is milled into the waveguide. The two examples highlight the flexibility of the FIB technique as any desired feature shape as well as any periodic arrangement can be fabricated.

It turns out that the minimal size of the fabricated features in Si_3N_4 is not determined by the focal spot size of the FIB ($\sim 8\,\mathrm{nm}$), but rather by charging of the non-conducting Si_3N_4 layer. As a result, increasing the milling time results in larger feature sizes. To prevent the charging, a thin conducting carbon layer ($\sim 20\,\mathrm{nm}$) was deposited on top of the Si_3N_4 before milling. The carbon was removed afterwards by Oxygen-plasma etching.

A single slit in a waveguide was fabricated using a beam current of 4 pA and an exposure time of 57 s. The slit has a width of 160 nm and a length of $1.8\,\mu\mathrm{m}$. This slit is investigated in section 3.1.1 using a near-field technique. In section 3.1.2 two different periodic structures are investigated: a ridge waveguide containing 15 air rods and a ridge waveguide containing an array of 15 slits. Figure 1.8 shows the periodic array of air rods. Both arrays, the air rods and the slits, are designed

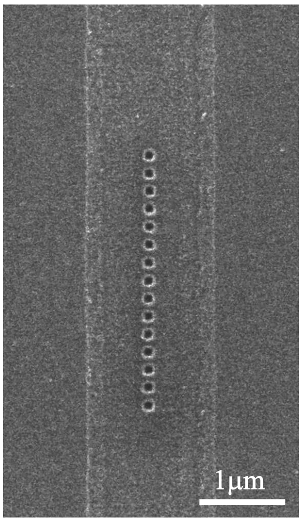

Figure 1.8: Array of 15 air rods milled into the centre of a waveguide ridge. The diameter of the air rods is 110 nm and the periodicity of the array 220 nm.

with a periodicity of $a = 220$ nm. The diameter of the air rods is 110 nm. The slits are 110 nm wide and 2.5 μm long. In both cases, the milling was performed such, that the feature depth is approximately 70 nm. The high-index Si_3N_4 layer of 55 nm is therefore penetrated completely.

1.2.2 Freestanding two-dimensional photonic crystal slabs produced by laser interference lithography

The two-dimensional photonic crystal slabs presented here are freestanding membranes produced by laser interference lithography [29]. Quite often, the index contrast between guiding layer and the surrounding lower index medium is not high enough to achieve large stopgaps. By embedding the guiding layer in air, the highest possible index contrast is achieved.Fabrication of an extended freestanding photonic crystal slab is challenging, since the slab must be connected to supports and the material of the slab must be stiff enough to prevent collapse. Fig. 1.9 shows a schematic of such a crystal slab.

The basis for the photonic crystal slab is a three layer composite. A silicon-rich silicon nitride (Si_3N_4) layer is deposited by low-pressure chemical vapour deposition (LPCVD) on a thermally grown, 3.2 μm thick SiO_2 layer on top of a Si-wafer. The slightly increased Si concentration reduces the stress in the layer and increases

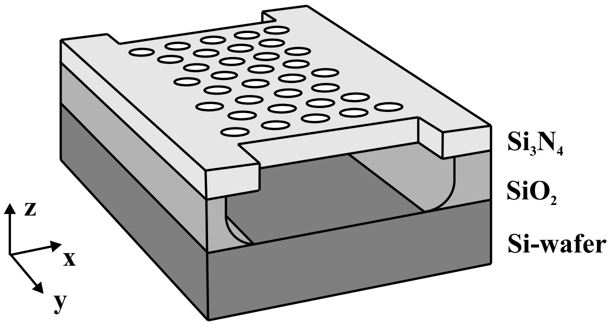

Figure 1.9: Schematic drawing of the photonic crystal slab. A triangular pattern of air rods is etched into a Si$_3$N$_4$ layer. An air gap underneath the Si$_3$N$_4$ layer ensures symmetry of the structure in the z-direction.

the resistance of the membrane against collapse. With laser interference lithography, a triangular pattern of dots is developed in a photoresist layer on top of the Si$_3$N$_4$ layer. The pattern of the photoresist dots is transferred into a chromium mask via lift-off and subsequently etched into the Si$_3$N$_4$ layer by reactive ion etching. The air rods in the Si$_3$N$_4$ allows the production of an air gap underneath the guiding layer through wet etching such that a freestanding membrane results.

The Si$_3$N$_4$ slab has a refractive index of $\mathrm{n} = 2.16$ ($\varepsilon = 4.6656$) at $\lambda_0 = 600\,\mathrm{nm}$. For the fabrication of the membrane investigated in chapter 4 the following design parameters were used. The thickness of the Si$_3$N$_4$ layer is 120 nm. The width and length of the photonic crystal are $100\,\mu$m and 4 mm, respectively. The air gap underneath the Si$_3$N$_4$ layer is $3.2\,\mu$m corresponding to the thickness of the SiO$_2$ layer. The triangular lattice of air rods has a lattice parameter of $a = 343\,\mathrm{nm}$. The fabricated air rods have an elliptical shape with a long axis and short axis of 125 nm and 93 nm, respectively. The long axis points into one of the Γ - M direction. This asymmetry leads, in principle, to a more complex unit cell. However, the influence on the band diagram and the gap size was calculated and determined to be small.

Figure 1.10 depicts a SEM image of the photonic crystal slab performed under an angle to show both the top and the side view. The triangular arrangement of the air rods is clearly visible. Note, that the SEM image shows only a small fraction of the membrane (< 0.2 ‰). It can be seen that the membrane is connected directly to the support, which separates the membrane by $3.2\,\mu$m from the Si-wafer in the z-direction. The photonic crystal slab does not extend all the way to the support. The final $\sim 7\,\mu$m of the membrane is free of holes due to under etching effects. The end facet of the membrane runs along the Γ - M direction of the hexagonal air rod pattern. The membrane ends $\sim 50\,\mu$m before the wafer ends.

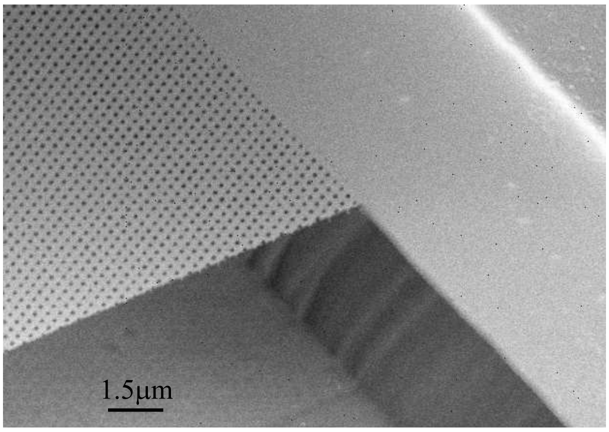

Figure 1.10: SEM image of the side of the fabricated photonic crystal slab. The image shows only a very small fraction ($< 0.2\ ^0\!/_{00}$) of the entire photonic crystal. On the right side the support to which the membrane is connected is visible and the air gap underneath the slab can be seen.

The optical properties of a photonic crystal slab are described by the dispersion relation, which was discussed in section 2.2 (Fig. 1.4). Since the material properties and the geometrical dimensions are known, we can calculate the effective refractive index of the photonic crystal slab using Eq. 1.2. With $\phi_{air} = 0.36$ and $\phi_{Si_3N_4} = 0.64$, we calculate the effective refractive index of our photonic crystal slab to be $n_{eff} = 1.83$. The effective refractive index of the crystal is a useful characteristic parameter that will be used in the following.

Freestanding photonic crystal slabs have also been fabricated by e-beam lithography (e.g., [38]). The advantage of our structures is the homogeneity of the lattice over a large area. Especially for far-field investigations, as we will perform, where averaging over many unit cells takes place, the homogeneity is an important issue. In addition, e-beam writing of such large areas is time consuming.

1.2.3 Artificial opals made by self-assembly

The three-dimensional photonic crystals, investigated in chapter 5, are fabricated by self-assembly [39]. A colloidal suspension of polystyrene latex spheres in water was used (Duke Scientific). By slow sedimentation the crystals were grown. Afterwards, they were carefully dried by evaporating the water over a time of about 1 - 2 months. The process results in artificial opals of polystyrene spheres.

We investigate opals of five different sphere sizes: $r = 120$ nm, $r = 129$ nm, $r = 180$ nm, $r = 213$ nm and $r = 241$ nm. The monodispersity of the spheres is better

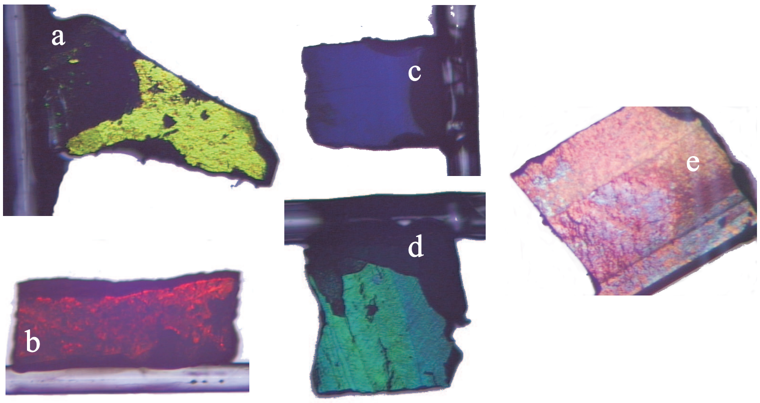

Figure 1.11: Polystyrene opals of different sphere radii imaged with an optical reflection microscope: a) r = 120 nm, b) r = 129 nm, c) r = 180 nm, d) r = 213 nm, and e) r = 241 nm. As can be seen in a) to d), the crystals are glued to an optical fibre for ease of handling in the near-field experiments. The images show different wavelength ranges reflected, when the Bragg condition is fulfilled. These wavelength ranges correspond to the forbidden frequencies in the Γ - L stopgaps.

than 2%. The volume fraction of the crystals is $\phi_{polystyrene} = 0.74$ [39]. The refractive index of polystyrene is n = 1.59. Using Eq. 1.2 leads to an effective refractive index $n_{eff} = 1.46 \pm 0.07$.

Fig. 1.11 shows optical reflection microscope images of the different crystals. The images clearly show strong reflections of distinct wavelength ranges. The large coloured areas indicate the long-range homogeneity of the crystals. The reflected wavelength ranges observed correspond to frequencies in the first and second order stopgaps along the Γ - L crystalline direction (see Fig. 1.5). The band diagram calculations predict a first order Γ - L stopgap centred at $\omega = 0.60$. In Table 1.1 we show the calculated centre wavelength of the stopgap for the crystals of different sphere size. The crystal of sphere radius r = 120 nm has its first order stopgap at 566 nm, which corresponds to the yellow colour observed in Fig. 1.11 a. A red colour is observed for the r = 129 nm crystals, which corresponds to the first order gap at 608 nm (Fig. 1.11 b). For the larger sphere sizes, the first order Γ - L stopgap moves out of the visible wavelength range to the near-infrared. A second order stopgap range approaches the visible window. For the r = 180 nm crystal in Fig. 1.11 c, we observe the dark blue colour. This second order stopgap region moves up in wavelength for increasing sphere size, similar as the first order stopgap. We observe reflection of green light (Fig. 1.11 d) and red (Fig. 1.11 e),

r	$\lambda_{\Gamma-\mathrm{L}}$
120 nm	566 nm
129 nm	608 nm
180 nm	849 nm
213 nm	1004 nm
241 nm	1136 nm

Table 1.1: Calculated stopgaps for polystyrene opals for different sphere sizes. For the calculation we used the determined stopgap frequency $\omega = 0.6$ from the band diagram.

for r = 213 nm and r = 241 nm, respectively.

As can be seen in Fig. 1.11 a to 1.11 d, the crystals are glued to an optical fibre to enable careful handling. The glue used is rapidly drying such that it can not soak the crystal by capillary forces, which would affect the optical characteristic of the crystals. The actual size of the crystals is in the millimeter range.

Chapter 2

Probing of light propagation

Optical characterisation of complex materials is possible by different methods. Mostly, far-field reflectivity or transmission measurements, which can be compared directly with simulations, are performed. In photonic crystal structures, the local probing of light properties becomes essential. The relevant length scale of the crystals is below the wavelength of light, thus sub-wavelength detection is required to obtain full insight in the physical properties of photonic crystals. In this chapter investigation methods (near-field and far-field techniques) used in this thesis are introduced. The far-field reflectivity measurements provide important information about the stopgaps of crystals. Reflectivity spectra obtained as a function of incident angle provide details about the coupling of light to crystal modes. The near-field techniques enable the study of local optical properties of light inside the crystal structure, with sub-wavelength resolution.

2.1 Near-field scanning microscopy

To investigate local properties of light, e.g., interference effects or scattering phenomena, a resolution beyond the wavelength of light is required. As a result, optical microscopy can only be used, when the diffraction limit is overcome. Using evanescent fields of light, the diffraction limit can be overcome. In near-field optical techniques, the basic idea is to access the evanescent fields (near-fields) of a structure or to couple evanescent fields from a light source to a structure under investigation. To access the evanescent fields, sub-wavelength probes that act as an effective dipole are used. One specific possibility is to use a sub-wavelength aperture probes as light source or as detector. The aperture to sample distance has to remain smaller than the aperture diameter. In the specific case of using aperture probes, the resolution of the measurements is completely determined by the size of the aperture. In a near-field scanning optical microscope (NSOM), a sharply tapered dielectric fibre probe can be used as aperture. An alternative to aperture probe are metallic probes, where the apex of the probe has to be sub-wavelength. With both approaches, optical details with a resolution beyond the diffraction limit is achieved.

Different operation methods of a NSOM enable the detection of optical properties in illumination mode or collection mode. In illumination mode, the near-field fibre probe acts as a light source to excite molecules or illuminate a sample. Detection takes place at the other side of the sample [40], [41]. A NSOM operating in collection mode can be used to investigate local optical fields inside a sample [42]. In literature different names for NSOM can be found (e.g., SNOM, STOM, TNOM, PSTM etc.).

With its small excitation volume ($10^5\,\mathrm{nm}^3$) NSOM has advantages over confocal detection ($\sim 10^8\,\mathrm{nm}^3$) resulting in higher resolution and a better signal to noise ratio. Moreover, the topography is acquired simultaneously. NSOM was the first method to show single molecule detection at room temperature [43]. Moreover, Raman spectroscopy, ultrafast microspectroscopy and multi-photon processes are becoming relevant topics (e.g., [44]).

In this chapter, we focus on two special measurement setups and elucidate the technical details such, that the measurements presented in the following chapters are more easily understood.

2.1.1 Fabrication of near-field optical aperture probes

The heart of the near-field scanning microscopes described in this thesis, is the near-field aperture probe. It is fabricated from single-mode optical fibre (cut-off frequency depending on the experiment), by local heating and subsequent pulling to achieve a sharp taper region with a small end face ($\sim 80\,\text{nm}$). The pulling is performed with a CO_2-laser based micropipette/fibre puller P-2000 (Sutter Instrument Company). Pulling parameters, such as pulling strength, start velocity, delay time and laser power, have to be adjusted to obtain an optimal taper of the fibre. The pulled near-field fibre probes (tips) are sometimes directly used for collection mode measurements on relatively flat structures (section 3.2.2). However, in strongly modulated structures, e.g., with large refractive index variations on a scale comparable to the wavelength like photonic crystals, scattering of light occurs. This light emanating from the structure can couple directly into the bare fibre probe. Therefore, separating intensity distributions associated with propagating light inside the structure is very hard from measurements obtained with uncoated fibre probes. Moreover, for the near-field microscope operating in illumination mode, a well defined aperture is required. For these reasons, our probes are metal coated in a high vacuum evaporator (BAK 600). First a thin chromium layer of $\sim 1\,\text{nm}$ and afterwards an aluminium layer of $\sim 100\,\text{nm}$ thickness are deposited on the pulled fibres. The chromium layer is used to obtain better adhesion of the aluminium. Other coating methods use for example a multilayer process of alternating thin titanium and thick aluminium layers [45]. In the collection mode near-field setup we have found that the metal coating strongly reduces the pick up of scattered light and also prevents the detection of light that travels along and just above the sample surface. Sofar, we have found no evidence for an influence on the optical properties of the investigated structure caused by the probe with its metal coating. Theoretical calculations predict a small effect [46]. To produce a well defined circular aperture in the coating at the end facet of the tip, the coat-

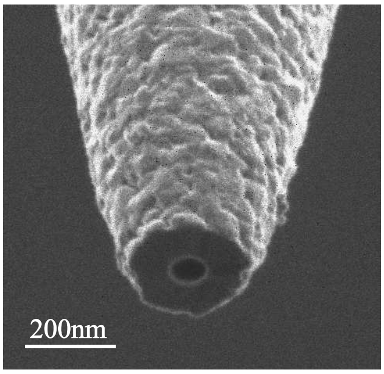

Figure 2.1: Typical near-field probe after side-on milling by a focussed ion beam. A circular aperture of a diameter $\sim 80\,\text{nm}$ and the grainy structure of the $100\,\text{nm}$ thick aluminum coating are clearly visible.

ing process is performed under an angle (shadow effect). The resulting apertures can be cleaned up or enlarged to every desired dimension through side-on milling with a focused ion beam (FIB, 200 FEI) [47]. Since the NSOM techniques became established and commercially available, novel probe designs are receiving a great deal of attention (e.g., [48], [49]).

Figure 2.1 shows the end face of a typical near-field probe fabricated by the process described above. A circular aperture of ∼80 nm is clearly visible. The image was acquired by the FIB by scanning the ion-beam with an ion current of 4 pA and collecting secondary electrons coming from the tip. Even the grainy structure of the aluminum coating is resolved.

The fabrication process of our fibre probes is highly reproducible and produces probes that have a throughput of typically 10^{-5}. In all measurements presented in this thesis (expect for the shape evolution in space of a phase singularity) coated fibre probes with aperture diameters between 80 nm and 110 nm were used. The aperture size determines the optical resolution of the measurements. The lateral topographical resolution is of the order of the diameter of the probe end face, but usually much better. In that case a small Al grain located at the end face of the tip results in an enhanced resolution.

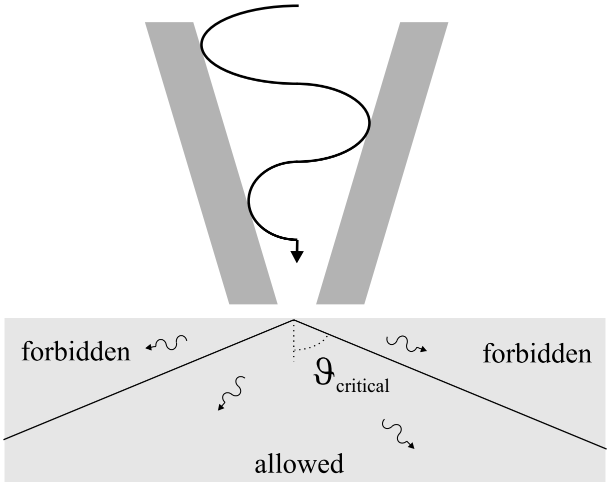

Figure 2.2: Illustration of coupling process of light coming from a near-field probe to a sample. Propagating waves can couple to the angular range of allowed angles. Only near-field (evanescent) waves can couple to forbidden angles. The transition between forbidden and allowed is given by the critical angle ϑ for total internal reflection at the material interface.

Figure 2.2 sketches the principle of evanescent coupling from a sub-wavelength aperture to a sample surface. If a near-field aperture probe is brought in close vicinity to a sample, for example an artificial opal or a glass plate, not only propagating light waves coming from the tip can couple to the sample. The propagating light couples to the region of the so-called allowed angles. This is the range of angles between the cone limited by the critical angle ϑ_c, that is defined by the total reflection on the air-sample interface

$$sin(\vartheta_c) = \frac{n_{air}}{n_{sample}} \ , \tag{2.1}$$

where n_{air} and n_{sample} are the refractive indices of air and the sample, respectively. In the case of a near-field probe close to the surface, evanescent field components can couple to the sample. These field components will couple to the so-called forbidden angles.

2.1.2 Photon scanning tunnelling microscopy

A near-field microscope operated in collection mode is called photon scanning tunnelling microscope (PSTM) [50]. A near-field probe picks up part of the evanescent fields above a structure. Detection of the evanescent field at each surface position allows a reconstruction of an optical intensity distribution that is associated with the light propagating inside the structure. Mostly, our PSTM is operated for investigation of light in the visible wavelength range, however, the setup has recently been modified to enable investigations in the telecommunication windows at $\lambda = 1.3\,\mu$m and $\lambda = 1.5\,\mu$m.

Figure 2.3 shows the layout of our PSTM and the heterodyne interferometric detection scheme. The principle is illustrated with a channel waveguide with an inserted hole array as the photonic structure of interest. The optical fibre probe (tip) is raster scanned over the surface of the structure under investigation. A constant distance between tip and surface is maintained with a tuning fork based shear-force height feedback mechanism [51]. Recording the applied piezo-voltage of the height feedback yields the topography of the structure. The topographical details are visualised with an accuracy of ~ 50 nm in plane and ~ 1 nm in the vertical direction. At a typical tip to surface separation of $z \sim 10$ nm, the evanescent tail of optical fields in the structure is frustrated in the taper region of the fibre probe. Hereby, a propagating mode inside the fibre is excited, which is subsequently detected with a photo multiplier tube (PMT). From the detected intensity as a function of tip position on the sample, a map of the optical intensity inside the structure is constructed. Optical and topographical information obtained in this way contain details on the nanometre scale and reveal local sample properties.

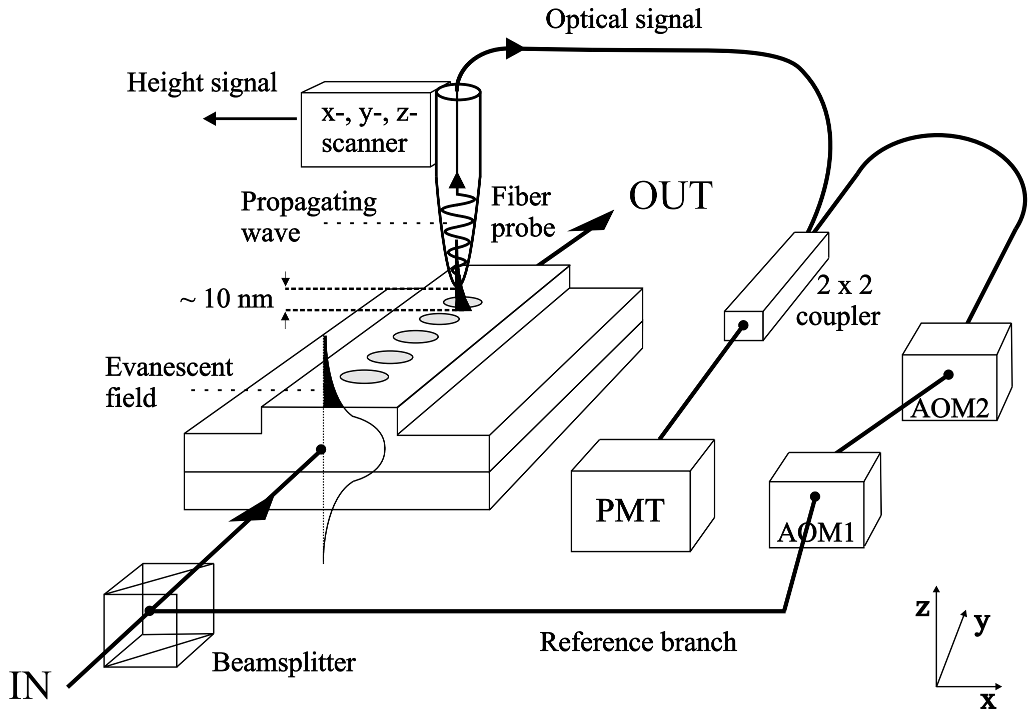

Figure 2.3: Layout of the interferometric PSTM, which consists of a conventional PSTM incorporated into one branch of a Mach-Zehnder interferometer. Two acousto-optic modulators (AOM) in the reference branch enable heterodyne detection. A standard photonmultiplier tube (PMT) is used as detector. The fibre probe is scanned across the photonic sample with piezo actuators. In this way, the heterodyne interferometric PSTM measures the amplitude and the phase of the propagating light simultaneously with the topography of the structure. This setup enables a full optical investigation of light waves inside photonic structures.

On this scale such information can not be gained by far-field techniques, which are, by their nature, limited by diffraction. Only by strong local scattering or induced luminescence can far-field methods show local fields with diffraction limited resolution.

Already in 1993, a heterodyne detection in a near-field scanning optical microscope was introduced to investigate phase effects on a test structure [52]. Adopting a similar concept, we incorporated the conventional PSTM into one branch of a Mach-Zehnder interferometer (see Fig. 2.3) to detect the phase of light propagating inside a structure [53]. To enable heterodyne detection, the optical frequency of light in the reference branch is shifted by 40 kHz with two acousto-optic modulators (AOM). Light collected by the near-field probe (signal) is interfered with light in the reference branch by using a 2×2 fibre coupler. The resulting intensity is detected by the PMT. The PMT signal and the reference of the 40 kHz are both fed to a Lock-in-Amplifier to produce two signals I_1 and I_2 with

$$I_1 \propto A_s \cdot A_r \cdot cos(\varphi) \quad \text{and} \quad I_2 \propto A_s \cdot A_r \cdot sin(\varphi) \ . \tag{2.2}$$

Here, A_s and A_r are the optical amplitudes of the signal and reference branch, respectively and φ is the optical phase difference of light in the two branches. From the measured signals, we extract the amplitude, the cosine and the sine of the phase:

$$A_s \propto \sqrt{I_1^2 + I_2^2} \ , \tag{2.3}$$

$$cos(\varphi) = \frac{I_1}{\sqrt{I_1^2 + I_2^2}} \quad \text{and} \quad sin(\varphi) = \frac{I_2}{\sqrt{I_1^2 + I_2^2}} \ . \tag{2.4}$$

Thus, amplitude and phase of the optical field in the sample are separated. Figure 2.4 shows an example of a PSTM measurement. In Fig. 2.4 a the waveguide ridge is clearly visible. Figure 2.4 b shows the signal produced by the Lock-in-Amplifier (Eq. 2.2). Horizonal stripes indicate the interference of light. The brighter colour in the waveguide region indicates an increased optical intensity with respect to the left and right side of the waveguide. Figures 2.4 c and 2.4 d show the separated amplitude and phase information of the optical field, respectively.

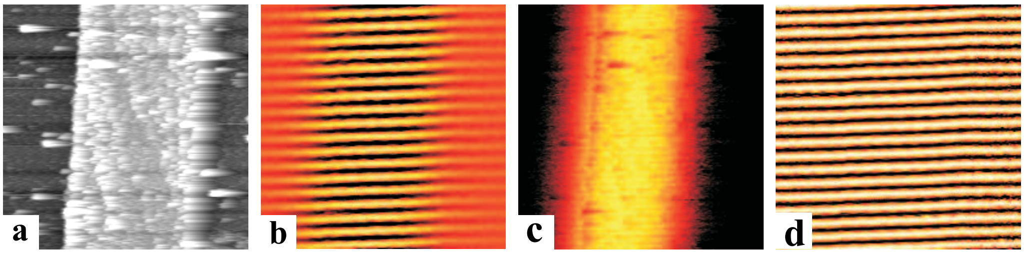

Figure 2.4: Measurement of a straight channel waveguide. a) depicts the topographical image obtained simultaneously with b), the optical information consisting of the multiplication of the amplitudes and the phase difference of the interfering signals. c) and d) show the separated amplitude and phase information as obtained with Eq. 2.3 and Eq. 2.4, respectively. Image sizes: 3.9 μm × 2.3 μm.

During a measurement the length of the reference branch is kept constant, whereas the length of the measurement branch changes as the probe collects light from different positions of the sample. As a result, interference fringes are observed as the tip position is varied (see Fig. 2.4 b). They can be directly interpreted in terms of the phase of the light inside the structure (see Fig. 2.4 d). Consequently, the observed periodicity of either $sin(\varphi)$ or $cos(\varphi)$ corresponds to the wavelength of light inside the structure.

The two branches of the Mach-Zehnder interferometer consist of both bulk optics and fibre optics. A box around the setup strongly reduces thermal drift and air flow that would otherwise disturb the sensitive interferometric measurement. The stability and drift of the phase measurement is checked. To this end, a line scan along the waveguide axis is observed in time before and after each measurement to observe any changes in position of the phase pattern. A phase drift smaller than π in 15 minutes is considered sufficiently small.

2.1.3 Illumination mode near-field scanning optical microscopy

The near-field scanning optical microscope (NSOM) used for our investigations is operated in illumination mode [54], in which light emitted by the probe is detected on the other side of the sample. Figure 2.5 shows a schematic of the experimental setup used to investigate the three-dimensional colloidal photonic crystals. A conventional NSOM setup projects the small excitation volume onto a detector with a high NA objective (e.g., [54], [55]). We have modified this detection path. To investigate the coupling of light coming from a point-like source to a crystal together with transmission properties of a photonic crystal, a photodiode is positioned directly beneath the sample to collect the transmitted light. In this way all the light coming from the bottom crystal facet is collected and averaged over the full extent of the facet. This is beneficial for our investigation, since local variations in the out-coupling efficiency at the bottom of the crystal are averaged and thus the setup only detects in-coupling effects with sub-wavelength resolution. The fibre probe is kept at a constant height of $z \sim 10\,\text{nm}$ from the sample surface using a shear-force feedback mechanism [51], while the sample including detector is scanned in the x-y plane. As the crystal is scanned underneath the tip, the positional dependent coupling and subsequent transmission of light coming from the near-field probe through the sample is measured. The topographical information of the samples under investigation is simultaneously measured with the optical signal. The technique may, under certain conditions, yield information on the local density of states (LDOS) [56] at the interface of a photonic crystal.

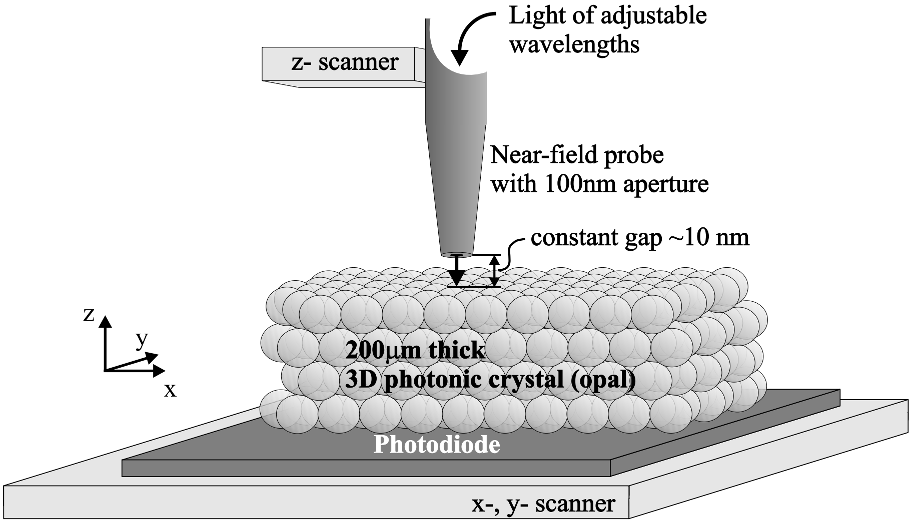

Figure 2.5: Schematic of the illumination mode near-field setup. Light from a point source (near-field aperture probe) is launched to the three-dimensional photonic crystal. By scanning the fibre probe relative to the crystalline surface, the light transfer can be studied as a function of launching position. A photodiode, mounted underneath the crystal, detects all the light reaching the rear of the crystal.

2.1.4 Three-dimensional measurement mode

The operation of PSTM/NSOM in shear force feedback results in an optical response image at a certain contour of constant force interaction, typically at a distance of $z \sim 10\,\text{nm}$. The topographic structure can influence the optical contrast [57]. A truly reliable investigation requires the mapping of the full three-dimensional field distribution above the sample, i.e., including measurement in the z-direction [58]. Figure 2.6 shows schematically the three-dimensional measurement mode, which is implemented in both our setups (PSTM and NSOM). By moving the probe perpendicular towards and away from the sample surface the intensity of the optical signal is measured as a function of probe height in both, the retraction and approach trajectory. We consider the PSTM measurements on a waveguide structure. The gray plane in the left sketch in Fig. 2.6 is the constant gap measurement obtained in a standard force feedback measurement. The approach or retraction curves will yield the exponential decay of the evanescent field of the light inside the waveguide. Performing approach curves at different positions on the sample allows the reconstruction of images at different planes parallel and perpendicular to the sample. In the sketch on the right side in Fig. 2.6, some reconstructed planes are depicted: the (x,y)-plane is oriented parallel to the sample, the (x,z)-plane and the (y,z)-plane perpendicular. The three-dimensional measurement mode provides a test of the reliability of the near-field pattern and is an important part of any near-field setup. Moreover, the measurement reveals to which extent stray and scattered light contribute to the optical signal in the constant shear-force measurement.

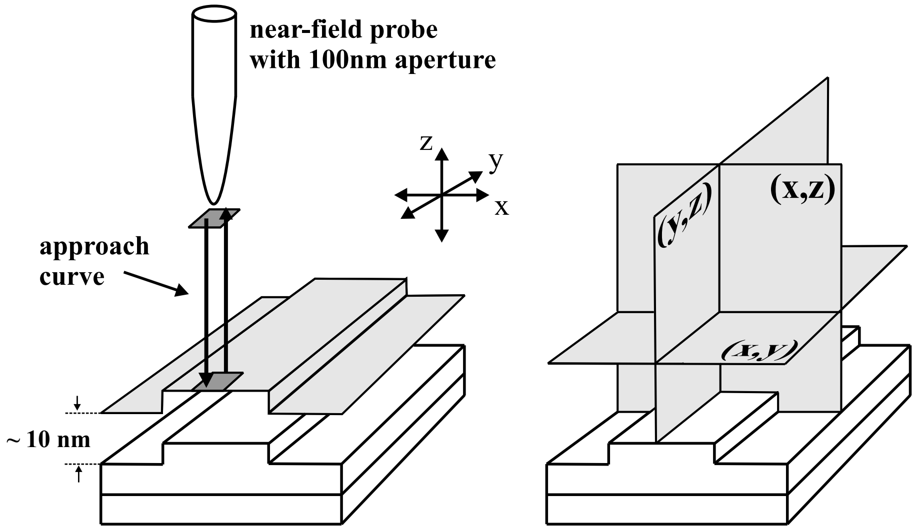

Figure 2.6: Three-dimensional measurement mode. At each position in the (x,y)-plane, a retraction and an approach curve is measured. In this way, measurement images at planes oriented parallel to the sample, (x,y)-plane, and oriented perpendicular to the sample, (x,z)-plane and (y,z)-plane, can be reconstructed. Moreover, one approach curve contains all the information to determine whether or not the near-field measurement contains light scattered directly from a structure or topographical artefact.

2.2 Far-field reflectivity methods

The optical characterisation of photonic crystals is mostly carried out by far-field techniques. Far-field methods provide a good, spatially averaging method to investigate the overall properties of a photonic structure. As such they are complementary to near-field techniques that reveal more local and detailed information. By transmission and reflectivity measurements, stopgaps, e.g., [8], [33] or guided modes [59] can be investigated. Losses through, e.g., y-junction embedded in a photonic crystal have been investigated [59], [60]. It has been shown that two-dimensional photonic crystal slabs enables trapping of photons [7]. Group-velocity dispersion in linear waveguides in a photonic crystal slab have been measured [61] and the propagation of ultrashort nonlinear pulses investigated [62]. Moreover, angle-dependent reflectivity spectra on two-dimensional photonic crystals reveal coupling to resonant modes (modes above the light line) [63] of the structure (e.g., [64], [65] and [66]). Moreover, time-resolved pulse propagation and spontaneous emission of laser dyes located inside the crystal have been investigated [8].

In this thesis we use reflectivity measurements to determine the stopgaps of the two-dimensional photonic crystal slab and of the three-dimensional polystyrene opals. In addition, we investigate the coupling of incident light to resonant modes of the two-dimensional photonic crystal slab. To this end, we perform angle-dependent reflectivity measurements that are briefly elucidated in the following.

2.2.1 Normal incidence

To probe the stopgaps on the two- and three-dimensional photonic crystals, normal incidence reflectivity spectra are performed with two different setups. For the measurements on the polystyrene opals, we use a Biorad Fourier-Transformation spectrometer (FTS6000) [67]. Light from a Tungsten-Halogen-lamp passes a Michelson interferometer, of which the end mirror of one branch is moved continuously for- and backwards with a frequency of 50 kHz. This enables heterodyne detection (see section 2.1.2). The white light is then focussed with an objective of a numerical aperture (NA) of 0.17 on to the sample surface. The same objective is used to pick up the reflected spectrum, which is subsequently detected by a convectional Si-diode. The spectra are obtained with a frequency resolution of 16 cm^{-1}.

A different setup is used to obtain reflectivity spectra on the two-dimensional photonic crystal slab. White light is provided from an ozone-free Xenon-lamp (75 W, shortarc). With an objective of a NA = 0.4 (20 ×), the linearly polarised beam is focused to a spot with a diameter of $\sim 40\,\mu$m at the endface of the membrane. A Nitrogen cooled CCD camera detects the spectra from 500 nm to 1000 nm. The resolution of the spectra is 3 nm and the camera has a very low dark current.

In both setups described, we use the same objective for the detection of the reflected light as for the illumination of the sample. Due to the focussing of the beam, we have a range of wavevectors available in addition to the wavevectors parallel to the crystalline direction of interest. The angular spread of wavevectors is given by

$$sin(\varphi_{air}) = \frac{\mathrm{NA}}{\sqrt{\varepsilon_{air}}} \quad \text{and} \quad sin(\varphi_{crystal}) = \frac{sin(\varphi_{air})}{\sqrt{\varepsilon_{eff}}} \ , \tag{2.5}$$

where φ_{air} is the angular spread of incident and reflected wavevectors in air and $\varphi_{crystal}$ the resulting angular spread of wavevectors in the photonic crystals. The value of $\varphi_{crystal}$ predicts to which extent the different directions in the reflectivity spectra are probed.

We calculate the angular spread of wavevectors for the specific setups used on the two-dimensional photonic crystal slab. The numerical aperture of the used objective is 0.4. As a result, a spread of wavevectors in air is available over $\pm 23.6\,^\circ$. The effective index of the two-dimensional photonic crystal slab was calculated earlier and is 1.83. With this, the wavevector spread in the photonic crystal slab probed by the in-plane reflectivity is determined to be $\varphi_{Si_3N_4} = \pm 12.6\,^\circ$. Similarly, we calculate the spread of wavevectors provided in the reflectivity measurements on the opals. With the NA = 0.17 of the objective used, the spread in air becomes $\varphi_{air} = \pm 9.8^\circ$. For the polystyrene opals the effective refractive index is $n_{eff} = 1.46$. The angular spread is $\varphi_{opal} = \pm 8\,^\circ$. In both reflectivity measurement setups, the wavevector spread is reasonable small. It is expected, that the reflectivity spectra are influenced only slightly, i.e., a broadening of the stopgaps can occur.

2.2.2 Specular reflectivity

In the band diagram of a two-dimensional photonic crystal slab three types of modes are described: bound states or guided modes (below light line), resonant states (above light line) and a continuum of modes in air (gray area). By measuring angle-dependent (also called specular) reflectivity spectra on a photonic crystal slab, the resonant states are probed and part of the dispersion relation can be reconstructed.

Figure 2.7 shows the principle of the specular reflectivity measurement. A parallel beam of white light, with a size of $300\,\mu\text{m} \times 2\,\text{mm}$, is incident on the photonic crystal slab under an angle Θ. Reflection takes place and a spectrum is measured under a reflection angle of $-\Theta$ as shown in Fig. 2.7. If the length of the wavevector projection $k_{//}$ and the optical frequency ω of the incident light match those of a resonant state of the photonic crystal slab, coupling occurs and a resonance feature is observed in the reflection spectrum. Extracting the frequency of the resonance from the spectrum provides the information needed to reconstruct the dispersion relation of the resonant modes, as the optical dispersion relation of air combined with simple trigonometry suffices

$$k_{\|} = k \cdot sin\Theta = \omega_{res} \cdot sin\Theta = \frac{a}{\lambda_{0,res}} \cdot sin\Theta \ , \tag{2.6}$$

where k is the dimensionless wavevector of incident light at resonance, ω_{res} is the dimensionless frequency at resonance, $\lambda_{0,res}$ is the vacuum wavelength of light at resonance, Θ is the angle of incidence, c is the speed of light in vacuum and a is the periodicity of the lattice.

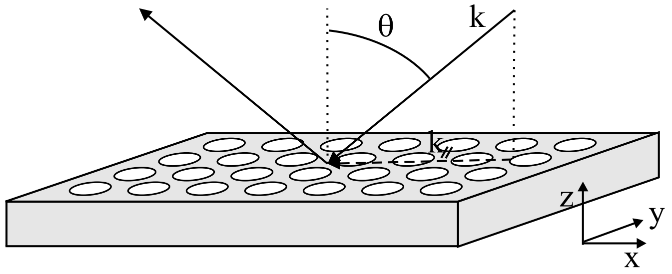

Figure 2.7: Top reflection setup used to measure angle-dependent spectra. A parallel beam of white light is incident on the photonic crystal slab under an angle Θ. The detector is positioned under an angle $-\Theta$, to measure the spectra of the reflected light.

Far-field reflectivity measurements enable probing light properties of guided and non-guided modes of photonic crystal slabs. This combination provides a good insight to the optical properties of the photonic crystal slabs.

Chapter 3

Light scattering of sub-wavelength dielectric structures

Photon scanning tunnelling microscopy enables the visualisation of the optical field distribution of propagating light in a structure (e.g., a channel waveguide) with sub-wavelength resolution. First, we map the fields around nanometer size scatterers, such as a single slit, a periodic array of 15 slits and a periodic array of 15 air rods that are milled into a channel waveguide. The obtained information reveals material properties of the three-dimensional waveguide layer composite. Moreover, scattering phenomena in front of the structures are scrutinised and provide information that is not possible to observe with far-field methods, like the excitation of leaky modes.

In the second part, we present observation of the phase of light around the 15 air rod structure. There, interference between incoming light and circularly scattered waves gives rise to phase jumps and phase singularities. Using the three-dimensional measurement mode, we study the shape evolution of such phase singularities as a function of tip to sample separation. Furthermore, to show the importance of the three-dimensional measurement mode, we investigate a waveguide containing two slits, where scattered and guided light are directly discriminated on their propagation and non-propagation character.

3.1 Local optical intensity distributions

Investigations by photon scanning tunnelling microscopy (PSTM) provide optical details about the flow of light. The optical fields in waveguides [68], junctions [69] and microcavities [70] structures have been investigated visualised. Not only the optical field distribution of light inside a structure is measured, but simultaneously the topography of the structure itself is mapped. This allows direct determination of the geometrical influence of the light flow. We use a phase-sensitive PSTM that also allows detection of the phase evolution of light inside the structure [53], [71]. With this method, a complete characterisation of the locally propagating optical fields is possible.

Studies of the local optical field distributions in photonic crystal structures are attracting a lot of interest as they will contribute to a better the understanding of the optical properties and to the optimisation of the crystals for applications. So far, local investigations in the near-field regime have only been performed on one- and two-dimensional structures (e.g., [72], [73], [74]). Investing a one-dimensional periodic array of Au nanoparticles revealed an unexpected squeezing of the optical near-field due to plasmon coupling [75]. By a scanning probe optical microscope combined with laser spectroscopy the transmitted light through a waveguide-microresonator-waveguide structure embedded in a macroporous silicon two-dimensional crystal has been investigated [76]. Most exciting, the near-field technique could allow imaging of local density of states [77], [56]. Moreover, the technique was used for near-field optical lithography for fabrication of photonic crystals [78].

In this chapter, the optical properties of light propagating in three different waveguide structures is investigated using PSTM. First, a single slit milled into the waveguide ridge is examined. In the second part, we visualise the light propagation in and around periodic arrays consisting of 15 air rods and 15 slits in a channel waveguide. The fabrication details of the structures have been described in section 1.2.1. The geometrical dimensions of the channel waveguide were chosen such that for the interesting wavelength range between $\lambda_0 = 585\,\mathrm{nm}$ and $\lambda_0 = 647\,\mathrm{nm}$ only the propagation of the fundamental transverse electric mode (TE_{00}, electric field in x-y plane) and no transverse magnetic mode (magnetic field in the x-y plane) is supported. The experiments were performed with different laser sources: a HeNe laser, an Ar / Kr laser and a tuneable frequency-doubled (Ti: Sapphire-pumped) optical parametric oscillator. Light is coupled into the photonic structures with a microscope objective (0.4 NA, 20 ×).

3.1.1 A sub-wavelength single slit in a channel waveguide

Using a photon scanning tunnelling microscope (PSTM) we map the intensity of light around a single slit in a waveguide. Figure 3.1 shows the PSTM measurements. In the topographical image (Fig. 3.1 a) the waveguide ridge and the slit are clearly visible. The measurements show a height resolution of 0.5 nm and a lateral topographical resolution better than 50 nm. Figure 3.1 b depicts the optical intensity obtained simultaneously with the topography. Light of $\lambda_0 = 632.8$ nm is coupled into the channel waveguide (~ 4 mm away from the image area) and propagates from the top of the image to the bottom. In front of the slit, which is in the upper part of Fig. 3.1 b, horizontal intensity stripes are clearly resolved. A periodicity of roughly 216 nm is observed over a large range in front of the structure. Just in front of the slit itself, an increased intensity is observed. We attribute this increase in intensity to light that scatters directly from the slit into the aperture of the coated fibre probe. Measurements with uncoated fibre probes contained

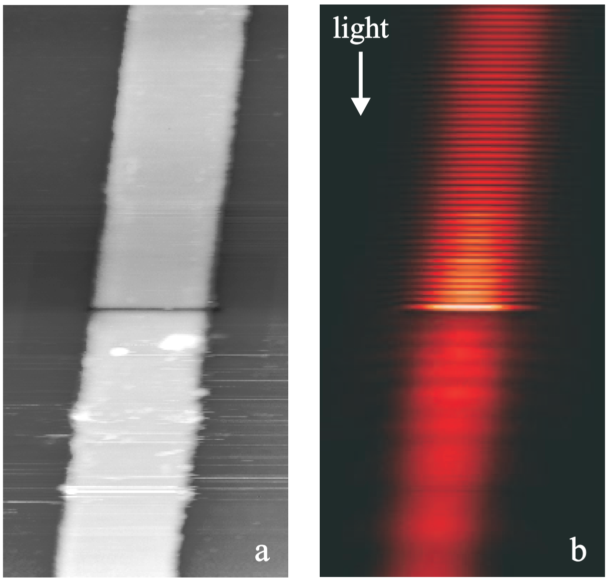

Figure 3.1: Simultaneously measured topographical a) and optical b) information of a waveguide containing a single slit obtained with a PSTM. Clearly, the 160 nm wide slit in the waveguide ridge is resolved in the high resolution topographical image. The optical field distribution shows a periodic pattern resulting from interference between incoming light (arrow indicates direction) and reflected light at the slit. Image size: 4.0 μm × 20.0 μm.

so much of this stray light, that investigations in a region of 680 nm around the slit were impossible. Furthermore, Fig. 3.1b shows that some light is transmitted through the slit and reappears as a guided mode of the waveguide behind the slit.

To analyse the periodic pattern in front of the slit with a good signal to noise ratio, several adjacent parallel line traces along the centre axis of the waveguide have been summed up. Figure 3.2 a depicts the average intensity obtained by summing up 80 line traces from Fig. 3.1 b. The high peak corresponding to the increased intensity in front of the slit is evident in Fig. 3.2 a. Moreover, the long range periodic pattern in front of the slit is obvious. A Fourier transformation over 10.5 μm (dotted box in Fig. 3.2 a) is shown in Fig. 3.2 b. A strong peak corresponding to a periodicity of 216 ± 2 nm is observed. Obviously, this sub-wavelength periodicity indicates that the pattern is caused by interference: reflected and incoming light built up a standing wave in front of the slit. As a result, we observe that the wavelength of the guided mode is $\lambda_{TE_{00}} = 432$ nm. Using the effective index method [79], we calculated that the refractive index of the fundamental TE_{00} mode is $n_{eff} = 1.4604$, which leads to a wavelength of the mode in the material of $\lambda_{TE_{00}} = \lambda_0 / n_{eff} = 433.3$ nm. The agreement with the value obtained from the measurement is perfect. At lower spatial frequencies additional peaks are visible indicated by arrows in Fig. 3.2b. The decaying average intensity of light before

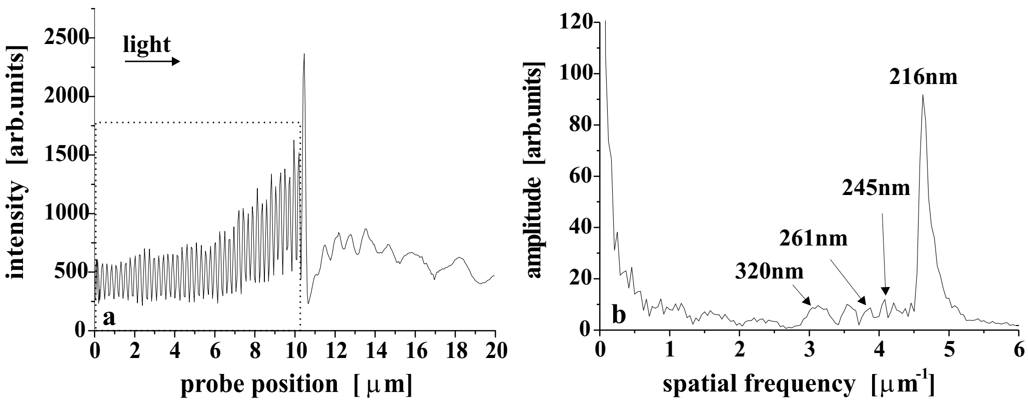

Figure 3.2: a) Intensity graph constructed by summing up 80 line traces of the optical image along the waveguide. The maximum of the high intense peak occurs at the material-air interface of the single slit. b) Fourier transformation of boxed area of a). The clear peak corresponding to a periodicity of 216 nm indicates that the interference pattern is dominated by a standing wave set up by an incoming and a reflected TE_{00} mode. The peaks at lower spatial frequencies (indicated by the arrows) are the result of interference between the TE_{00} mode and leaky modes.

the slit (Fig. 3.2 a) already hints at the origin of those peaks. The decay can be fitted with an exponential function $e^{-\beta x}$, where $\beta = 0.38\,\mu\text{m}^{-1}$ is found as decay rate. Furthermore, we analyse the modulation depth M of the interference pattern, which is given by

$$M = \frac{I_{max} - I_{min}}{I_{max} + I_{min}} \quad . \tag{3.1}$$

In a range of $3\,\mu$m before the slit, the modulation depth is 0.48, which corresponds to an amplitude reflection coefficient of 26 %. Further away from the slit, the modulation depth has decreased to 0.40, suggesting a leakage of light out of the waveguide. The decrease of the modulation depth far away from the slit, the exponential decay of the average intensity and the peaks at lower spatial frequencies in the Fourier transformation are attributed to the presence of so-called leaky modes propagating in the opposite direction of the incoming light. These leaky modes have a strong coupling to continuum modes in air and therefore have a high loss rate. Theoretically, leaky modes are predicted for n_{eff} ranging from 1.4460 to 0.5508. To verify the existence of the leaky modes, we have calculated the interference length between them and the incoming fundamental TE_{00} mode of our waveguide. The resulting numbers of spatial frequencies are in agreement with the measured ones. Apparently, the scattering of light, most probably due to roughness of the slit walls, excites leaky modes.

The observation of light scattering into leaky modes exemplifies the power of PSTM to identify local properties of optical fields. Since leaky modes are present only within a few μm in front of the slit, there is no possibility to defect them with conventional input / output methods.

3.1.2 Periodic arrays of 15 air rods and 15 slits

After the investigation of light scattering at a single slit we now investigate arrays of scatterers. We focus on two different structures that consist of a ridge waveguide containing a periodic array of silts and one containing a periodic array of air rods.

Optical intensity measurements

The topography of two different structures as obtained by PSTM measurements is shown in Figs. 3.3 a and 3.3 c. The simultaneously obtained optical intensity maps are presented in Figs. 3.3 b and 3.3 d. In both measurements, light is coupled into the waveguide (incoupling position is at a large distance of ~ 4 mm from measurement area) and propagates from top to bottom in the images. For the measurement on the air rod structure (Fig. 3.3 b) light with a wavelength of $\lambda_0 = 647$ nm was

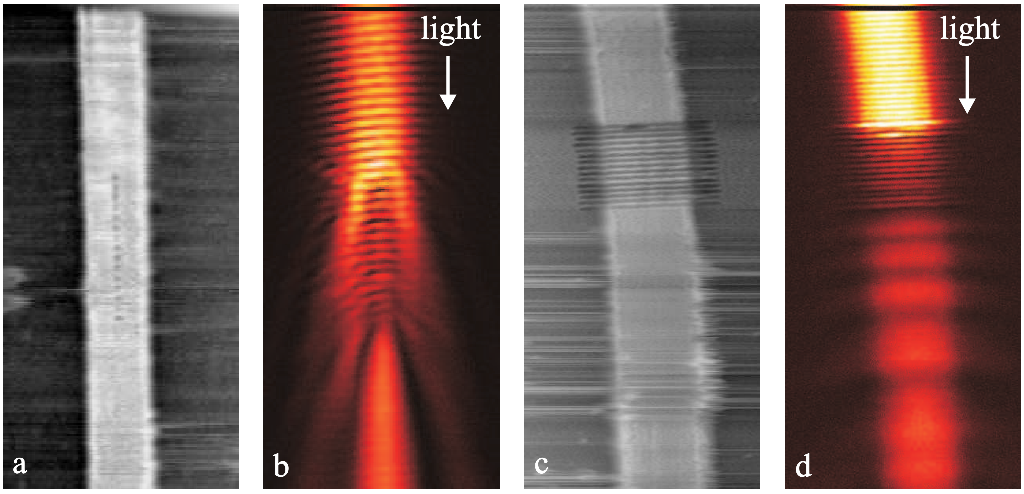

Figure 3.3: Measurement of two different structures obtained by PSTM. a) and b) show the topography and the optical field distribution for $\lambda_0 = 647\,\mathrm{nm}$, respectively of a channel waveguide containing 15 air rods. In the topographical image c) the waveguide containing 15 slits is clearly resolved. The simultaneously obtained optical image for $\lambda_0 = 610\,\mathrm{nm}$ is shown in d). The periodicity of both arrays is 220 nm, the air rods have a diameter of 110 nm. The width and length of the slits is 110 nm and 2.5 μm, respectively. In both optical images, light propagates from top to bottom (arrow). In front of the periodic arrays a standing wave is built by interference between incoming and light reflected by the rods and slits. Behind both structures, some light recovers in the waveguide to a propagating mode. The image sizes of a) and b) 5.8 μm × 11.1 μm (horizontal × vertical) and of c) and d) 4.0 μm × 18.3 μm (horizontal × vertical).

coupled into the waveguide. For the measurement on the slit array (Fig. 3.3 d), light of $\lambda_0 = 610\,\mathrm{nm}$ was used.

In Figs. 3.3 a and 3.3 c, the 11 nm high waveguide ridges are apparent and the periodic structures are easily resolved. From the topographical measurement, we determine the dimensions of the waveguide and the array (we generally find that the calibration of our PSTM agrees with the one of the FIB). The measured sizes of the sub-wavelength features are given in table 3.1. The measured dimensions differ slightly from the design values. We attribute the broadening of the features to the fabrication process with the FIB. Especially, charging of the Si_3N_4 results in enlargement of the feature sizes, even though a conducting carbon layer is used. The waveguide width is probably broadened also by tip convolution effects.

In both topographical images, horizontal stripes are visible. In the lower part of Fig. 3.3 c some of those stripes are pronounced. These are fluctuations in the interaction between tip and sample probably caused by changes in the environment, which make the feedback mechanism less stable. Note that these fluctuations in height (7 nm at most) have no significant influence on the simultaneously recorded optical signal (Fig. 3.3 d).

	Fig. 3.3 a (rods)	Fig. 3.3 c (slits)	Design values
waveguide width :	1558 ± 33 nm	1627 ± 13 nm	1500 nm
air rod diameter :	111 ± 37 nm		80 nm
slit width :		122 ± 30 nm	80 nm
slit length :		2333 ± 13 nm	2500 nm

Table 3.1: Values of waveguide and structure dimensions obtained from the measurements shown in Fig. 3.3. For comparison the design values used for the fabrication are shown in the last column. The measured values show reasonable agreement within the error range of tip convolution effects. A slight broadening of the sub-wavelength features is observed compared to the design values.

Figures 3.3 b and 3.3 d depict the measured optical intensity distribution of light inside the structure. In both images the standing waves in front of the the periodic array of air rods and slits, which was already observed in front of the single slit, are clearly visible. Fourier transformation analysis reveals in front of the air rod structure a periodicity of 221 nm and in front of the slit array a periodicity of 213 nm. Again, the periodicity corresponds perfectly to half of the wavelength of the mode in the waveguide ($\lambda_{TE_{00}}/2$). Table 3.2 presents an overview of the modal wavelengths obtained from the measured standing waves and those calculated by $\lambda_{TE_{00}} = \lambda_0/\mathrm{n}_{eff}$. The effective refractive index n_{eff} of the waveguide is calculated by the effective index method [79] and λ_0 is the vacuum wavelength of light. As can be seen in table 3.2 good agreement between the measured and calculated values is found.

The interference patterns just in front of the array structures differ in shape, as can be seen in Figs. 3.3 b and 3.3 d. In the case of the slits the horizontal stripes are straight, whereas in front of the air rod structure a slight curvature of these stripes is observed. In front of a single air rod in a waveguide, we observe similar curvature of the standing wave. A simple picture explains the origin of the curvature. In the case of the air rod structure, the pattern is built up from interference between circularly scattered waves and incoming plane waves. Such interference leads to a parabolic curvature in the first few intensity stripes [50]. In the waveguide with the slit array, light is reflected into a plane wave, resulting in straight interference stripes.

Inside both the air rod array and the slit array a periodic pattern is still visible,

vacuum wavelength	experimental		calculated
λ_0	$\lambda_{TE_{00}}$ air rods	$\lambda_{TE_{00}}$ slits	$\lambda_{\mathrm{TE}_{00}}$
585 nm	398 ± 5 nm	406 ± 4 nm	399 nm
600 nm	405 ± 3 nm	407 ± 6 nm	410 nm
610 nm	416 ± 4 nm	426 ± 7 nm	417 nm
633 nm	428 ± 7 nm	439 ± 8 nm	433 nm
647 nm	441 ± 2 nm	446 ± 3 nm	443 nm

Table 3.2: The wavelength of light propagating in the waveguide as determined from the periodicity of the standing waves. The first column gives the vacuum wavelength λ_0 of light. Second column: calculated wavelength ($\frac{\lambda_0}{n_{eff}}$) of the TE$_{00}$ waveguide modes. To obtain these values, the effective index method [79] was used to calculate the effective refractive index n$_{eff}$ of the structure. The measured values $\lambda_{TE_{00}}$ are given in the third column for the air rod structure and in the fourth column for the slit array.

but the absolute optical intensity decreases inside both structures. In Fig. 3.3 b it can be seen that light passes on the left and right side along the air rod array. Beyond the final air rod, the fundamental mode of the unperturbed waveguide recovers. The mode almost completely recovers after several hundred nanometers beyond the final air rod. A different recovery process is observed after the 15 slit structure in Fig. 3.3 d. Intensity minima and maxima occur in a non-periodic way. Interestingly, with increasing distance beyond the slit array, the distance between the minima increases.

To analyse data in more detail, line traces taken parallel to the waveguide axis are investigated. Figure 3.4 a shows the average intensity produced by summing up adjacent line traces over a ~ 120 nm wide area in the centre of the waveguide of the measurement in Fig. 3.3 b. In a similar way, Fig. 3.4 b has been constructed by summing up adjacent line traces over a 1 μm wide area from Fig. 3.3 d. In both figures, the propagation direction of the light is from the left to the right. The locations of the periodic arrays are indicated by the dotted rectangles.

In front of the periodic arrays in the left part of Figs. 3.4 a and 3.4 b the periodic oscillations of the standing wave are visible. As discussed above and shown in table 3.2, the pattern has a periodicity of half the wavelength of light in the waveguide. A difference in the intensity profile of the standing wave in front of the air rods and slits is clear. In front of the 15 air rods a continuous attenuation of both intensity and the modulation depth M (see Eq. 3.1) is observed over a range of 1 μm. We find a modulation depth of 0.56 close to the air rod structure. Further away from the 15 air rods as well as in front of the 15 slits the intensity and modulation depth of the standing waves are constant. These observations

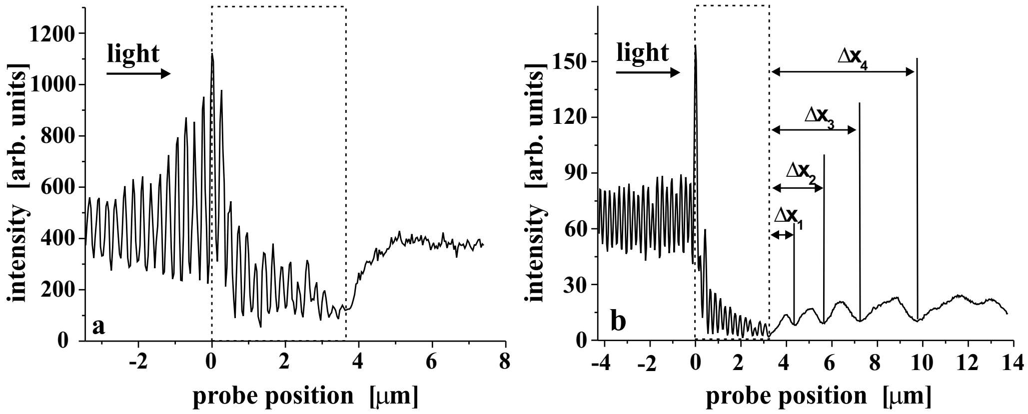

Figure 3.4: Line traces obtained from the measurements in Fig. 3.3. To obtain a better signal-to-noise ratio, several adjacent line traces were summed up to produce the graphs. Light propagates from left to right. The dotted square gives the location of the 15 air rods a) and 15 slits b), respectively. The graphs show clearly the standing waves in front of the periodic structures. In graph b) a recovery with maxima and minima involved is observed. We will analyse the distances $\Delta\,x_i$ between the minima occurring and the position of the last slit.

on the two structures hold qualitatively for all wavelength of light investigated. The decrease in intensity and modulation depth indicates a loss of coherence of the standing waves. We attribute the loss of coherence to a combination of the excitation of leaky mode (see section 3.1.1) and the circularly scattered waves. In the case of 15 slits, no change in the modulation depth of the standing wave is observed. The amount of scattering light into leaky modes is not measurable.

In front of both periodic structures a high intense peak is present, which was also seen in front of the single slit. The peak intensity compared to the amount of incoming light can be up to 2.5 × in the case of the 15 slits and 1.6 × for the air rod structure. We attribute this high intensity of the first peak to light that is directly scattered out of the slit into the aperture probes due to the impedance mismatch between the ridge waveguide and the periodic structure.

In the region of the photonic structures (dotted rectangles), a periodic intensity pattern is found as well. 15 peaks located inside the dotted rectangles are found in both cases (Figs. 3.4 a and 3.4 b). The periodic distance between those peaks corresponds to the periodicity of the array (220 nm) as determined with a Fourier analysis. We observe for all wavelength used that the intensity pattern inside the array have the periodicity of the array structure. Topographical artifacts in the optical image can be excluded for two reasons. Firstly, the exponential decay observed for the maxima of intensity inside the array does not reproduce for the minima of intensity in the array. In the case of artifacts, one would expect to observe for both, maxima and minima, the same decay. Secondly, the intensity stripes found in the periodic region of the air rods are elongated in the horizontal direction. An artifact induced by topography would result in a symmetric pattern with a dimension roughly corresponding to the probe size convoluted with the air rod diameter. Our apertures are circular symmetric, so an elongation in one direction only is not possible. We therefore suggest that direct probing of so-called Bloch modes takes place. Such an observation is only possible with sub-wavelength detection methods.

Behind the periodic structures, light recovers differently for both structures. Some hundreds of nanometers behind the last air rod (Fig. 3.4 a), the fundamental mode (TE_{00}) of the waveguide is recovered. The recovery of light behind the slits is different compared to the air rods (as discussed above). In Fig. 3.4 b a non-periodic intensity pattern is visible.

Intensity distribution simulations

The electric field around the periodic structures has been calculated as a function of wavelength to allow direct comparison to the PSTM data. The two-dimensional simulations are based on Maxwells equations in the frequency domain [80], [81].

In our PSTM measurements, TE polarised light was coupled into the structure. As a result, we compare the measurement to only one component of the simulated E-field. The simulation is performed for a cross-section through a waveguide containing 15 slits. Figure 3.5 shows the $\mid E_{\perp} \mid^2$ distribution of the simulation, since $E_{\perp}$ is perpendicular to the simulation plane and thus the E-field component most comparable to our PSTM measurement. The image is presented in a logarithmic gray scale, where bright means high intensity and dark represents low intensity. Light ($\lambda_0 = 632.8\,\mathrm{nm}$) is launched from the left side and propagates to the right side. The guiding Si_3N_4 ($n = 2.01$) waveguide layer is 55 nm thick and located on top of a $3.2\,\mu$m thick layer SiO_2 ($n = 1.45$) supported by Si. The SiO_2-Si interface has an appreciable reflection coefficient for many wavelengths of light. For this reason, a perfect mirror is chosen to mimic the physical buffer-substrate interface in the simulations, which is realised by placing the artificial computational window boundary at this position. The horizontal axis gives the relative position with respect to the first slit. In front of the slit array, the standing wave pattern is clearly present. At the position of the first slit, light is scattered mainly back into the waveguide and into the SiO_2 substrate. The light scattered into the substrate is subsequently reflected at the Si-substrate located at -$3.2\,\mu$m. This scattered light interferes behind the structure with guided light transmitted through the slits.

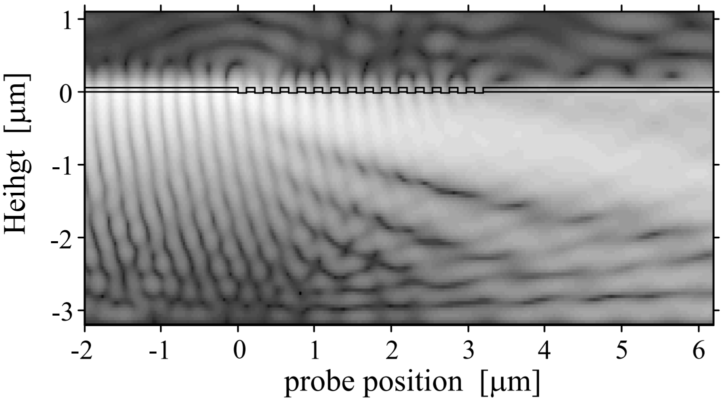

Figure 3.5: Gray scale representation of the $\mid E_\perp \mid^2$ distribution of a two-dimensional simulation of a cross-section through a waveguide ridge containing 15 slits. $\mid E_\perp \mid$ is the E-field component perpendicular to the simulation plane. The geometry of the structure is depicted with drawn lines. The incoming light propagates from left to right. The gray scale scale on the right side gives the intensities in arbitrary units. The colour representation is in logarithmic scale. On the left side, a standing wave in front of the slit array is visible. Furthermore, light scatters from the first slit into the substrate. An interference pattern is produced between propagating light in the guiding layer and reflected light from the Si-substrate located at 3.2 μm.

To compare the simulations directly with the measurements, we plot in Fig. 3.6 $\mid E_\perp \mid^2$ of a line located 10 nm above the waveguide. Again, the standing wave in front of the slit array (indicated by the dotted rectangle) is clear. At the location of the first slit, the highest intensity of the distribution is found. Inside the array a decay in intensity is observed. Behind the 15 slits, a non-periodic recovery of light in the waveguide is found. Two pronounced minima are found for this simulation (marked by x_1 and x_2). Different simulations show that this non-periodic pattern behind the slits changes as a function of thickness of the SiO_2 buffer layer. For example if the SiO_2 layer is 10 μm thick, the non-periodic interference pattern becomes undetectable.

Comparison between measurements and simulations

We will compare the line traces obtained from the measurements for different wavelength to the line traces from the simulations. The standing waves in front of the periodic arrays have been compared already to calculations in table 3.2. For this reason, we will focus here only on the optical patterns inside and behind the arrays.

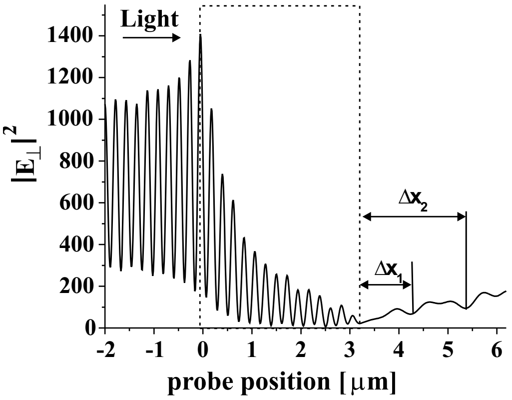

Figure 3.6: Line trace of | $E_\perp$ $|^2$ taken from the simulation at a height of 10 nm above the waveguide. Besides the standing wave, the experimentally observed exponential decay of intensity inside the array is reproduced. Behind the slits, a non-periodic recovery is found.

The period of the interference pattern inside the periodic structures is found to be 220 nm for all wavelengths in both the measurements and the simulations. The array consists of 15 periods and 15 intensity maxima located in the structure are found. For different line traces measured for different wavelength λ_0, we fitted an exponential decay exp(-βx) through the maxima of intensity located inside the periodic structure. The decay rate β is the free fit parameter and x is the probe position with respect to the first air rod or slit.

Figure 3.7 depicts decay rates obtained from fits to the measurement data and to the simulations plotted as a function of λ_0. In the case of the 15 air rods, we fitted an exponential decay through all 15 maxima located in the periodic array. Comparison to the fits obtained with the simulations show good agreement in both the wavelength dependence and the absolute values. Comparing the line trace of the measurement on 15 slits (Fig. 3.4 b) with the line trace the simulation (Fig. 3.6) shows an apparent discrepancy at the location of the first slit. As explained in section 3.1.1, a high intense peak at the first slit is measured and attributed to scattering. A comparable peak is not clearly visible in the simulations. However, the calculated | $E_\perp$ $|^2$ does show a circular pattern originating from the area of the first slit indicating a scattered wave. Note that this scattered light is picked up more readily by our near-field probe than the evanescent tails of | $E_\perp$ $|^2$ above the rest of the structure. The measured intensity at the front of the structure can therefore easily be greater (for equal calculated | $E_\perp$ $|^2$) than above the rest of the structure, because the relative contribution of scattered light compared

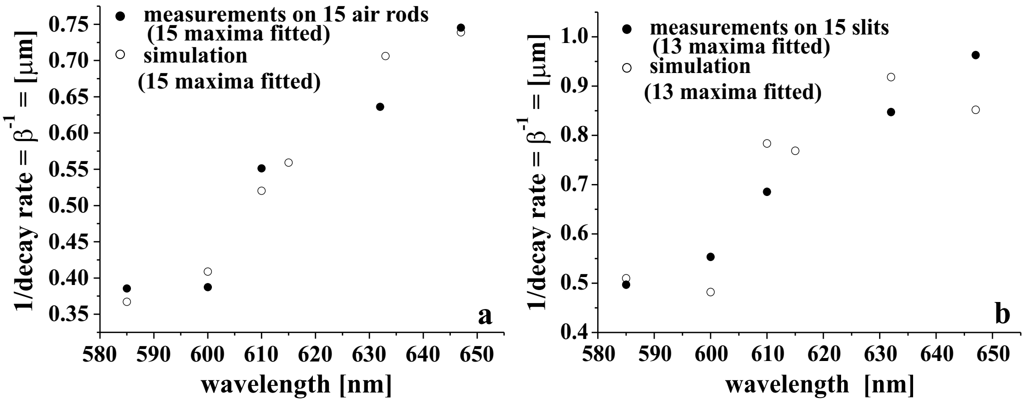

Figure 3.7: Measured and calculated decay rates of intensity inside the periodic array determined for different wavelengths of light coupled into the waveguide. A good agreement between measurement and simulation is found for both structures. A fit with exp(-βx) was performed to line traces as shown in Fig. 3.4 a and 3.4 b. a) For the air rod array structure all 15 maxima were used to perform a fit. b) For the slit structure only 13 maxima were used to perform the fitting to prevent the influence of the strong first peak. Good agreement is found between measurement and simulation for both structures.

to evanescent fields is larger at that position. As a result, we neglect the first and second peak for the comparison of the decay inside the structure. Thus, 13 maxima have been fitted from the measurements on the slit array and from the simulations. Impedance mismatch occurs when light couples from the last air rod or slit to the unperturbed ridge waveguide again. Because of the very low local intensity the inclusion of the last peak makes no difference to the exponential fit. Figure 3.7 b shows the decay rates found, again we compare them with decay rates obtained from the simulations. From the exponential decay rate, we calculate that the periodic structures have losses between 4.4 dB/μm and 11.4 dB/μm. The decay is faster for shorter wavelength, which is typical for scattering phenomena that generally increase with decreasing wavelength. We therefore attribute the wavelength-dependent decay found in our periodic arrays to scattering on the air-material interface.

As a next step we investigate the origin of the maxima and minima in the recovery of light beyond the 15 slits. The Si layer, which lies at a position of - 3.2 μm beneath the Si_3N_4 layer is approximated as a mirror in the simulations. Light scattered into the SiO_2 at the first slit gets reflected on the Si-substrate. Interference takes place in the waveguide behind the slit structure with the light that is directly transmitted by the slit structure. In Fig. 3.8 the distances Δx_i (see Fig. 3.4 b and Fig. 3.6) between the minima occurring and the last slit position are

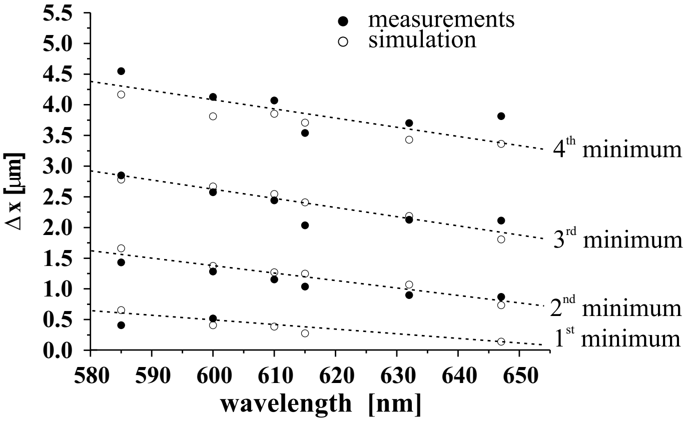

Figure 3.8: Measured and calculated distance between final slit and minima in the recovery pattern behind the periodic array, plotted as a function of wavelength. The recovery of single mode behind the 15 slits involves a non-periodic intensity pattern. The distance between the minima occurring and the last slit are plotted as a function of wavelength. Good agreement is found between measurement (filled dots) and simulation (open circles).

plotted as a function of wavelength λ_0. We find that for increasing wavelengths the distance of the minima to the periodic structure decrease. Good agreement with the simulation is found for the positions of the minima occurring over large ranges behind the slits. As a result, the observation of this non-periodic interference pattern behind the slits is a measure of the thickness of the SiO_2 buffer layer. Normally, layer thicknesses are globally determined by ellipsometry, whereas our measurement tool reveals it locally. In contrast to the slits, the air rod structure scatters a much smaller amount of light to the direction of the Si-substrate and no oscillations in the recovery are found there. The observed scattering towards lower substrate layers and subsequent reflections by those layers may have serious consequences for optical circuits based on photonic crystals.

3.2 The phase evolution of scattered light and singularities

In the first part of this section, we will present the phase measurements performed on the 15 air rod structure. The measurement reveal interference effects as well as local material properties. In the second part of this section, we demonstrate the three-dimensional measurement mode of the photon scanning tunnelling microscope. Phase singularities occur, when light with different wavevectors but equal optical frequencies, e.g., different waveguide modes, interferes destructively. The shape evolution of a phase singularity is visualised as the relative contributions of the interfering modes changes by altering the height of the probe. Finally, we analyse the amplitude and the phase of light scattered from a waveguide by two slits and show how to distinguish between guided and scattered light.

3.2.1 Interference around 15 air rods

Our photon scanning tunnelling microscope measures not only the optical amplitude of light, but by using the heterodyne interferometric detection scheme the phase evolution inside the photonic structure is visualised. From the measurement, we obtain the cosine of the phase of light propagating through the structure (Eq. 2.4). Figure 3.9 shows a map of the cosine of the phase of the light around the 15 air rod structure. The periodic air rod array is located in the centre of the image. Light of $\lambda_0 = 632.8\,\mathrm{nm}$ propagates from the top of the image to the bottom. A wealth of different phase patterns is observed. The whole image contains all the information of contributing modes, which have various wavevectors (different spatial directions and different absolute values), even if they are leaky or scatter out of the confining layer. In the upper half of Fig. 3.9 the optical wavefronts of the fundamental waveguide mode are visible as flat phase fronts. With a Fourier analysis, the period of the wavefronts is found to be $439 \pm 4\,\mathrm{nm}$, which corresponds to the wavelength of light in the waveguide structure. Figure 3.9 also shows circular waves superimposed on the plane wavefronts. These circular waves have their origin in the centre of the image, where the air rods are located. Scattering of incoming light takes place at the air rod array and generation of circular waves takes place. As discussed earlier, these circularly shaped waves contribute to the change in modulation depth of the standing wave in front of the periodic array.

Due to interference between the incoming light and circular waves with origin in the centre of the image, different phase patterns are produced. In the upper part of the image we find jumps in the phase. They are a result of interference of light that propagates in almost opposite directions (with a crossing angle close to π) and their position changes parallel to the plane wavefronts during a single oscillation of the optical field. In the lower part of the image phase singularities are observed. They occur when different modes that propagate in the same direction interfere. If the amplitudes of the contributing modes are equal, the modes are out of phase and on the two different sides of this point a different mode has the highest amplitude, then a singularity with zero optical amplitude occurs [82]. Integration of the phase gradient around the position of a singularity results in an offset of the phase value by $\pm 2\pi n$, where the integer n is the so called “topological charge” of the singularity. The “topological charge” of all phase singularities observed in the

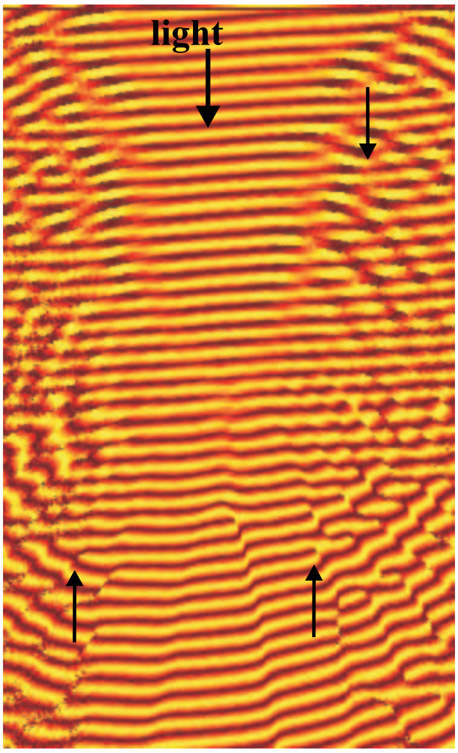

Figure 3.9: The phase evolution of light propagating through the waveguide containing 15 air rods is visualised. In this image, the cosine of phase is depicted. The incoming light propagates from top to bottom. We find circularly shaped waves as well as many phase irregularities in the upper and lower part of the image (a number of which is indicated by an arrow). Due to interference between counter-propagating light (upper part) or co-propagating light (lower part), either phase jumps(upper part) or phase singularities (lower part) occur. Image size: 9.33 μm × 17.23 μm (horizontal × vertical).

lower part of Fig. 3.9 is either +1 or -1.

Figure 3.10 shows a measurement of only the air rod region. Simultaneously, the topographical image (Fig. 3.10 a) and the phase information (Fig. 3.10 b) were detected, while light of $\lambda_0 = 632.8$ nm was coupled into the structure. In front of the air rods (top), the straight lines corresponding to phase fronts of the incoming plane wave are visible. Inside the periodic array a distortion in the phase fronts occurs (region indicated by the dashed oval). Careful investigation of Fig. 3.9 shows the same distortions. This distortion from a straight wave front at the position of the air rods indicates a local change of the refractive index of the material. We find that the wavelength of light inside the periodic structure is 411 ±4 nm, whereas

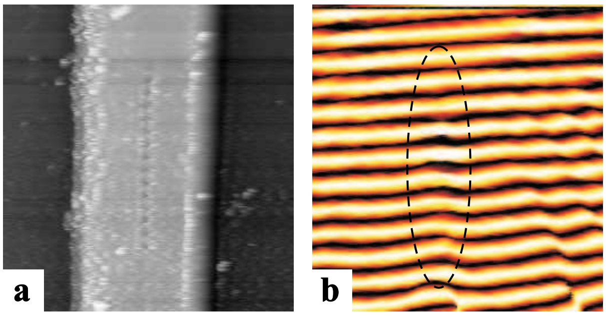

Figure 3.10: Measurement of the nearby region around the air rods. a) Topographical information, which clearly shows the 15 air rods in the waveguide ridge. b) Phase information simultaneously obtained with the topography. The incoming light propagates from top to bottom. On the whole, straight phase fronts with a periodicity of the wavelength of light in the materials are visualised. In the air rod region, however, a perturbation of the phase fronts is observed in the area indicated by the dashed oval. This indicates a local change of the effective refractive index at the location where the air rods are introduced. Image size: $5\,\mu\text{m} \times 4\,\mu\text{m}$.

the supported mode of the waveguide structure (in front of and beyond the air rod array) has a wavelength of 439 ± 4 nm (Fig 3.9). Thus, a shortening of wavelength by 6 % takes place inside the air rod region. After $4\,\mu$m, a shift of almost 200 nm between phase fronts of light inside the air rod region in relation to phase fronts of light that propagates left and right side along the air rods has developed. This shortening in wavelength is remarkable. It implies an increase in the effective refractive index, whereas a lower effective index of refraction was expected due to the introduction of the air rods. Until now, no obvious explanation of this wavelength shortening is found. Due to the periodic structure, the dispersion relation can show regions with increased refractive index. We suggest that due to such anomalous dispersion of light inside the array, a shortening in wavelength takes place. To understand and confirm this assumption, further three-dimensional calculations are needed.

To analyse the complex phase pattern of Fig. 3.9 in more detail, we performed a two-dimensional Fourier transformation analysis. We considered the product of the measured amplitude and the cosine of the phase as shown in Fig. 3.11 a. Interference between incoming light and circularly scattered light is clear. Furthermore, the intensity is mainly confined to the waveguide. Beyond the 15 air rods, two beams scattering out of the waveguide are observed. In between these two beams, an increasing amplitude due to the recovery of light to the waveguide mode is clearly observed.

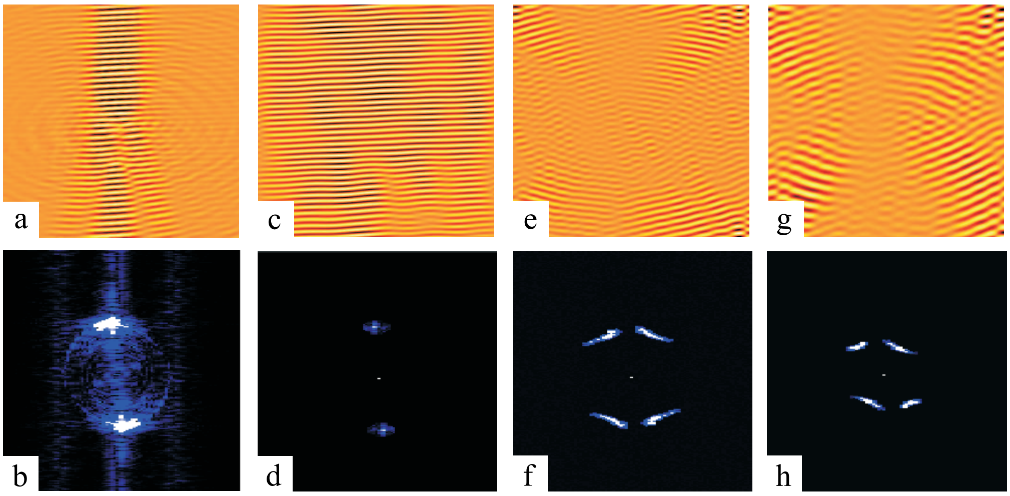

Figure 3.11: Two-dimensional Fourier analysis of the scattering around 15 air rods. a) shows the original data: $A \cdot \cos\phi$. b) gives the spatial frequencies as given by the intensity of the two-dimensional Fourier transformation of a). For a detailed analysis, we have separated the features found in the Fourier transform of b). The three dominant features are shown in d), f) and h). To see the contributing details clearly, different intensity normalisation was used for b), d), f) and h). Investigating those components by Fourier back transformation untangles in all three cases plane waves, which propagate under different angles. Figs. c), e) and g) correspond to d), f) and h), respectively. c) shows plane waves under an angle of 0 degrees, which represent the incoming plane waves propagating through the structure. e) reveals plane waves propagating under an angle of 15 degrees and g) depicts plane waves propagating under an angle of 21 degrees. The image sizes of a), c), e) and g) is $9.33\,\mu\text{m} \times 17.23\,\mu\text{m}$. Images b), d), f), and h) show an area of $10.7\,\mu\text{m}^{-1} \times 11.6\,\mu\text{m}^{-1}$.

In Fig. 3.11 b, shows the intensity of the two-dimensional fourier transform of the original measurement presented in Fig. 3.11 a. A spatial frequency regions is pronounced, which represent the directions of forward and backward propagation. In addition, two concentric rings can be seen in Fig. 3.11 b. To investigate the details we use Fourier filtering, where different areas selected in the frequency domain are used to reconstruct a fourier filtered image. We split the complex pattern of Fig. 3.11 b into the three main contributions shown in Fig. 3.11 d, 3.11 f and 3.11 h. The first component contributing to Fig 3.11 a is a plane wave ($\lambda = 439 \pm 4\,\text{nm}$) over the whole image shown in Fig. 3.11 c. Fig. 3.11 c is the fourier filtered image produced by using the selected area shown in Fig. 3.11 d. In the same way, Figs. 3.11 e and 3.11 g are produced by inverse Fourier transformation of Figs. 3.11 f and 3.11 h, respectively. Figures 3.11 e and 3.11 f show plane waves propagating under discrete angles away from the centre of the image. We find for the waves shown in Fig. 3.11 e an angle of 15° compared to the top-down propagation direction. From the spatial frequency found in Fig. 3.11 f, we calculate an effective refractive index of these waves of 1.20 (corresponding to a wavelength $\lambda_{scattered} = 527\,\text{nm}$). Figure 3.11 g shows plane waves of a refractive index of 0.90 (corresponding to a wavelength $\lambda_{scattered} = 703\,\text{nm}$), which propagate under an angle of 21.5°. Comparing the refractive indices found for the plane waves with the refractive indices of leaky modes of the slab gives a reasonable match (some leaky slab modes: TE_{07}: $\text{n}_{eff} = 1.233$, TE_{10}: $\text{n}_{eff} = 0.980$).

3.2.2 Shape evolution of a phase singularity in space

In the previous section, we have demonstrated how interference of propagating waves builds up a complex phase pattern. On different locations, so-called phase jumps and phase singularities were observed. Using the three-dimensional measurement mode, we now investigate the shape evolution of such phase patterns as a function of distance to the surface. While increasing the tip to sample separation, the ration between the amplitudes of the contributing changes.

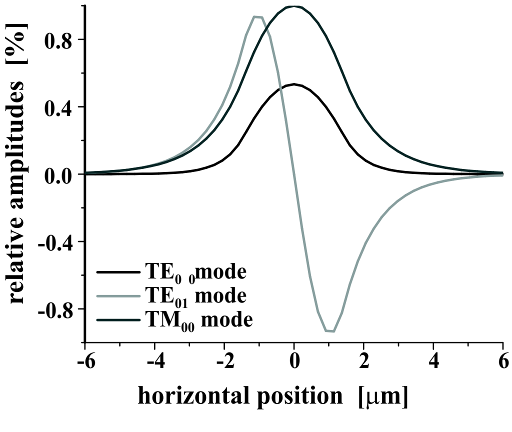

Figure 3.12: Mode profiles of the supported waveguide modes. The relative amplitudes between the modes are 0.53 for TE_{00}, 0.93 for TE_{01} and 1.00 for TM_{00}. This combination of mode amplitudes is used for Figs. 3.13 c and 3.13 d.

To produce a phase singularity in a controlled way, we use a ridge waveguide structure that supports different modes. The waveguide ridge has a height of 4 nm and is 3 μm wide. A slab layer of $110 \pm 5\,\text{nm}$ thickness surrounds the waveguide ridge. The mode profiles of the supported TE_{00}, TE_{01} and TM_{00} modes in the waveguide are depicted in Fig. 3.12. From these profiles we determine the full width at half maximum (FWHM) of the modes. In addition, we calculate the effective refractive index n_{eff} of the modes [79]. The decay lengths into air (z-direction) is calculated with

$$\kappa = \sqrt{\frac{1}{\varepsilon_{eff} - \varepsilon_{air}}} \cdot \frac{\lambda_0}{2\,\pi}. \tag{3.2}$$

The values obtained for the supported waveguide modes are summarised in tabel 3.3.

mode	n_{eff}	κ [nm]	FWHM [μm]
TE_{00}	1.6162	79.82	2.61 ± 0.08
TE_{01}	1.6109	80.64	3.91 ± 0.1
TM_{00}	1.4713	93.47	3.20 ± 0.08
TM_{01}	1.4682	93.69	21.31 ± 0.1

Table 3.3: Specification of the supported waveguide modes. The first column gives the effective index n_{eff} of the modes. The second column gives the decay length κ of the evanescent field away from the waveguide surface into air. The third column gives the full width at half maximum (FWHM) of the different modal field distributions, determined from calculated mode profiles.

A phase singularity occurs at the position where two modes have equal amplitude and are 180° out of phase. Destructive interference between these modes occurs and when on either side of that position different modes have the highest amplitude. Such phase singularities have been observed and described earlier [82]. The field components of TE and TM polarised modes are perpendicular and therefore decoupled. As a result, interference only takes place between modes of the same polarisation. However, we observe interference between TE and TM polarised light. Interference occurs not in the waveguide itself, but due to mixing of the field components while picking up the light with the near-field probe. This interference has been called "quasi-interference" [83].

The mixing of polarisation is a useful side effect which enables to distinguish directly which modes are present in the waveguide. Note that, interference between modes of the same polarisation as observed in section 3.2.1 is real and takes place in the waveguide structure itself.

Mode beating between three different modes (TE_{00}, TE_{01} and TM_{00}) is shown in Fig. 3.13. The PSTM measurements are performed with light of $\lambda_0 = 632.8$ nm. Figure 3.13 a shows the optical amplitude of light propagating from left to right.

The phase information is depicted in Fig. 3.13 b. Clearly, phase singularities are observed at locations where the amplitude of the field is zero. In Fig. 3.13 c and Fig. 3.13 d, calculations of the optical field and phase are depicted, respectively. The calculations are based on interference of the contributing modes and reproduce both the intensity pattern and the phase information.

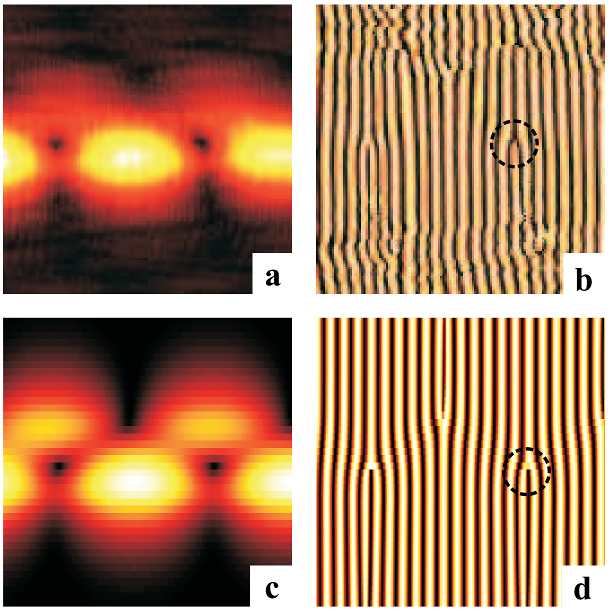

Figure 3.13: Quasi-interference between a TE_{00}, a TE_{01} and a TM_{00} mode. a) and c) show the measured and calculated local amplitude, respectively. b) and d) show the measured and calculated local cosine of the optical phase, respectively. Clearly, at the position where the optical field is zero, a phase singularity is present (dashed circles). Image size: 8.6 μm × 3.8 μm.

We will now focus on the singularity pointed out with a dashed circle in Fig. 3.13 b and Fig. 3.13 d and investigate this singularity at different planes parallel to the surface. Fig. 3.14 shows the measurements (top images) and simulations (bottom images) at three different heights: $z \sim 10$ nm, $z = 100$ nm and $z = 180$ nm. No visible changes in the shape of the phase singularity is observed as the tip to sample separation increases. This observation is reproduced with calculations based on the optical values given in table 3.3. The fact that the shape and position of the singularity does not change indicates that the relative ratio between the amplitudes of the contributing modes hardly changes as a function of tip to sample separation.

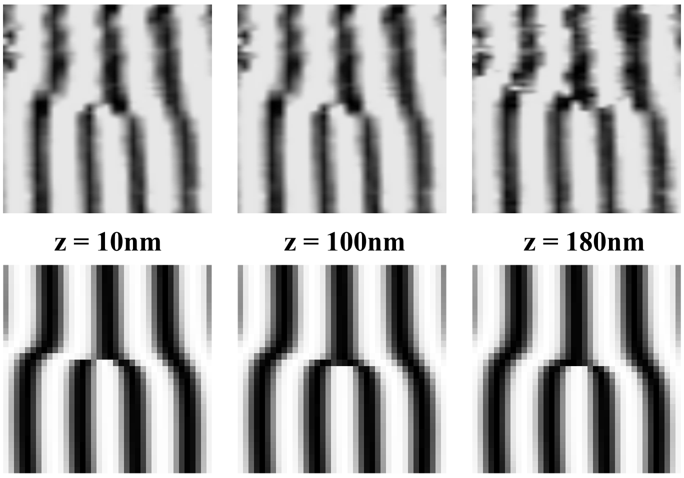

Figure 3.14: Evolution of phase singularity in space. The top images are measurement and the bottom images represent calculations. The singularity does not change in shape nor move in position, as the tip to sample separation increases. The calculation reproduces the experiment. Image size: $4.0\,\mu\text{m} \times 1.5\,\mu\text{m}$.

Through a change in the incoupling of light to the waveguide, we are able to excite a TM_{01} mode. This mode gives rise to a completely different interference pattern and the development of a new phase singularity. Figure 3.15 shows the measurements observed for different tip to sample separations ranging from $z = 10\,\text{nm}$ to $z = 180\,\text{nm}$. The relative amplitudes of the four contributing modes change in such a way, that at a distance of $z = 90\,\text{nm}$ two phase singularities are created.

3.2.3 Evanescent and scattered fields around two slits

The potential of three-dimensional imaging becomes apparent when investigating a strongly scattering structure. Two slits have been milled by FIB in a waveguide (geometry of the waveguide is the same as in sections 3.1). The width of the slits is 110 nm and the centre spacing is 220 nm. For our three-dimensional investigations, we used light of a wavelength of $\lambda_0 = 632.8\,\text{nm}$.

Figure 3.16 shows the topographical image and the optical signal in the plane perpendicular to the sample surface and along the waveguide axis. Light propagates from left to right. In the topographical image (Fig. 3.16 b), the two slits in the centre of the scan range are clearly resolved. In the optical image in Fig. 3.16 b, a standing wave is observed in front of the two slits (left side of the image). Inter-

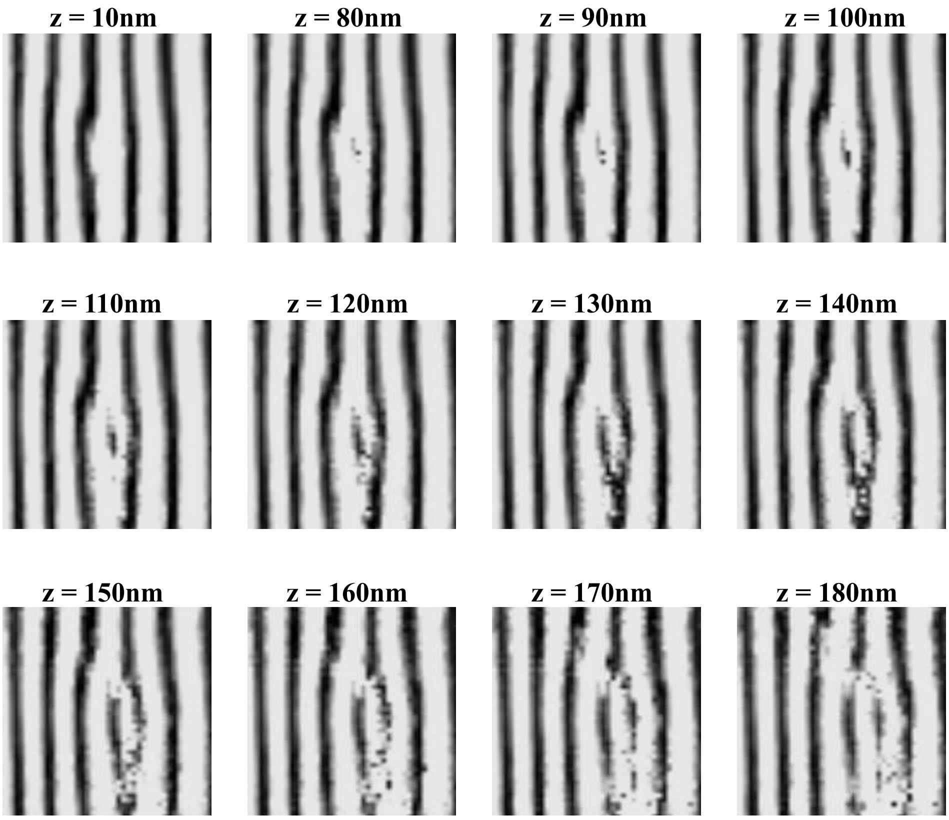

Figure 3.15: Evolution of phase singularities for different heights above the surface. Two singularities develop as the distance between probe and surface is about 100 nm. Increasing the tip to sample distance, the singularities move in position away from each other in opposite directions. They also change in shape at a distance around 160 nm. Image size: $5.8\,\mu\text{m} \times 8.4\,\mu\text{m}$.

ference between incoming and reflected light at the slits builds up a standing wave of periodicity of 216 ± 10 nm. Furthermore, the intensity of light in the waveguide is visible up to 300 nm away from the waveguide. Four distinct beams emanating from the two slits are apparent in the optical amplitude image. To determine the scattering angles of these beams, the amplitude is measured along a circle with its origin at the slits (indicated in Fig. 3.16 b). The angular amplitude distribution has been determined for two different circle radii; $\mathrm{r} = 1.25\,\mu$m and $\mathrm{r} = 0.25\,\mu$m and is depicted in Fig. 3.16 c. The angles are given with respect to the transmission direction, which is chosen to be 0 °. For a radius $\mathrm{r} = 0.25\,\mu$m, the amplitude distribution is rather uniform. This can be expected, since the image is still dominated

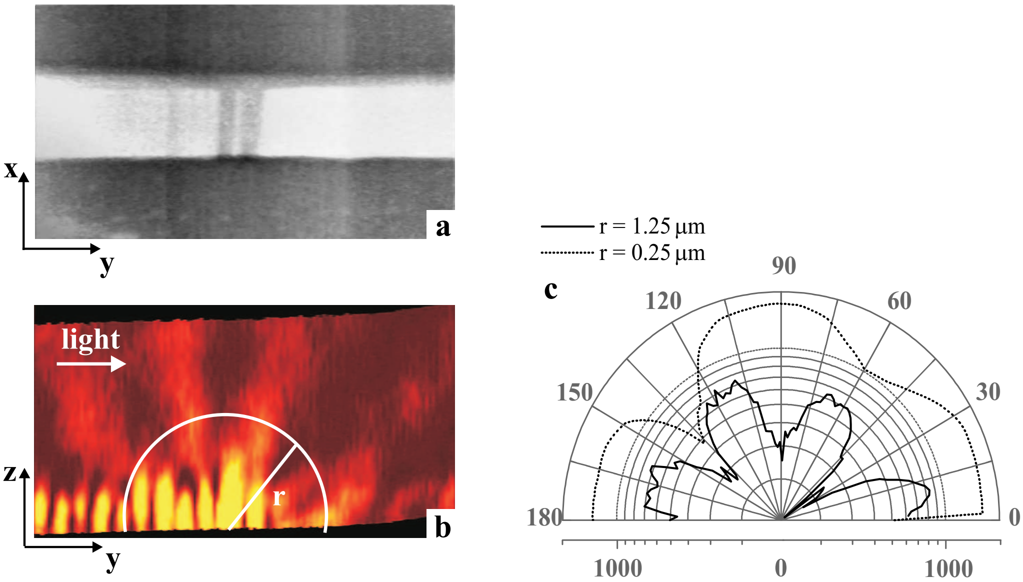

Figure 3.16: a) The measured topography in which the waveguide ridge and the two slits are clearly recognised. b) The amplitude of the light above the two slits. The slits are located at the centre of the drawn curve. This curve depicts a line of constant distance to the slits. c) The amplitude as a function of the angle with respect to the propagation direction for different distances to the centre of the slits (logarithmic scale). Four different peaks in the scattered light can be distinguished. The image sizes in x-, y- and z-direction are 4.3 μm, 6.0 μm and 1.5 μm, respectively.

by evanescent field components. For a larger radius, the scattered beams become clearly recognisable. From the distribution, we find the scattering angles of the distinct beams to be: 11 °, 61 °, 116 ° and 166 °.

Simultaneously with the optical signal, the phase information in all three dimensions was obtained. Figure 3.17 depicts three different planes of which the orientations are given with respect to the x-, y- and z-axes. Fig. 3.17 a presents the measurement in the x-y plane, which is the top view to the waveguide (z-direction). In Figs. 3.17 a and 3.17 b, light propagates from the left to right. The straight wavefronts are more pronounced inside the waveguide region, whereas outside of the waveguide (top and bottom), the noise becomes dominant over the signal. We determine the wavelength of the light inside the waveguide at different positions. In front of the slits, a wavelength $\lambda_{TE_{00}} = 423 \pm 17$ nm is found and the wavelength determined behind the slits is found to be $\lambda_{TE_{00}} = 419 \pm 17$ nm, both in good agreement with the wavelength of the fundamental mode ($\lambda_{TE_{00}} = 433$ nm). The dashed white lines indicate the axis, along which the other two image planes

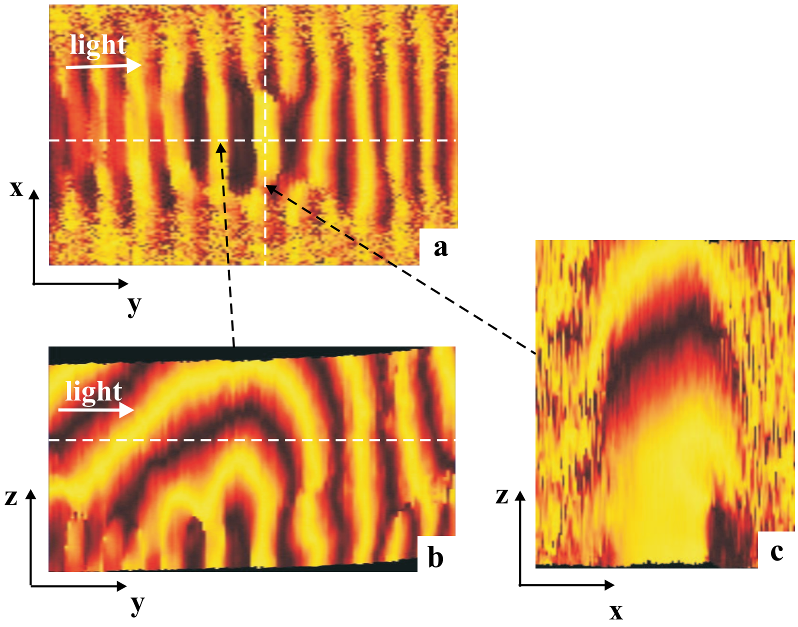

Figure 3.17: Different cuts through the measurement of cos(φ) on the waveguide with two slits. a) cosine in the same plane as Fig. 3.16 b. b) the cosine of the phase measured at the surface. The white lines indicate the positions of the planes shown in the other figures. c) the cosine of the phase across the waveguide. The image sizes in x-, y- and z-direction are 4.3 μm, 6.0 μm and 1.5 μm, respectively.

(Fig. 3.17 b and 3.17 c) are oriented. The image plane in Fig. 3.17 b is the same as for the optical signal in Fig. 3.16 a. Again, we find straight lines away from the waveguide, which are visible up to 300 nm. The evanescent field does not have a real wavevector in the z-direction, but only an imaginary part. As a result, the effective optical path length of the signal branch in the Mach-Zehnder interferometer does not change as long as the evanescent waves dominate the pick up signal. This is more clear in Fig. 3.17 c, where for a plane perpendicular to the waveguide a straight wavefront is observed. At a height of roughly 900 nm, the phase fronts of the scattered waves become dominant. The position of the two slits is roughly in the centre of the image. We observe, that light scatters strongly out of the two sub-wavelength slits and builds a roughly circular wave in the y-z plane. in front of the slits we determine that the interference pattern has a period of 575 ± 45 nm. After the slits, a shorter period of 453 ± 45 nm is observed. Figure 3.18 shows the phase information in a plane at a tip to sample separation of ∼ 1.2 μm (indicated by dashed, white line in Fig. 3.17 a). Again, a difference in periodicity is found

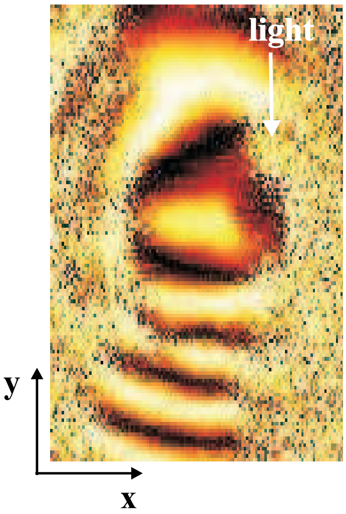

Figure 3.18: Cosine of the phase at a plane at roughly 1.2 μm above the surface. We observe a larger periodicity of the wavefronts in front of the slits (upper part) than behind the slits (lower part).

between the wavefronts in front of the slits and those behind.

Apparently, in front of the two slits, light is scattered into propagating waves in air ($\lambda_0 = 632.8$ nm) dominates over evanescent contributions. Whereas behind the slits, the scattered light is still dominated by interference with light inside the waveguide, and therefore a shorter wavelength compared to λ_0 is observed.

3.3 Conclusions

We have presented PSTM as a powerful technique for characterising complex photonic structures. Simultaneous with the topography, the optical field distribution is mapped with a resolution of roughly 50 nm. A quantitative analysis of the interference pattern in front of a single slit reveals a standing wave resulting from the interference between incoming and backscattered light. Moreover, a Fourier analysis indicates scattering into leaky modes.

Investigations on two different photonic structures (15 air rods and 15 slits milled into the ridge of a conventional waveguide) are performed. From the optical intensity distribution measurement we find a wavelength-dependent exponential decay rate inside the periodic structures. A faster decay is found for shorter wavelength. The wavelength dependence is therefore mainly attributed to losses arising from scattering processes. The scattering behaviour of the two structures has been found to differ. For the air rod array, we find strong scattering into leaky modes of the waveguide. This leads to a change in modulation depth of the standing wave close to the air rod array. The slit structure scatters more efficiently into the SiO_2 buffer layer, which leads to an unexpected interference pattern behind the slits, causing a wavelength-dependent recovery behind. Simulations confirm that at the first few slits much light is scattered into the SiO_2 layer, which is subsequently reflected at the SiO_2-Si interface. As a result a non-periodic interference pattern is observed behind the slit structure. This finding has implications for photonic crystal structures based on silicon on insulator technology as it can lead to unwanted crosstalk.

Our technique visualises both the amplitude and the phase of local fields inside the structures. Investigation of the phase evolution of light scattered around the 15 air rods reveals circularly scattered waves with their origin in the air rod region. Due to interference between these circularly scattered waves and light propagating in the structure a network of phase jumps and phase singularities is built up. Local observations of the phase around the air rods show a change of the effective refractive index of the waveguide.

Using the three-dimensional measurement mode, we investigated the evolution of the phase for increasing tip to sample separation. It is easily recognised, that the phase should not change as a function of distance, when evanescent light is measured. Singularities exemplify the phase behaviour resulting from interference of different modes in a waveguide structure. Due to different exponential decay lengths, the relatives amplitudes between the modes changes as a function of probe to sample distance. As a result, the creation of a pair of singularities was observed.

On the example of two slits milled in a waveguide, we can distinguish scattered light from guided (evanescent) light. Four distinct beams emanating from the slits are seen in the optical field distribution. Light is scattered from the two slits and circular waves are observed at horizontal planes above the waveguide.

All the detailed optical properties in and around sub-wavelength structures can only be obtained with a near-field setup. We found information on local light scattering and phase shifts, which would have remained hidden using far-field methods. We anticipate that our technique will allow the mapping of wave functions of local photon states inside one- or two-dimensional photonic crystals.

Chapter 4

Coupling to resonant modes of 2D photonic crystal slabs

Free-standing two-dimensional photonic crystals slabs are investigated by far-field reflectivity measurements. The in-plane stopgap along the crystalline Γ - K *direction is revealed directly. The technique is used to probe the coupling to resonant modes of the photonic crystal slab by angle-dependent reflectivity spectra on the top side of the slab. Sharp resonance features are observed in the spectra, which change their position and shape as a function of incident angle. From the frequency at which the resonances occur, the dispersion of the resonant modes is reconstructed. We investigate in detail the line shapes of the resonance features, which are determined by interference of light propagating along different pathways. The line shape analysis reveals a phase shift occurring in one of the pathways when* $k_{//}$ *is varied.*

4.1 Far-field characterisation of a photonic crystal slab

Far-field reflectivity spectra measurements enable a good characterisation of the optical properties of a photonic crystal slab. By probing the in-plane reflectivity at the end facet of the slab the stopgaps of the crystal are revealed. These stopgaps are located in the guided mode regions, which are the modes found in the dispersion relation below the light line. But by far-field methods not only these guided mode properties can be probed. Angle-dependent reflectivity measurements (also called specular reflectivity measurements) on top of the photonic crystal slab, enable coupling to resonant modes. In the dispersion relation, the resonant modes are located above the light line. From the spectral position of the resonances observed, the band diagram above the light line is reconstructed directly from the measurements. Overall, the two different reflectivity methods (in-plane and angle-dependent) give a complete picture of the dispersion relation and describe the optical properties of the photonic crystal slab.

In this chapter, we show both, in-plane and specular reflectivity spectra obtained on a free-standing photonic crystal slab. Details of the photonic crystal slab investigated here are given in section 1.2.2. The setup used was described in section 2.2.2.

4.1.1 In-plane reflectivity spectra

The stopgap along the Γ - K crystalline direction is probed by in-plane reflectivity spectra. Reflection in the plane of the crystal slab is measured by focussing white light to a spot with a diameter of roughly $40\,\mu$m at the endface of the membrane. In this way, the reflected signal is increased sufficiently to measure. Due to the focussing of the beam, a range of wavevectors is incident besides the wavevector parallel to the Γ - K direction. The angular spread is $\pm\,23.6°$, which is calculated for light propagating in air. For light propagating in the crystal the angular spread is $\pm\,12.6°$ (see section 2.2.1). Due to the small angular spread different crystalline directions are probed in the reflectivity spectra.

The measured reflectivity spectra obtained for two different polarisations of incident light are shown in Fig. 4.1. The two different polarisations used are TE (E-field in x-y plane) and TM (H-field in x-y plane), which probe for our slab geometry the properties of the even and odd modes in the band structure, respectively. The spectra were normalised to the spectra of the Xe-lamp, which was obtained by reflection on a silver mirror. Afterwards, the maximum value found in the spectral range was set equal to 1. Note that the reflectivity spectrum for TM polarised light was approximately five times less intense than that for TE

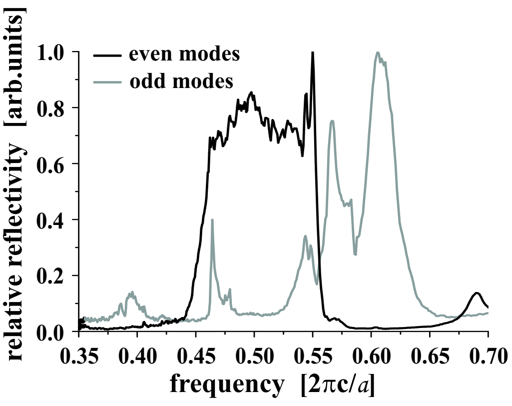

Figure 4.1: Reflectivity spectra obtained for light propagating in the photonic crystals slab (x-y plane). Both spectra, for even and odd modes show ranges of frequencies where strong reflection occurs. These ranges of frequencies are associated with stopgaps along the Γ - K direction.

polarised light. The origin of the lower reflectivity of TM polarised light has not been identified yet.

In the in-plane reflectivity spectra (Fig. 4.1), we find several reflection peaks for TM polarised light. The strongest reflection peak range in frequency from 0.60 to 0.62 and has a FWHM of 4.4 %. In the TE spectrum the a strongly reflected frequency range is found from 0.46 and 0.55. We compare the measurements with the calculations (section 1.1.2). The first row in table 4.1 gives the stopgap range obtained at FWHM from the measurements. The second row summarises the stopgaps along the Γ - K direction found in the simulations. Reasonable agreement is obtained for both polarisations of incident light. For the measured gap of even modes, the FWHM is 0.01 larger than predicted from the simulations. The use of an objective for the measurements results in a spread of available wavevectors $k_{//}$

	measured	calculated Γ - K
TE / even	0.46 - 0.55	0.45 - 0.53
TM / odd	0.60 - 0.62	0.57 - 0.61

Table 4.1: Comparison of measured and calculated stopgaps. The first column gives the measured reflected range of frequencies for both, TE and TM polarised light. The second column gives the values of the stopgaps along the Γ - K crystalline direction for both polarisations of incident light obtained from the calculations in Fig. 1.4 and discussed in section 1.2.2.

(as discussed above). These additional available wavevectors result in a broadening of the gaps. However, the enlargement of the gap should take place at the red shifted band edge and not at the blue shifted as observed in table 4.1. For the stopgap in the odd modes a 0.02 smaller gap is found as well as a blue shift of the measurements compared to the simulations. Assuming an overall blue shift of the measurements compared to the simulations is present, we can corrected for such a blue shift. As a result, the broadening of the stopgaps occurs at the low frequency side. Such a blue shift can have different origins. A slightly smaller thickness of the slab shifts the gap range to higher frequencies (blue shift). Similarly, a slightly different refractive index of the Si_3N_4 shifts the gap. The thickness of the slab as well as the index of the silicon-rich Si_3N_4 were determined experimentally and used as direct input parameters of the simulations. A measured inaccuracy can lead to the discrepancy between simulations and reflectivity measurements.

The slopes at the band edges are rather steep. Normally, fabrication imperfections, such as roughness of the material interfaces and slight variations in periodicity, influence the steepness of the slope at the band edge. The measurements in Fig. 4.1 shows, that the investigated photonic crystal slab produced by laser interference lithography has a high homogeneity. Laser interference lithography has high potential for the fabrication of high quality two-dimensional photonic crystals.

4.1.2 Specular reflectivity spectra

In the band diagram of a photonic crystal slab (Fig. 1.4) three different kind of modes are present: guided modes lying below the light line, resonant modes lying above the light line and a continuum of air modes indicated by the gray area above the light line. In angle-dependent reflectivity measurements coupling of incident light to resonant modes can be investigated, since a resonance feature appears in the spectra. Coupling to a guided modes is only possible, when both the wavevector and the frequency of incoming light match those of the mode.

With our angle-dependent reflection setup spectra for incident angles between $\Theta = 33^\circ$ and $\Theta = 80^\circ$ can be measured. A parallel beam of white light, with a rectangular profile of $300\,\mu\text{m} \times 2\,\text{mm}$, is incident on the photonic crystal slab under an angle Θ. The reflectivity spectra are detected at an angle $-\Theta$. The large beam size decreases diffraction effects.

Specular reflectivity spectra were obtained for both, TE and TM polarised incident light and along the two different crystal directions Γ - K and Γ - M. Figures 4.2 and 4.3 depict the angle-dependent reflectivity spectra measured along the crystal Γ - K direction for TE polarised light and TM polarised light, respectively. The angle of incidence increases from top to bottom in both figures.

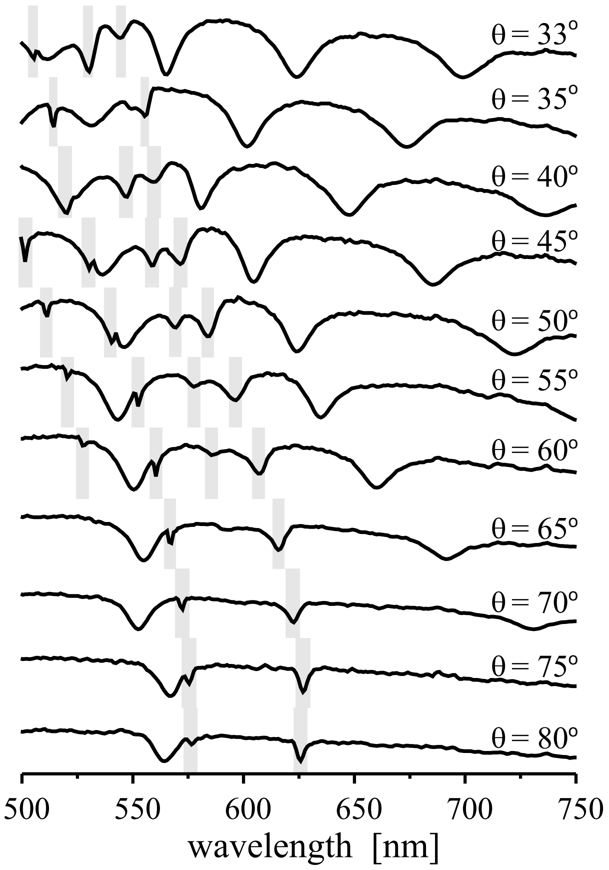

Figure 4.2: Specular reflectivity spectra for TE polarised light measured along the crystal direction Γ - K. Background modulations due to Fabry-Perot interference in the 3.2 μm air gap underneath the photonic crystals slab are observed. Superimposed on this background, sharp resonance features can be seen (indicated by gray areas). The resonance features shift in position of wavelength as a function of the incident angle Θ.

The spectra show a background modulation upon which much narrower resonance features are superimposed. The background modulations are stronger for small incident angles Θ. They are Fabry-Perot fringes arising from reflections in the air cavity of 3.2 μm in between the Si_3N_4 membrane and the Si-wafer. The sharp features superimposed on the smooth background shift with increasing incident angle Θ upwards in wavelength by up to 81 nm. The features have different line shapes, such as minima, maxima and dispersive line shape. A closer investigation reveals that the features observed for TE polarised incident light (Fig. 4.2)

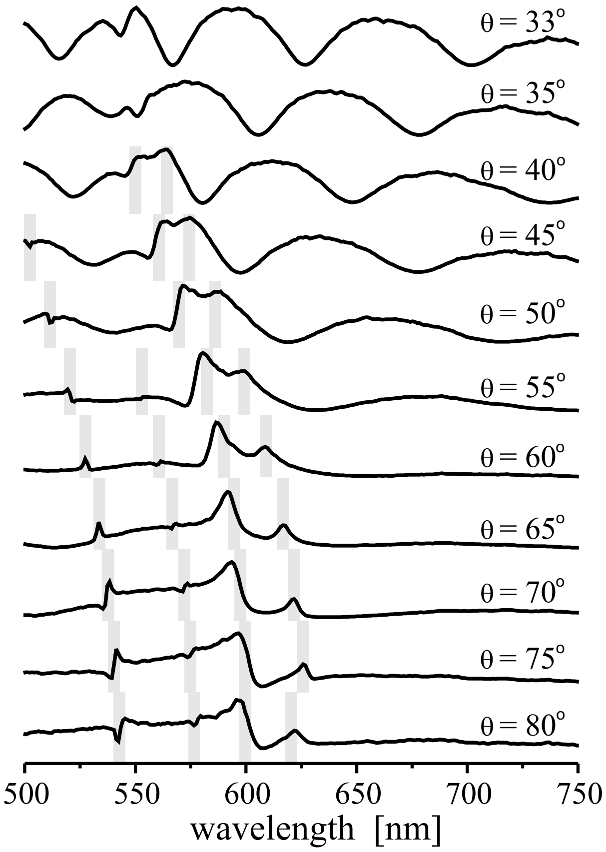

Figure 4.3: Specular reflectivity spectra for TM polarised light measured along the crystalline direction Γ - K. Similar as in Fig. 4.2, a background modulation upon which sharp resonance features are superimposed can be seen. The resonance features (indicated by gray areas) shift in position of wavelength as a function of the incident angle Θ. Moreover, the shape of the resonance features changes with angle.

are always minima, whereas the features observed for TM polarised incident light (Fig. 4.3) exhibit all the possible dispersive line shapes. Measurements along the Γ - M direction were also obtained for both polarisations. Qualitatively, these spectra look similar to those shown in Fig. 4.2 and Fig. 4.3. For this reason, the raw data is not presented here, but is included in the analysis.

On one-dimensional structures (e.g., [64], [84]) and on two-dimensional structures with square lattice (e.g., [65], [66]) or with triangular lattice (e.g., [85]), resonance features similar to those depicted in Figs. 4.2 and 4.3 have been observed. However, in all those measurements no difference in the shape of the features related to the polarisation of the incident light was observed. Moreover, the resonant features observed in our study are narrower than those observed in previous studies. The width of the resonances depends on the vertical confinement of the mode, as confirmed by simulations [64]. A strongly confined mode shows a narrower resonance than a weakly confined mode. For this reason, the observation of narrow features indicate that our structures have a high confinement of the modes due to the symmetric layer system and that little scattering occurs thanks to the long range perfect order in our crystal. The large area of our freestanding membrane gives rise to a high angular resolution in the reflectivity spectra. Note that the narrow features are directly broadened by a detection system with a limited angular resolution, since then averaging over different angles takes place.

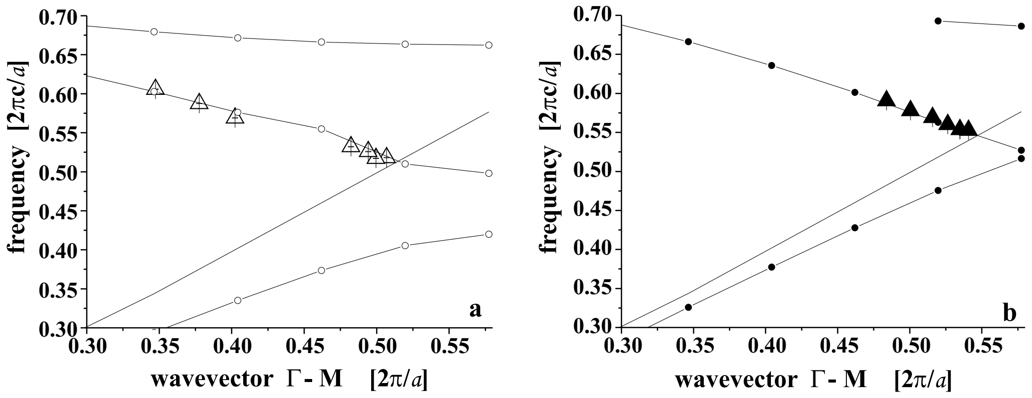

Figure 4.4: Reconstructed dispersion of the resonant modes. The spectral position of the observed resonance features was determined by fitting the line shape of the resonance. a) represents the even modes (open triangles) and b) the odd modes (filled dots). The results are in perfect agreement with the band diagram calculations, depicted as open and filled circles.

The spectral position of the resonances in reflectivity spectra is determined by a fit of the resonance line shape, which will be discussed in the next section. In principle, the position of the resonances could also be determined manually. Here, we use the resonance frequencies obtained from the fit to reconstruct the dispersion of the resonant modes using Eq. 2.6 since this is more accurate. In Figures. 4.4 and 4.5 the dispersion relations along the crystalline directions Γ - M and Γ - K are depicted, respectively. The dispersion relation obtained from the specular reflectivity spectra are plotted together with dispersion obtained from the band diagram calculations in section 1.1.2. Figs. 4.4 a and 4.5 a represent the even modes corresponding to TE polarised incident light (open symbols). Figs. 4.4 b and 4.5 b represent the odd modes corresponding to TM polarised incident light

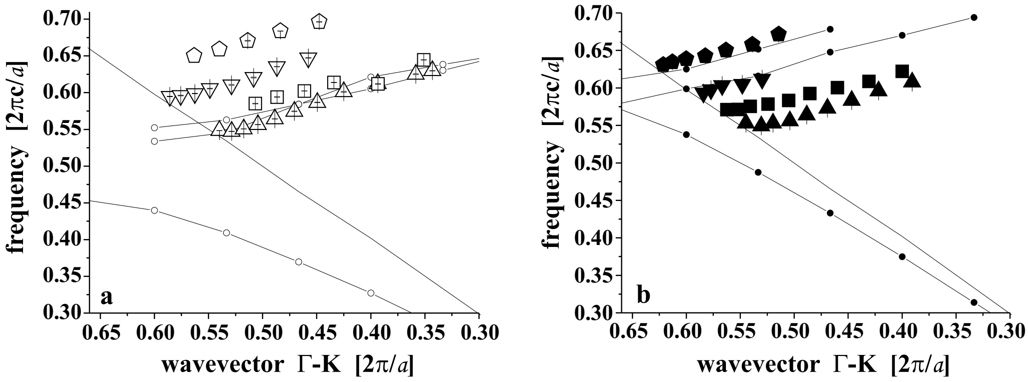

Figure 4.5: Reconstructed dispersion of the resonant modes. The spectral position of the observed resonance features was determined by fitting the line shape of the resonance. a) represents the even modes (open symbols) and b) the odd modes (filled symbols). For both polarisations, two modes perfectly match two calculated modes (open and filled circles), whereas two additional modes are observed in the measurements, which are not explained by the calculations. We refer to the modes as first order (triangles), second order (squares), third order (inverted triangles) and fourth order (pentagon).

(filled symbols). We find perfect agreement between measurements and simulations in the dispersion along the Γ - M direction. For the measurements along the Γ - K direction in Fig. 4.5 we find four different dispersion bands from the measurements. From these four bands, two are predicted theoretically for each polarisation, i.e. the first and second band for even modes and the third and fourth band for odd modes. It turns out, that the four different modes observed for both polarisations are the same, which becomes obvious, when the results of Fig. 4.5 are plotted together in one graph (see Fig. 4.6). This overlap is due to polarisation mixing which was observed earlier by [64]. It has been suggested [64] that higher order bands contain high momentum guided waves due to the folding into the first Brillouin zone. Mode mixing occurs when low momentum unfolded components are mixed into this high momentum by the patterning of the photonic crystal. As a result, the mode appears with opposite polarisation to the general character of the band. The observation of mode mixing points out an important discrepancy between measurements and simulations.

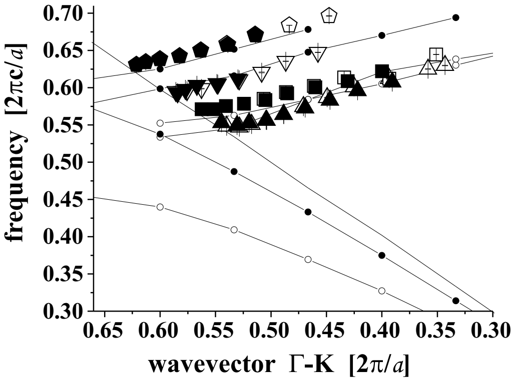

Figure 4.6: Reconstructed dispersion relations of the resonant modes obtained in the specular reflectivity spectra plotted together with the band structure calculation. The open symbols represent the measurements of even bands and the filled symbols the measurements of odd bands. The calculation is represented by open and filled circles. We observe mode mixing between even and odd modes.

4.2 Analysis of coupling to resonant modes

4.2.1 Theory of Fano line shapes

The sharp resonance features observed in the specular reflectivity spectra (Figs. 4.2 and 4.3) exhibit all the properties of dispersive line shapes as described by Fano [86]. Here, we will use the formula proposed by Fano to investigate the coupling of continuum states to the discrete resonant modes of the photonic crystal slab.

In 1961 a theoretical description for resonances that occur in the spectra of inelastic scattering of electrons on Helium was presented [86]. In that case, an electron-beam, represented by a continuum of initial states ψ, is scattered inelastically by a Helium atom. As a result, autoionisation of the Helium can occur or the electrons scatter to an unperturbed continuum of states Ψ_E. The autoionisation of the atom during the scattering produces a resonance in the detected electron spectrum, which is explained by coupling of the initial electron states ψ to a discrete resonant state ϕ. Such a resonance has a dispersive line shape that can be described by

$$f(E) = 1 + \frac{q^2 - 1 + 4\,q\,(E - E_\psi - F)/\,\Gamma}{1 + 4\,(E - E_\psi - F)^2/\,\Gamma^2} \quad , \tag{4.1}$$

where q is the coupling parameter and Γ the spectral width of the resonance. The unperturbed energy level E_ψ is shifted by a discrete energy F to the resonant state

ϕ. As a result, $E_\psi + F$ is the resonance energy level lying within the perturbed continuum of states Φ. The coupling parameter q is given as the ratio of the transition probabilities from an initial state ψ to the discrete resonant state ϕ and to a band width Γ of unperturbed continuum states Ψ_E by

$$\frac{1}{2}\,\pi\, q^2 \;=\; \frac{|\langle\phi\,|\,T\,|\,\psi\rangle|^2}{\Gamma\cdot|\langle\Psi_E\,|\,T\,|\,\psi\rangle|^2} \;\; , \tag{4.2}$$

where T a suitable transition operator. $\langle\phi\,|\,T\,|\,\psi\rangle$ and $\langle\Psi_E\,|\,T\,|\,\psi\rangle$ are matrix elements of the transitions to the discrete resonant state and to continuum states, respectively.

We translate this theory of inelastic electron scattering on atoms to the photonic case for the description of the excitation of the resonant modes observed in our reflectivity spectra. We substitute $E = \hbar\omega$ and $\Gamma = \hbar\gamma$ in equation 4.1. Furthermore, we include some parameters to fit the measurement data properly. We write

$$f(\omega) = S\cdot\left[1+\frac{q^2-1+4q(\omega-\omega_0)/\gamma}{1+4(\omega-\omega_0)^2/\gamma^2}\right] + f_0 + b\cdot(\omega-\omega_0) \;\; , \tag{4.3}$$

where ω_0 is the resonance frequency of the resonant mode, γ is the line width of the resonance, q is the coupling parameter, S is the amplitude of the resonance (a parameter that includes the coupling strength) and f_0 is an offset of data. A background of the data is given by the slope $b\cdot(\omega-\omega_0)$. In our experiment incoming white light describes the initial continuum of states ψ. The resonant state ϕ is determined by the spectral position ω_0, where the sharp features with dispersive line shapes are observed. The detected spectral range of frequencies are the unperturbed continuum states Ψ.

The line width γ of a mode corresponds directly to the lifetime of the mode. Theoretically, a lossless, guided mode has an infinitely small line width γ. This implies that the lifetime becomes infinite. Due to the leakage, resonant modes have a finite lifetime. Moreover, we can relate the line width γ to a quality factor Q of the mode,

$$Q \;=\; \frac{\omega_0}{\gamma} \;\; . \tag{4.4}$$

It is obvious, that a perfectly guided mode has an infinite quality factor.

We illustrate the fitting procedure on two examples of resonant line shapes, shown in Fig. 4.7. The reflectivity measurements for this examples were performed along the crystalline Γ - K direction and at an incident angle of $\Theta = 75°$ (depicted as black lines). The left graph shows the resonance observed for TE polarised incident light and the right graph the resonance observed for TM polarised incident light.

Clearly, a minimum and a dispersive line shape are observed, respectively. The gray lines give the fits obtained with formula 4.3. In both cases, the fit represents the line shapes of the resonances accurately. We find for the minimum in the left graph the resonance frequency at $\omega_0 = 0.547$, the line width $\gamma = 0.003$ and a coupling parameter of q = 0.102. For the resonance in the right graph, we obtain a resonance frequency $\omega_0 = 0.635$, a line width $\gamma = 0.002$ and a coupling parameter q = -1.122. From the two examples, we conclude that equation 4.3 is suitable to fit the measured resonance features.

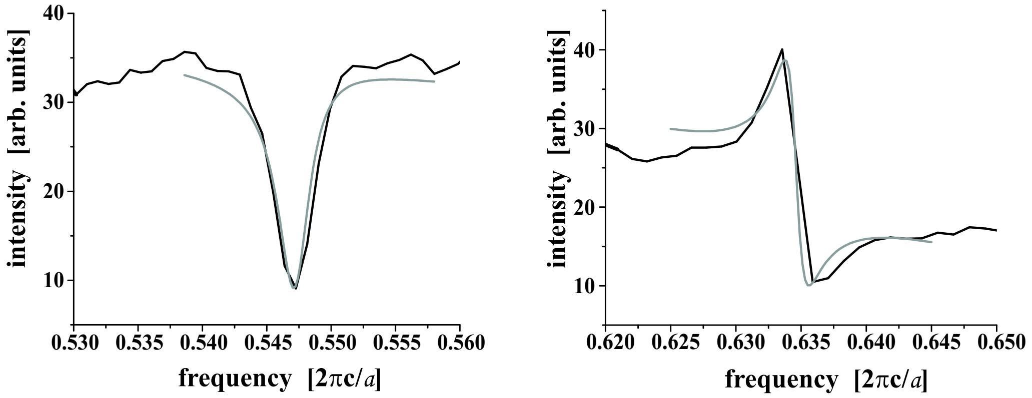

Figure 4.7: Two examples of resonance features obtained in measurements obtained for TE (Fig. 4.2) and TM (Fig. 4.3) incident light at $\Theta = 75°$. The black line represents the measured raw data. The gray line represents the fit obtained by equation 4.3. The fit reproduces the experimental data well. The fit returns the following parameter for the left graph: $\omega_0 = 0.547$, $\gamma = 0.003$ and q = 0.102. For the right graph we obtain: $\omega_0 = 0.635$, $\gamma = 0.002$ and q = -1.122

When two features occur at frequencies close to each other, see for example the case in Fig. 4.3 for the resonances at 600 nm and at 620 nm, we use an adapted function to fit. The sum of two resonances is used to fit those features. Figure 4.8 shows a double resonance feature, observed in the spectrum along the Γ - K direction at an incident angle $\Theta = 75°$ and for TM polarised incident light. The measurement is depicted as black line and the fit is shown as a gray line. We obtain the following fit parameters for the first (left) and second (right) resonance: $\omega_{0,1} = 0.549$, $\omega_{0,2} = 0.571$, $\gamma_1 = 0.006$, $\gamma_2 = 0.011$, $q_1 = -22.115$ and $q_2 = 1.256$. The two resonance features are fitted suitable, even though care has to be taken for the lower frequency one. The coupling parameter seems not to be realistic, which is confirmed by this difference in line shape at the left side of the resonance. Note, that two resonance features close to each other may only be fitted by the function proposed by Fano, if the resonances do not interact with each other [87].

As a result, our adopted fit function, which consists of the sum of two resonance line shapes, provides a good approximation to the measurements as long as the resonances do not interact.

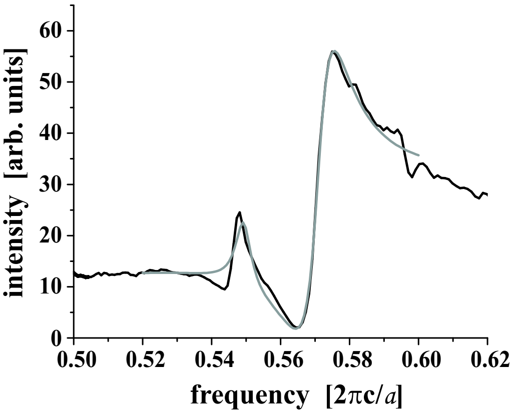

Figure 4.8: Reflectivity as a function of normalised frequency. The black line depicts the reflectivity measurement along Γ - K obtained for TM polarised light with an incident angle $\Theta = 75°$ as a function of normalised frequency. The gray line gives the best "double feature" fit. The parameters found from the fit are: $\omega_{0,1} = 0.549$, $\omega_{0,2} = 0.571$, $\gamma_1 = 0.006$, $\gamma_2 = 0.011$, $q_1 =$ -22.115 and $q_2 = 1.256$.

The function proposed for the analysis of resonances in the energy spectra of electrons is translated to the photonic case. To analyse the observed resonance features in the specular reflectivity spectra, we fit them with either the function 4.3 or an adapted "double feature" fit.

4.2.2 Lifetime of resonant modes and q-reversal

From the fits performed for each resonance found in the specular reflectivity spectra along the Γ - M and Γ - K directions of the crystal for both polarisations, we obtained the parameters ω_0, γ and q, which are the resonance frequency, the line width of the resonance and the coupling parameter, respectively. With Eq. 2.6, the dispersion of the resonant modes has been reconstructed and shown in section 4.1.2. Excellent agreement with the simulation is obtained. In this section, we will discuss the results of the line width γ and the couplings parameter q.

The line widths of the even and odd resonant modes along the crystalline direction Γ - M are depicted in Fig. 4.9. We find for both modes no clear wavelength dependence of the line width. The average line width for the even modes is approximately $\gamma = 0.005$ and for the odd modes roughly $\gamma = 0.001$.

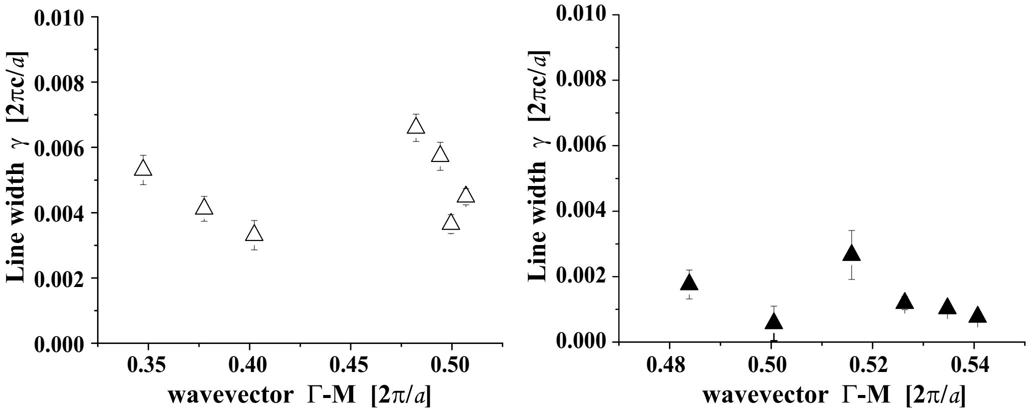

Figure 4.9: Line width γ obtained from the measurements performed along the crystalline Γ - M direction. The left graph (open symbols) presents the even modes and the right graph (filled symbols) the odd modes. The line width shows no clear dependence on wavevector.

We calculate the quality factor Q (Eq. 4.2) of the resonances along Γ - M. We find for even modes a range from 81 to 172 and for odd modes from 214 to 1014. As predicted theoretically (e.g., [88], [63]) resonant modes can have quality factors up to 10^3 or even up to 10^5 (see [89], [90]). The combination of the high confinement of the modes in our symmetric slab structure and the high angular resolution of the measurements allow the theoretical prediction to be reached. Apparently, the quality of the photonic crystal structure is also high.

For the measurements along the Γ - K direction, we observed several resonant modes. To ease the discussion of the line width, they are presented in three subgraphs (Fig. 4.10): one for the lowest resonant mode, one for the second resonant mode and a third subgraph for the third and fourth resonant modes together. For the higher order modes, the width of the resonances does not exhibit a clear dependence on wavevector. We find that γ is slightly wider for the second band as compared to the third and fourth band. For the lowest band we observe a changes in the line width in the Γ - K direction for both polarisation. For decreasing angle of incidence (corresponding to a decreasing value of the wavevector k) down to approximately $\Theta = 50°$ to $55°$ the line width of the resonances increases. For angles smaller than $\Theta = 50°$ (corresponding to $k_{//} = 0.45$), the width of the resonance stays constant.

Again, we calculate the quality factor Q corresponding to the line width γ. The first bands shows quality factors for even and odd modes, ranging from 81 to 214 and from 21 to 103, respectively. For the second bands we find quality factors for even modes in the range between 102 and 139 and for odd modes between 53

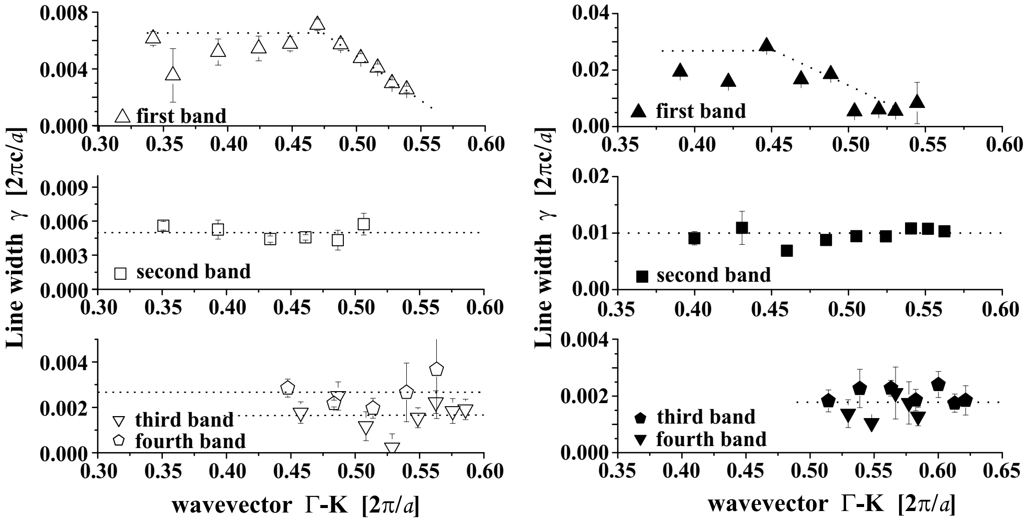

Figure 4.10: The left (open symbols) and right (filled symbols) graph depict the line widths determined from the measurements along the Γ - K direction and for TE and TM polarised light, respectively. The first resonant mode shows an angle dependence of the line width, whereas the higher order modes not. Moreover, the higher the mode is the smaller the line width becomes. The dashed lines act as guides to the eye.

and 87. The quality factor for the third and fourth band of the even modes is found in the order of 177 to 530 and for the odd modes between 265 and 576. From the quality factors obtained, we conclude that modes in higher order bands couple less to the continuum than the lower order bands.

The last parameter obtained from the fit with equation 4.3 is the coupling parameter q. Figure 4.11 and Fig. 4.12 show the coupling parameter for the two crystalline directions Γ - M and Γ - K, respectively. Again, the graphs with open symbols represent the even modes and the graphs with the filled symbols correspond to odd modes. For all measurements obtained with TE polarised incident light, we observe that the value of q varies around zero corresponding to the observation of a minimum in the reflectivity spectra. We attribute the fact that in our measurements for TE polarised incident light only minima occur and no dispersive line shapes to the symmetry (in the z-direction) of our structures. Most measurements reported in the literature were performed on asymmetric structures and no polarisation dependence of the shape of the resonant modes was found.

However, for the TM polarised light a significantly different behaviour of the coupling parameter is observed. Figure 4.11 shows that the coupling parameter actually changes its sign from a value around +1 to a value around -1 with in-

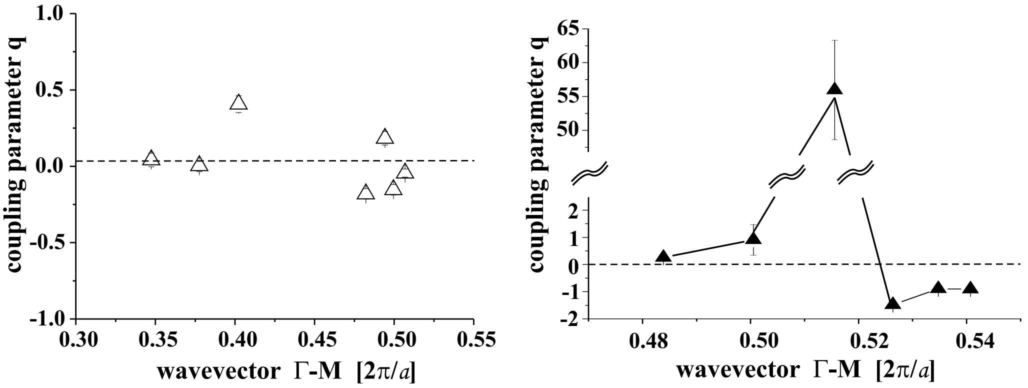

Figure 4.11: Coupling parameter q for the measurements along the crystallin direction Γ - M. For the even modes (left graph), the values of q are around zero, which corresponds to a minima in the spectra. For odd modes (right graph), we observe that the phase of the coupling parameter q changes at $k_{//} = 0.516$.

creasing angle of incidence Θ (increasing wavevector *k*). At an angle of incidence of $\Theta = 65°$ (corresponding to $k_{//} = 0.516$) the coupling constant *q* has a very large value.

Figure 4.12 shows the coupling parameters determined from the measurements performed along the Γ - K direction. For the measurements with TE polarised incident light (left graphs), no large variations in the coupling parameter *q* is observed. The values of *q* is small ($q < 0.45$) for all wavevectors. A similar wavevector dependence of *q* is observed for the third odd band (right graph). However, for the second and fourth band of the odd modes, the *q* - reversal observed in the Γ - M direction is also detected along the Γ - K direction.

For the measurement with TM polarised light along the Γ - K direction the coupling parameters determined for the second, third and fourth band are presented in Fig. 4.12 on the right side. The fit for the first band produced large error margins and is for this reason not suitable to be analysed. As mentioned previously, our fit procedure is based on the assumption that the two resonances do not interact. We therefore suggest, that the inaccurate fit is a result of the interaction between the two resonant modes observed. In the second band the coupling parameter *q* is positive for large incident angle and becomes negative for angles smaller than $\Theta = 60°$ (corresponding to $k_{//} = 0.505$). For the fourth resonant band we see that for small incident angle a positive coupling parameter is observed (around +1) and for incident angles larger than $\Theta = 65°$ (corresponding to $k_{//} = 0.582$) a negative value for *q* is found.

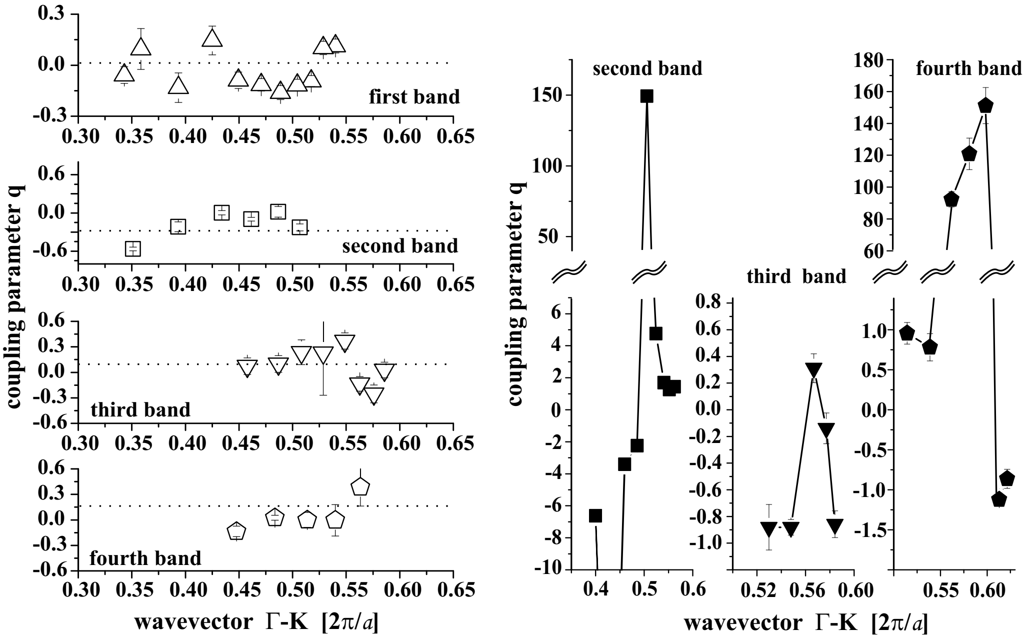

Figure 4.12: The coupling parameter for the different bands is shown. For the measurements obtained with TE polarised light, the values of q are around zero for all four bands, as can be seen in the left graphs. For the measurements obtained with TM polarised light, we observe a change of the coupling parameter.

The line shape of the resonances is associated to interference of light, that propagates along two different pathways. As a result, the q-reversal observed has to be sought in the nature of the interference. The square value of the coupling parameter q is defined as a ratio of transition probability (Eq. 4.2).

However, q also has a sign that reflects how the phase difference between the two pathways changes as the resonance frequency ω_0 is traversed. Here, the two pathways that can be identified are reflected via the discrete resonant modes (ϕ) and a direct reflection where in principle a continuum of states (Ψ_E) is available. The observed q - reversal via a large q value therefore indicates an overall phase shift of π between the two pathways. The large q values observed for certain wavevectors indicates that for those wavevectors the matrix element $\langle \Psi_E \,|\, T \,|\, \psi \rangle$ becomes small. Here, we suggest an explanation for the q - reversal based on the transission probability alone. Hereto we postulate that the photonic crystal slab actually has a Brewster angle

$$\Theta_{Brewster} = \arctan(\frac{n_{eff}}{n_{air}}) \ , \tag{4.5}$$

determined by an effective refractive index n_{eff}. With the effective refractive index $n_{eff} = 1.83$, calculated in section 1.2.2 of the two-dimensional photonic crystal slab, we find a Brewster angle at $\Theta_{Brewster} = 61.2\,^{\circ}$.

By traversing the Brewster angle, the phase of the reflected TM polarised light changes by π. At the Brewster angle, the reflection of TM polarised light is zero. For TE polarised light, the phase remains the same for all angles of incidence. The value of 61.2° agrees reasonably well with the angle for which the high q's are found. Above and below this angle, the phase of $\langle \Psi_E \,|\, T \,|\, \psi \rangle$ changes by π. In this explanation for the q-reversal we have assumed that the phase in the interference path via the resonant mode stays constant. Although the experimental accuracy is insufficient for real proof, the constant quality factors Q as a function of wavevector suggests a constant confinement time in the discrete mode.

Note that, in the field of molecule physics, e.g., autoionisation and molecular predissociation, q-reversal has also been observed [87]. In the photonic case, q-reversal in the form as shown here, where a discrete transition region is present, has not been reported before.

4.3 Conclusions

Far-field investigations have been performed on large photonic crystal slabs that is suspended in air. In-plane reflectivity measurements reveal a large TE stopgap along the crystalline Γ - K direction. For the odd modes (TM polarised light), also a stopgap is found. The measurements are in good agreement with the simulations. This suggests that the photonic crystal slab will also have the photonic bandgap for even modes, as predicted by the simulations.

The coupling of incident light to resonant modes of the crystal was observed in specular reflectivity measurements. From the resonance frequency, part of the dispersion relation directly is reconstructed and found to be in excellent agreement with simulations. Moreover, polarisation mixing between even and odd modes is observed in the spectra obtained along the crystalline Γ - K direction.

The line shapes of the resonance features is analysed in detail. For the fit, we adopted a function analogue to the one proposed in 1961 for resonances occurring in the energy spectra of electrons. From the line shape fit we obtain next to the resonance frequency two additional parameters, the line width γ of the resonance and the coupling parameter q. We find that the line width of the observed resonances are extremely narrow corresponding to high quality factors of the resonant modes. Two possible effects allow these observations. Firstly, our structures are symmetric and show a high confinement of the guided modes to the slab. Secondly, the angular resolution of our measurement setup is high, which avoids averaging of spectra obtained over an small angular range.

We observe a so-called q-reversal of the coupling parameter q for several modes. We suggest a the existence of a Brewster angle of the photonic crystal slab based on its effective medium index of refraction. This angle determines at which wavevectors the q-reversal occurs.

By combining in-plane and angle-dependent reflectivity measurements, a large fraction of the dispersion relation of the photonic crystal slab is probed. In this way, a solid understanding of the optical properties of the crystal is provided.

We have also performed near-field measurements on the two-dimensional photonic crystal slabs. However, the $100\,\mu$m wide membrane turned out to vibrate such that no reproducible results were achieved. Currently, PSTM investigations on similar membranes of $20\,\mu$m and $50\,\mu$m width are in progress. Moreover, first results on slightly different two-dimensional photonic crystals [91] were achieved. There, we visualised the coupling of light in coupled cavities in a two-dimensional photonic crystal. The preliminary results reveal the local coupling efficiency for frequencies at cavity resonance and of resonance. Such PSTM measurements allow, e.g., visualising the mode distribution of a cavity mode. Moreover, with our PSTM we can visualise propagating light pulses provided by a femtosecond laser [92]. Such investigations will reveal the local effect of the crystal on the different spectral components of light.

Chapter 5

Near-field optical transfer through 3D photonic crystals

Using a near-field microscope in illumination mode, light is coupled to a three-dimensional photonic crystal. The light transfer from the near-field source to the crystal and subsequent propagation is measured as a function of position and optical frequency. We investigate thick polystyrene opals with many different sphere sizes. Performing approach experiments allows the contribution of far-field and near-field components to be distinguished. In addition, we observe that defects in the <111> crystalline surface affect the coupling of light.

5.1 Introduction

Photonic crystals are rarely considered as the complex optical structures they are; their complete description should take into account not only far-field but also near-field properties [93]. So far, two main approaches have been utilised to probe the optical properties of photonic crystals. The first and by far the most extensively used has been transmission or reflection experiments in which both source and detector are in the far-field, see e.g., [8], [94]. These far-field methods have been successfully used to determine stopgaps or the mean free paths, and to elucidate the propagation of ultrafast pulses. Secondly, far-field measurements of spontaneous emission rates of sources embedded inside the crystals probe the so-called local density of states (LDOS) [5], [6]. The LDOS contains both far- and near-field components, and gives rise to modified quantum electrodynamics including inhibited or enhanced emission [95], [96]. In both approaches, the optical properties are spatially averaged by virtue of the detector being in the far-field. Even if focussed beams are used [97], [98] diffraction still limits the obtainable spatial resolution.

We present a new method to probe the near-field properties of three-dimensional photonic crystals. We investigate artificial opals of five different sphere sizes: $\mathrm{r} = 120\,\mathrm{nm}$, $\mathrm{r} = 129\,\mathrm{nm}$, $\mathrm{r} = 180\,\mathrm{nm}$, $\mathrm{r} = 213\,\mathrm{nm}$ and $\mathrm{r} = 241\,\mathrm{nm}$ (see section 1.2.3) with a NSOM in illumination mode. The sub-wavelength light source near the surface of the crystal launches light into the crystal. By scanning the position of the light source relative to the crystal surface, we measure the amount of light that reaches the other side of the crystal as a function of the launch position. With a resolution superior to the above mentioned techniques, we observe spatial variations in the amount of light launched into the crystals on length scales smaller than a unit cell.

5.2 Far-field reflectivity on opals

Using far-field reflectivity measurement (section 2.2.1), the exact location of the Γ - L stopgaps are determined, e.g., the stopgaps along the crystalline direction perpendicular to the <111> surface. Figure 5.1 shows a reflectivity spectrum for the opal with spheres of $\mathrm{r} = 241\,\mathrm{nm}$. The detected wavelength range is given in the corresponding dimensionless frequency, where a is the fcc lattice parameter and the frequency is given by $\omega = a/\lambda_0$. Since the material properties and the volume fraction are the same for crystals of different sphere sizes, the optical characteristics of the crystals, i.e., the stopgap positions, are related through a simple scaling behaviour. As a result, the reflectivity spectrum depicted in Fig. 5.1 is representative for the crystals of different sphere sizes used in this chapter.

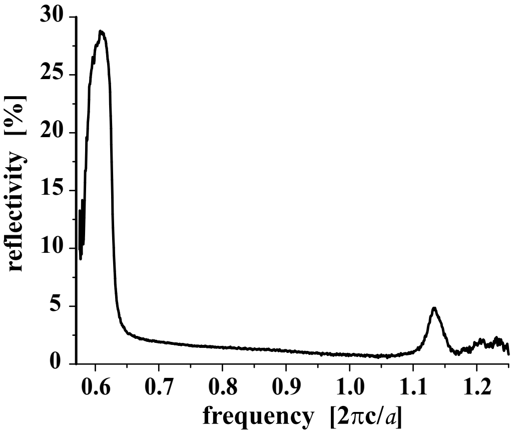

Figure 5.1: Reflectivity measurement on the r = 241 nm polystyrene opal. The dimensionless frequency (x-axis) is given by $\omega = a/\lambda_0$, where the cubic lattice parameter is $a = \sqrt{8} \cdot \mathrm{r}$. The first order Bragg diffraction is centred at $\omega = 0.61$. A second order Bragg diffraction peak is found at $\omega = 1.13$.

A strong first order Bragg diffraction is found at $\omega = 0.61 \pm 0.02$. The full width at half maximum (FWHM) of this reflection peak ranges from 0.58 to 0.63, which corresponds to a 8 % wide stopgap. A second reflectivity peak is found at $\omega = 1.13 \pm 0.02$. This peak ranges from 1.12 to 1.15 at the FWHM. In section 1.1.3, a first order Γ - L stopgap ranging from 0.58 to 0.62 was found in the calculations. This is in perfect agreement with our experiments. In addition, the range of second order Bragg diffraction along the Γ - L direction was determined from 1.13 to 1.24. As a result, the observed reflection peak around $\omega = 1.13$ is at the low frequency edge of a possible second order stopgap region.

Spectra have been measured for the different sphere size crystals. The obtained spectra are qualitatively similar to Fig. 5.1. We determined the centre wavelength of the first and second order Bragg diffraction and plot them as a function of sphere radius. Figure 5.2 shows the linear relation between sphere sizes and centre gap wavelength. For larger sphere radius r the L-gap shifts to longer wavelength. To determine the effective refractive index of the crystals, a linear fit was performed for the first and for the second order Bragg diffraction peaks as follows. The Bragg condition along the <111> crystalline direction (Γ - L direction) of a face centred cubic lattice is equal to

$$m \cdot \lambda_0^m = \frac{2}{\sqrt{3}} \cdot n_{eff} \cdot a = s_m \cdot \mathrm{r} \ , \tag{5.1}$$

where $a = \sqrt{8} \cdot \mathrm{r}$ is the cubic lattice parameter, λ_0^m the centre wavelength (in air)

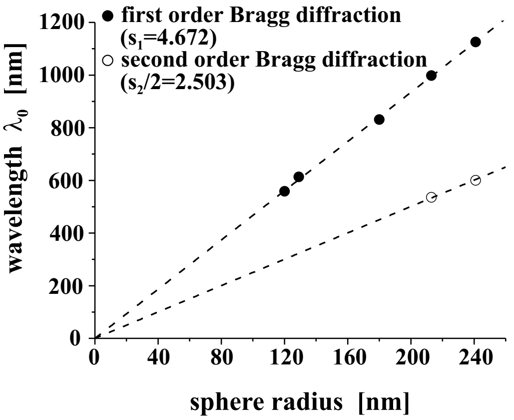

Figure 5.2: Wavelength of Bragg diffraction λ_0^m versus sphere radius r. The effective index can be determined from the slope. The second order Bragg diffraction shows, that the effective index is not twice of the first order Bragg diffraction.

of the stopgap and m an integer value corresponding to the order of the diffraction peak. We find a slope $\mathrm{s}_1 = 4.672 \pm 0.018$ for the first order Bragg diffraction and $\mathrm{s}_2/2 = 2.503 \pm 0.012$ for the second order Bragg diffraction. From the fit through the measured first order stopgap an effective index of refraction $\mathrm{n}_{eff} = 1.43 \pm 0.03$ is calculated. This shows that Eq. 1.2 provides a good approximation to calculate the effective refractive index ($\mathrm{n}_{eff} = 1.46 \pm 0.07$). However, the fit through the second order Bragg diffraction peak results in an effective refractive index of $\mathrm{n}_{eff} = 1.53 \pm 0.03$. In other words, the second order diffraction does not correspond to the order $m = 2$, but rather to $m = 1.87$, assuming the effective refractive index is $\mathrm{n}_{eff} = 1.43$. Such a discrepancy has been observed earlier for titania inverse opals, and has been attributed to complex multiple Bragg diffraction coupling [99]. The reflectivity measurement provide an accurate determination of the effective refractive index of the opals and of the first order Γ - L stopgap.

5.3 Position-dependent light transfer

Using the NSOM in illumination mode (section 2.1.3), we investigate the transfer of light coming from the point-like light source through the crystal. The position-dependent intensity data obtained in this way are the combined result of

1. the launching of the light from the fibre tip into the crystal,

2. the propagation of light through the crystal, and

3. the exiting of the light from the crystal to the large detector.

It has been found that the mean free path of light diffusion in similar crystals is about 15 μm [100]. Since this length is much less than the sample thicknesses of $\sim 200\,\mu$m, we conclude that the propagation and exiting (points 2 and 3) are randomised and are thus independent of the tip position. Therefore, the detailed position-dependence that will be discussed in the following is caused by the launching of the light from the tip to the crystal (point 1).

The crystals are mounted on a 0.17 mm thick glass plate, which is positioned on a photodiode. Light coming from the rear of the crystal passes the glass plate and an air gap of several hundred microns between the glass plate and the detector. The detector in this setup is effectively positioned in the far-field. For the near-field measurements, the evanescent field of the probe is assumed to be constant for different frequencies. In the experiment, light of an Ar / Kr laser is sent through a $\lambda/4$ and $\lambda/2$ plate before it is coupled via an 0.32 NA (16 ×) objective into the fibre with the near-field probe. The two waveplates are used to pre-polarise the light in order to obtain circularly polarised light coming out of the near-field probe. It has been established that the observed near-field patterns are independent of experimental conditions like the near-field probe geometry and the height feedback. The crystals are mounted such, that they present their <111> surface to the near-field probe.

5.3.1 Frequency-dependent light transfer on big sphere crystals

Crystals consisting of big spheres turned out to be more robust for scanning purposes. For this reason, we start our investigations on large sphere size crystals and perform the initial check of three-dimensional measurements, to determine the reliability of the near-field pattern. The crystal consisted of polystyrene spheres of $r = 241 \pm 5$ nm. The optical frequencies used are $\omega = 1.33$, 1.20 and 1.05, corresponding to the laser wavelength $\lambda_0 = 514$ nm, 568 nm and 647 nm, respectively. The near-field transfer is measured as a function of the relative position of the sub-wavelength light source with respect to the unit cell of the crystal.

As a first step optical measurements are carried out at different (x,y)-planes of constant heights above the surface (see three-dimensional measurement mode, section 2.1.4). Figure 5.3 a shows the topographical information simultaneously obtained with the measured transfer of light of $\lambda_0 = 647$ nm (Fig. 5.3 b) in shear force feedback measurement ($z \sim 10 \pm 5$ nm). In the topographical image corrugations of up to 85 nm are obtained. The high topographical resolution is a result of a small Al grain located at the end face of the fibre probe. The grainy structure of the tip can be seen in the observed tip convolution in Fig. 5.3 a. The detected optical signals for three different tip heights above the crystal are presented in Fig. 5.3 c for z = 84 ± 30 nm, in Fig. 5.3 d for z = 446 ± 30 nm and in Fig. 5.3 e for z = 723 ± 16 nm. In all four optical measurements, a hexagonal pattern of bright intense spots is clearly observed and remains visible even for large tip to sample separation. This persistence of the optical pattern shows that the near-field pattern in shear-force contact (Fig. 5.3 b) is not influenced by the height feedback. We therefore exclude topographical artifacts [57]. The periodicity of the optical pattern corresponds to the arrangement of the polystyrene spheres, which is 2 r = 482 nm. Thus, in all images optical information is obtained on a scale that is beyond the diffraction limit.

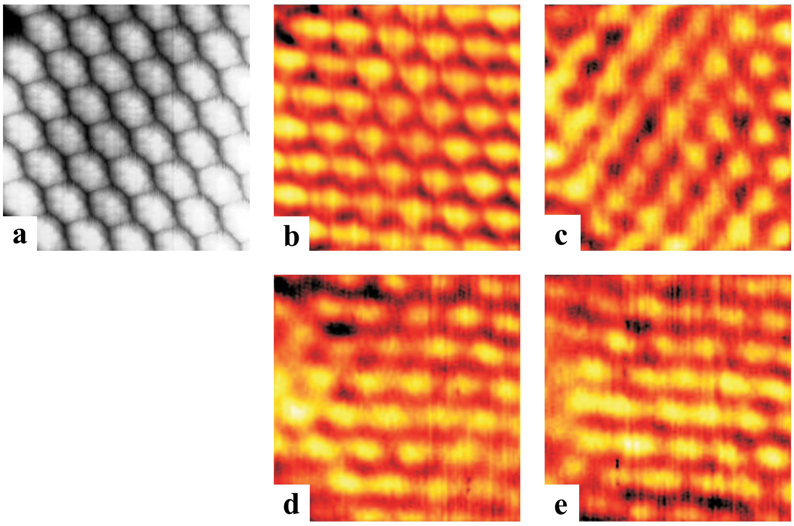

Figure 5.3: Near-field measurements performed for different tip to sample separations. a) Topographical image, the hexagonal arrangement of the polystyrene spheres in the <111> surface of the crystal is visible. The apparent shape of the spheres is dominated by tip convolution effects. b) Detected intensity as a function of x-y position, obtained simultaneously with image a) at z ∼ 10 nm. c), d) and e): Detected spatial intensity at planes parallel to the <111> surface at z = 84 nm, z = 446 nm and z = 723 nm, respectively. The optical patterns show local information of the light transfer with sub-wavelength resolution and the pattern persists for different tip to sample separations. Image sizes: 2.71 μm × 3.02 μm.

A quantitative analysis of the measurements in Fig. 5.3 reveals that the optical modulation M (see Eq. 3.1) decreases as a function of tip to sample separation from 7 % at a height of z ∼ 10 nm to 4 % at z ∼ 723 nm. Furthermore, the average intensity of transmitted light through the crystals drops by 13 % with increasing tip to sample separation from $z \sim 10\,\mathrm{nm}$ to $z = 723\,\mathrm{nm}$. We conclude that more light is launched into the crystal when the tip is in the near-field regime than when it is in the far-field regime. We recall, that a near-field probe provides both real and imaginary wavevectors over an angular range of 2π solid angle (section 2.1.1). The increase in throughput indicates that wavevectors within the forbidden angles are coupled to the crystal, when the probe is in the near-field regime.

As a next step, we investigate the different frequencies near the second order L-gap region. Figure 5.4 a shows the topography of the polystyrene crystal obtained simultaneously with the optical information shown in Fig. 5.4 d. The topographical information obtained simultaneously with the other optical measurements is identical to Fig. 5.4 a and for this reason not shown. The near-field patterns shown in Figs. 5.4 b, 5.4 c and 5.4 d are obtained at $\omega = 1.05$, 1.20 and 1.33, respectively. In all three measurements the hexagonal structure of the sphere arrangement with period $2\,r = 482\,\mathrm{nm}$ is clearly present. For all three different measurements more light is detected when the tip is positioned on top of a sphere. Less light is detected when the fibre probe is in between the spheres. While the images contain all the information about launching light into the crystal, the propagation of this light through and its exit from the crystal, the detailed features can be attributed to the near-field launching into the crystal.

The measured near-field patterns change as the wavelength is varied. To elucidate the changes in more detail, we summed up all unit cells found in the measurement in Figs. 5.4 b, 5.4 c and 5.4 d and reconstructed an average unit cell for each of the three measurements. Figures 5.4 e-h shows the area around one sphere as obtained from the average unit cell. Figure 5.4 e shows the topography around one sphere. Figures 5.4 f, 5.4 g and 5.4 h show the corresponding optical fields for the three different frequencies. It is clearly seen that the position of the bright spot shifts from the centre of a sphere at $\omega = 1.05$ to one edge of the sphere at $\omega = 1.33$. It is remarkable that the three-fold symmetry around the $<111>$ crystalline direction is broken in Fig. 5.4 g and 5.4 h.

To investigate the shift of the bright intensity spots, we have performed cross correlations between the different optical patterns of Figs. 5.4 b, 5.4 c and 5.4 d. As a result, the shift of the bright spots can be determined for the different crystalline directions. In table 5.3.1, the shifts observed along the crystalline $<\bar{1}10>$ and $<\bar{1}01>$ directions are given. We observe, that the shift between $\omega = 1.05$ and $\omega = 1.33$ along the $< \bar{1}10 >$ direction is larger than the shift observed between $\omega = 1.05$ and $\omega = 1.20$ along the same crystalline axis. Along the $<\bar{1}01>$ direction the shifts observed for the two frequencies $\omega = 1.20$ and $\omega = 1.33$ with respect to $\omega = 1.05$ are comparable.

As can be seen in Figs. 5.4 f, 5.4 g and 5.4 h, not only the position of the bright

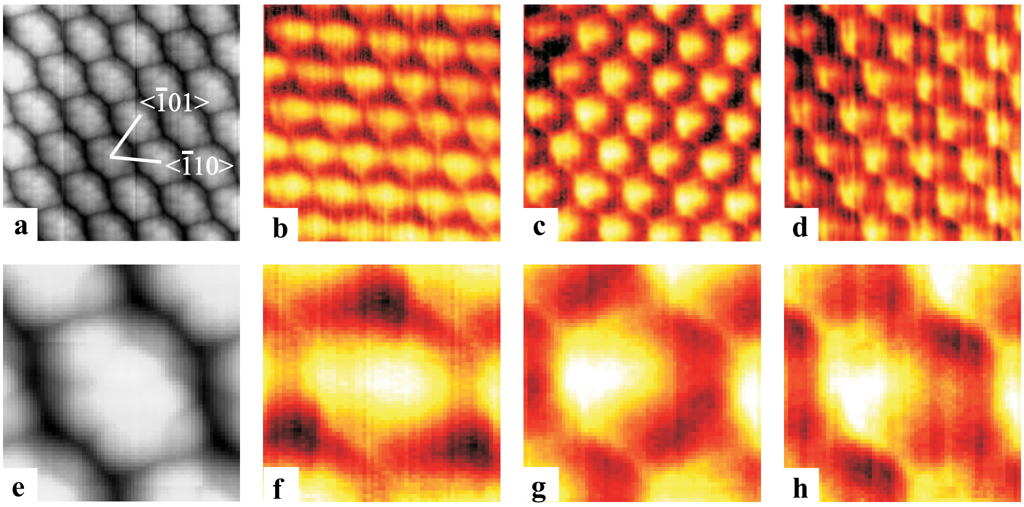

Figure 5.4: Position-dependent (x-y plane) transfer of light form tip to three-dimensional photonic crystal obtained for different wavelength of light. a) Topographical information of the <111> crystalline surface of the polystyrene crystal. b), c) and d): Near-field optical patterns at $\omega = 1.05$, 1.20 and 1.33, respectively. Image sizes: 2.28 μm × 2.53 μm. Images e), f), g) and h) show the topography and the optical signals of a close up area around one polystyrene sphere in more detail. The images are built up from an average unit cell to pronounce the details of the original measurements. Image sizes: 0.65 μm × 0.72 μm.

spots shift, but also their shape changes as a function of frequency. Figure 5.5 depicts a line trace taken along the <$\bar{1}$10> direction and through the centre of the sphere from the rebuilt areas of Figs. 5.4 f, 5.4 g and 5.4 h. The size of the bright intensity spots becomes smaller for shorter wavelengths. We measure the width w of the bright spot to be w = 360 ± 20 nm at $\omega = 1.05$, whereas the width of the spots at $\omega = 1.20$ and $\omega = 1.33$ is w = 270 ± 20 nm.

crystalline direction	$\omega = 1.05$ to $\omega = 1.33$ Δ [nm]	$\omega = 1.05$ to $\omega = 1.20$ Δ [nm]
$< \bar{1}10 >$	82 ± 6	72 ± 6
$< \bar{1}01 >$	24 ± 9	23 ± 9

Table 5.1: Shifts of the bright intense spots along two different crystalline directions, when the frequency is changed from $\omega = 1.05$ to $\omega = 1.33$, middle column, and when the frequency is changed from $\omega = 1.05$ to $\omega = 1.20$, right column.

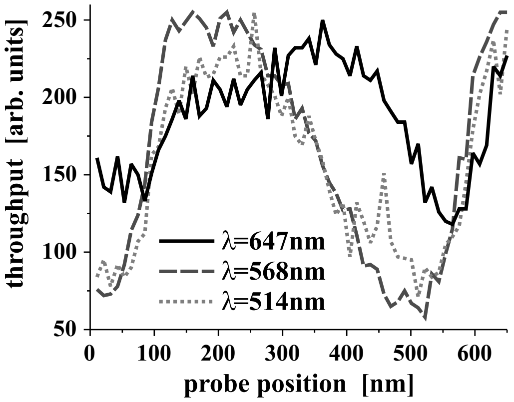

Figure 5.5: Line traces along the crystalline $<\bar{1}10>$ direction from Figs. 5.4 f, 5.4 g and 5.4 h. The shape of the optical pattern changes as a function of frequency. This is elucidated by determining the width w of the bright spots, which is $\mathrm{w} = 360 \pm 20$ nm at $\omega = 1.05$ and $\mathrm{w} = 270 \pm 20$ nm at $\omega = 1.20$ and at $\omega = 1.33$ for the $<\bar{1}10>$ crystalline direction.

To interpret the different optical patterns shown in Fig. 5.4, we recall that a second order stopgap region is present from $\omega = 1.13$ to 1.24. The three frequencies measured are situated near this region. The frequency $\omega = 1.05$ is situated below the second order stopgap. Therefore, light is launched into propagating modes that have the same symmetry as the crystal, by virtue of Bloch's theorem [21], [20]. The frequencies $\omega = 1.20$ and 1.33 are both situated inside the second order stopgap region. For frequencies in a stopgap, the light is not launched into propagating Bloch modes, but in evanescent modes that do not match the crystal symmetry. As a result, the intensity distribution does not have the symmetry of the underlying crystals and the distribution shifts through the unit cell. This tentative explanation is based on reasoning from dynamical diffraction theory for X-rays [101].

5.3.2 Near-field transfer on crystals of different sphere sizes

In this section we study the position-dependent near-field transfer on crystals of different sphere sizes. By using the laser wavelengths $\lambda_0 = 514$ nm, 530 nm, 568 nm and 647 nm, a range of frequencies from 0.52 to 1.33 of the band diagram is probed. We will discuss the results in the order of the sphere size of the opals by going from large to small. In the previous section, investigations on the big sphere crystal ($\mathrm{r} = 241$ nm) have already been presented.

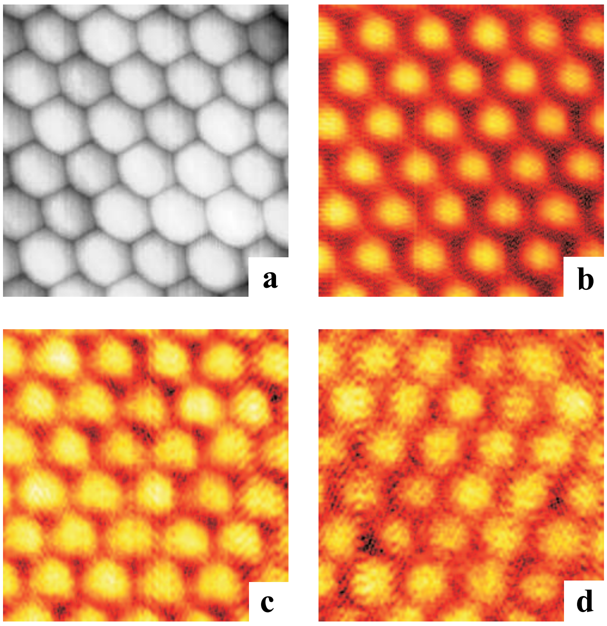

Figure 5.6: Position-dependent near-field transfer on a polystyrene opal with sphere radius r = 213 nm. a) Topographical information simultaneously obtained with the optical image at $\omega = 1.14$ depict in image d). Image b) and c) depict the optical information obtained at $\omega = 0.93$ and at $\omega = 1.06$, respectively. For all three frequencies, most light is coupled through the crystal, when the fibre probe is positioned on top of a sphere. Image sizes: 2.11 μm × 2.40 μm.

Figure 5.6 shows the position-dependent near-field transfer obtained on an opal with r = 213 nm. The measurements are performed at $\omega = 0.931$ (Fig. 5.6 b), $\omega = 1.06$ (Fig. 5.6 c) and $\omega = 1.14$ (Fig. 5.6 d), respectively. The topographical information shown in Fig. 5.6 a is obtained simultaneously with Fig. 5.6 d and shows a hexagonal pattern of smooth spheres. Clearly, the hexagonal arrangement of the spheres is recognised in the optical images (Figs. 5.6 b - d). It can be seen that the bright intensity spots are located on top of the spheres at all frequencies, similar to Fig. 5.4 b. This observation agrees with our hypothesis, since the frequencies correspond to propagating Bloch states with the symmetry of the crystal. For the frequency $\omega = 1.14$ situated at the low frequency edge of the region of second order stopgaps, no obvious changes amongst the optical pattern is found in Fig. 5.6 d. The absence of a detectable shift is very likely, because this frequency is barely in the stopgap region. Moreover, in an r = 213 nm crystal a shift should be proportionally smaller than in a r = 241 nm crystal, thereby further reducing the likelihood to observe a pattern shift.

Similar measurements are obtained on the r = 180 nm sphere crystal at frequencies $\omega = 0.79$, $\omega = 0.90$ and $\omega = 0.99$. The near-field patterns observed resemble those shown in Fig. 5.6, as our hypothesis predicts, since the frequencies correspond to propagating Bloch states with the symmetry of the crystal.

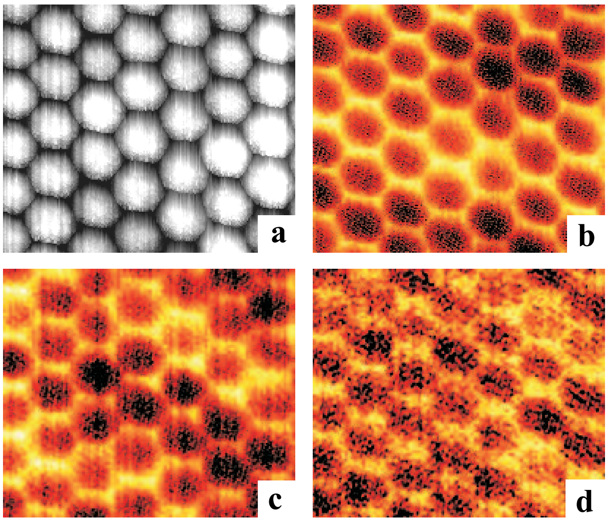

Figure 5.7: Position-dependent near-field transfer on a polystyrene opal with sphere radius r = 129 nm. a) Topographical information simultaneously obtained with the optical image at $\omega = 0.56$ depict in b). c) and d) show the optical information obtained at $\omega = 0.64$ and at $\omega = 0.71$, respectively. Most light is coupled through the crystal, when the fibre probe is positioned in between the spheres. Image sizes: 1.41 μm × 1.33 μm.

With decreasing frequencies, we approach the first order Γ - L stopgap that is centred at $\omega = 0.60$, as determined from the reflectivity measurements. Figure 5.7 shows the position -dependent near-field transfer on the r = 129 nm opal. Fig. 5.7 a depicts the topographical information obtained simultaneously with the optical measurement at $\omega = 0.56$ shown in Fig. 5.7 b. Figure 5.7 c and 5.7 d are obtained for $\omega = 0.64$ and $\omega = 0.71$, respectively. A completely different optical field distribution is encountered in these images compared to Fig. 5.6. Clearly, more light is transmitted through the crystal when the fibre probe is positioned between spheres. For the measurements on the r = 120 nm opal, the optical near-field transfer pattern looks qualitatively similar to that obtained on the r = 129 nm opal. The probed frequencies on the two small sphere size crystals are located around the first order Γ - L stopgap. Our hypothesis based on dynamical X-ray diffraction theory would predict an inversion of the near-field pattern at frequencies below compared to frequencies above a stopgap. The absence of such an inversion at the first order Γ - L stopgap can be rationalised as follows: a near-field probe launches light under the forbidden angles into the material. As a result, the fraction of wavevectors k, which the tip launches in the Γ - L direction, can be relatively small. We suggest that the available ratio between k vectors in the forbidden angles and k-vectors in the allowed angles is in our experiment such, that the sensitivity becomes small for the Γ - L direction and thus influences of the first order stopgap are not detected.

We find an inversion of the optical contrast in the near-field transfer patterns between $\omega = 0.71$ and $\omega = 0.79$, that is, more light enters between the spheres for $\omega < 0.71$, while more light enters on the spheres for $\omega > 0.79$. A tentative explanation for the inversion of the intensity distribution is that in this frequency range (0.7 - 0.79) many stopgaps are simultaneously present, i.e., at the U, K, and W at the sixfold rim of the Brillouin zone (Fig. 1.5). Since a large fraction of the modes launched by the tip are likely in these wavevectors (forbidden angles), our experiment is sensitive to stopgaps in these k-points. Below and above the stopgaps, the intensity distribution of Bloch modes has shifted from one spatial distribution to its complement [102]. Such a shift of the intensity distribution is exactly what we observe.

Note that in Fig. 5.7 contrast variations within the measurement area are observed between different unit cells. Especially in the Fig. 5.7 b and 5.7 c brighter and darker areas within the scan window are clearly visible. In the corresponding topographical image no displacement of the spheres (i.e., in the z-direction) is observed. We therefore attribute these variations to imperfections of the crystal in some of the underlying layers. Since the mean free path for light in these polystyrene opals is $\sim 15\,\mu$m [100], any changes in the first $15\,\mu$m of the crystal may influence the near-field transfer pattern directly. It is likely, however, that these pronounced effects originate in the first few monolayers. This notable finding shows that the NSOM is not only able to reveal local optical properties in two dimensions of the incouple interface (x-, y-direction), but NSOM also probes deeper underlying layers. In analogy, the scanning tunnelling microscopes (STM) have already proven, that defects below the perfect surface can be sensed (see e.g., [103], [104]).

5.3.3 Defects in the crystalline <111> surface

All measurements shown in the previous sections (5.3.1 and 5.3.2) have been performed on perfect <111> surfaces. Such surfaces may contain various types of defects, like edges of crystalline domains or missing spheres. In this section the effect of a single surface defect, e.g., a polystyrene sphere missing in the <111> surface, is investigated on the optical coupling.

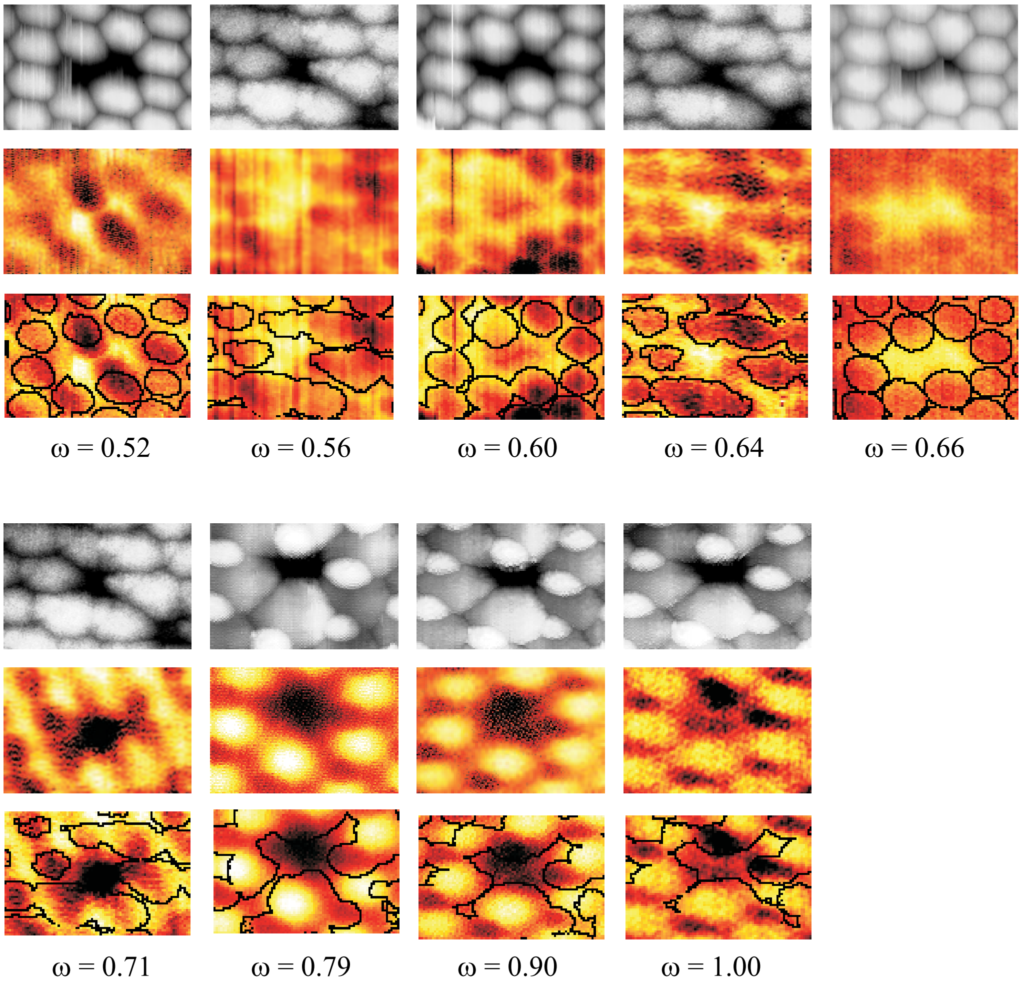

$\omega = 0.52$ $\omega = 0.56$ $\omega = 0.60$ $\omega = 0.64$ $\omega = 0.66$

$\omega = 0.71$ $\omega = 0.79$ $\omega = 0.90$ $\omega = 1.00$

Figure 5.8: Position- light transfer on a crystal area containing a defect for different normalised frequencies. For every frequency the measured topography (top), the optical signal (middle) and the optical signal with a superimposed topographical contour map (bottom) are given. The transmission and coupling of light from the near-field probe positioned on top of the defect is strongly frequency-dependent. For a frequency located at the stopgap ($\omega = 0.61$), less light is transmitted at the defect. For frequencies $\omega \leqslant 0.66$, bright spots at the locations of the defects are clearly observed in the optical image. For frequencies $\omega \geqslant 0.71$, less light is coupled at the defect locations.

Figure 5.8 shows measurements on polystyrene crystal <111> surfaces containing different defects. The measurements are arranged according to the dimensionless frequency ω at which they were measured. Three images are presented for each frequency ω. The images on top show the topographical information measured simultaneously with the optical image shown in the middle. The images on the bottom present a combination of the two upper ones. There, the topographical information is given by a contour plot and is superimposed on the optical information. In this way, the effect of the surface defect to the light transfer is more easily recognised.

The observations on local coupling via defects is discussed starting with the optical behaviour for small frequencies. At $\omega = 0.52$ light was coupled via a "dimer-defect". We observe that for a tip position on the defect more light is transferred. Even though the optical contrast is not excellent, a similar effect is observed at $\omega = 0.56$. In this case a single missing sphere forms the defect. The frequency $\omega = 0.60$ is located in the first order Γ - L stopgap. For this frequency less light is transmitted via the "dimer defect". For a frequency slightly above the stopgap, $\omega = 0.64$, we again find an increase in intensity at the location of the defect. At $\omega = 0.66$, the high transmission is very pronounced. For light at $\omega = 0.71$, less light is coupled to the photonic crystal via the defect. For higher frequencies ($\omega = 0.79$, $\omega = 0.90$ and $\omega = 1.00$), also less light is observed for a tip position on top of the defect.

In summary, we find that the transmission through a defect depends strongly on the frequency. We find a low transmission through a defect at the first order Γ - L stopgap frequency. For frequencies $\omega \leqslant 0.66$, except frequencies in the stopgap, we find a high throughput at the defect. For frequencies $\omega \geqslant 0.71$, less light enters through defects. We note that the inversion of the optical near-field pattern on the perfect crystal areas occurs at a slightly higher but different frequencies ($0.71 < \omega < 0.79$), compared to the inversion in transmission through the defect ($0.66 < \omega < 0.71$).

5.4 Approach curves

Moving the near-field probe in and out of contact while measuring the throughput reveals additional information about the coupling of light from the tip in the near-field regime of the crystal. We use the three-dimensional measurement setup described in section 2.1.4. Instead of reconstructing different measurement planes parallel or perpendicular to the sample, we will study the obtained approach curves directly.

5.4.1 Frequency-dependent approach curves on opals

We have performed approach measurements at different frequencies, using the wavelengths $\lambda_0 = 568\,\text{nm}$ and $647\,\text{nm}$ and different sphere size opals. In principle, an approach curve can be measured at different positions in the unit cell of the <111> surface. Here, only approach curves obtained on top of the spheres are discussed, since they are qualitatively similar to those obtained at a tip position in between spheres.

Figure 5.9 shows the obtained approach curves for six different frequencies, to illustrate the important characteristics observed in all approach curves. The x-axis of the graphs give the tip to sample separation, whereas the y-axis depicts the throughput measured on the photodiode. Note, that this throughput is not normalised to the intensity throughput of the tip. For this reason, the amount of throughput in the different approach curves of Fig. 5.9 can not be compared directly. Generally, we find a higher throughput in the near-field regime compared to the throughput in the far-field regime. For different measurements, we observe an increased near-field transfer intensity of up to 25 % more than the far-field throughput. This decrease in signal with increasing probe to sample separation has already been described in section 5.3.1. In all approach curves periodic fringes are observed. These are Fabry-Perot fringes that occur in the air cavity between tip and opal and the periodicity is exactly $\lambda_0\,/\,2$. We find that the modulation of the fringes is largest at $\omega = 0.60$. We associate this observation to a high reflectivity of light, since the frequency used is situated in the Γ - L stopgap. Note that the approach curves keep their general characteristics for all frequencies, independent of whether the position-dependent near-field pattern showed a bright spot on top of the spheres or whether more light was transferred in between the spheres.

Before we investigate the approach curves in more detail, we make a brief excursion to approach curves on a homogeneous dielectric, i.e., a glass plate and we introduce an intuitive picture to understand the difference of the coupling of near-field components of light and the coupling of far-field components of light. The excursion should help to understand qualitatively the contributing mechanisms, which play a role in the approach curves obtained on the opals. Afterwards, we provide a complete analysis on the approach curves obtained on the opals.

5.4.2 Experiments on a glass plate

Approach curves have been measured on a simple glass plate of 0.17 mm thickness. The glass plate is mounted directly on the detector similar as in the measurements on the opals. Figure 5.10 depicts approach curves on the glass plate performed for $\lambda_0 = 647\,\text{nm}$, $568\,\text{nm}$ and $530\,\text{nm}$, respectively. We find Fabry-Perot fringes with a periodicity of $\lambda_0/2$ due to an air cavity between tip end face and glass plate. The

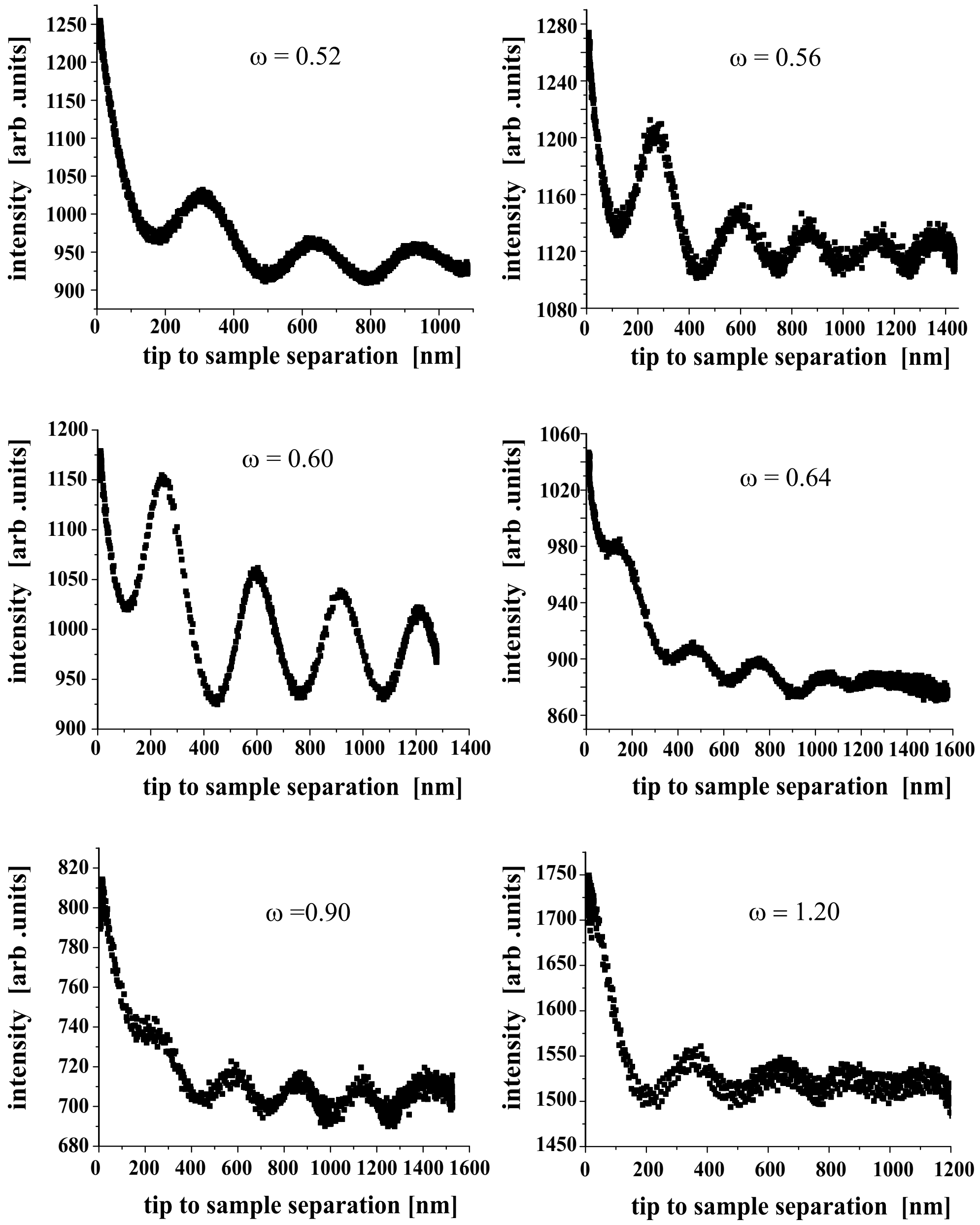

Figure 5.9: Approach curves measured at different optical frequencies. The general character of all approach curves shows an increase in throughput for a small tip to crystal separation. Furthermore, in all approach curves Fabry-Perot fringes are observed resulting from the air cavity between tip and opal. For the frequency situated in the first order Γ - L stopgap ($\omega = 0.60$), a larger modulation depth of the Fabry-Perot fringes is observed.

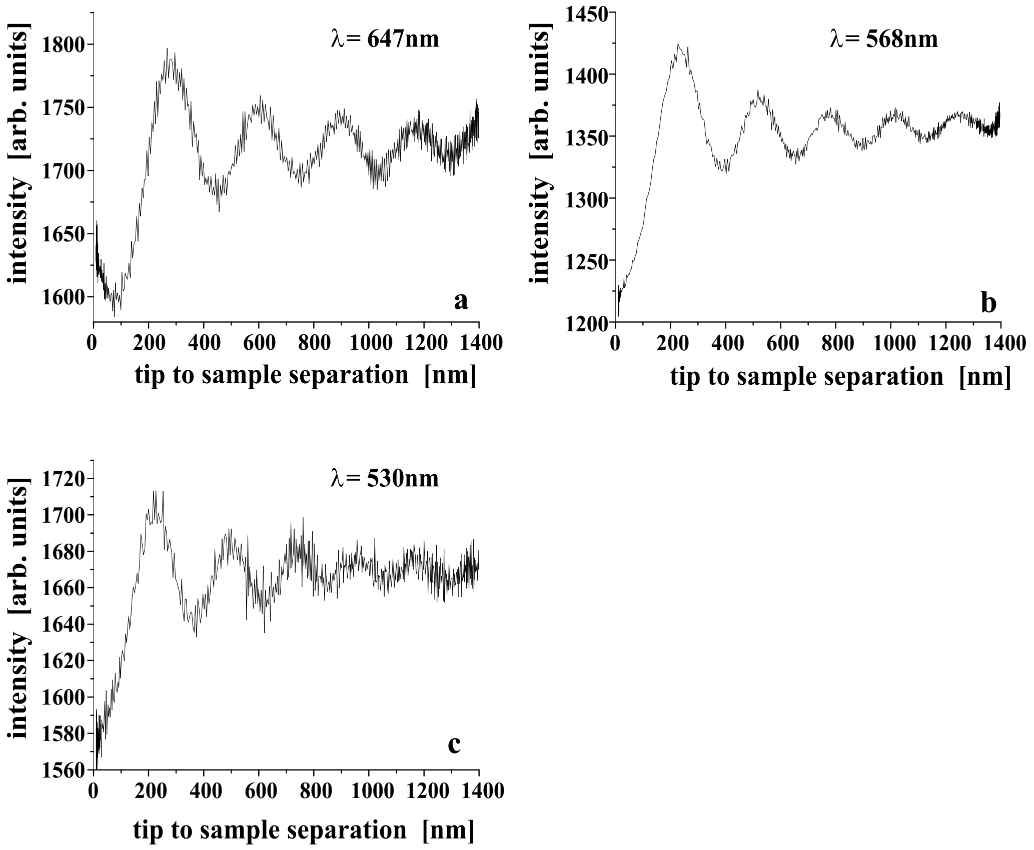

Figure 5.10: Approach curves on a glass plate for $\lambda_0 = 647\,\mathrm{nm}$, $\lambda_0 = 568\,\mathrm{nm}$ and $\lambda_0 = 530\,\mathrm{nm}$, respectively. In the near-field regime, a decrease in transmission compared to the far-field regime is observed. Furthermore, the modulation of the Fabry-Perot decreases for increasing tip to sample separation.

modulation of the fringes decreases clearly for increasing tip to sample separation. This effect is associated with planar geometry of the cavity. With increasing tip to sample separation light that propagates obliquely to the cavity axis escapes out of the cavity. In the near-field regime, less light is transmitted compared to when the tip is positioned in the far-field regime. In Fig. 5.10 a we find a small increase in intensity over the last tens of nanometers of the approach.

5.4.3 Intuitive model for approach curves

To interpret qualitatively the coupling of light under forbidden and allowed angles, we consider a simple model. The model is originally used to simulate fluorescence of single molecules [105]. Here, it is used to elucidate the principle of the coupling of near-field components of light. Figure 5.11 schematically shows the model used. A dipole is positioned inside a dielectric medium. The dipole is oriented at an angle, such that the emitted near-field and far-field components of light reach the detector. An air gap of height h is defined with $n_{air} = 1$. During an approach curve h is varied. The bottom dielectric medium corresponds to the sample, i.e., in our experiments either opal or glass plate. The detector is defined such that all the light coupled to the bottom dielectric is collected.

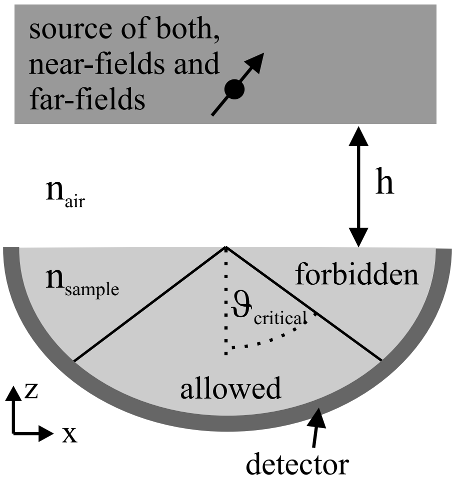

Figure 5.11: Schematic picture of the intuitive model. Near-field and far-field components of light are provided by a dipole located in the top dielectric. All the light that couples to the bottom dielectric reaches the detector. In an approach experiment, the height h of the air gap is varied.

Figure 5.12 shows the simulated approach curves on a glass plate, when the dipole emits light of $\lambda_0 = 647$ nm. Fig. 5.12 a depicts the intensity of transmitted light integrated over all the allowed angles $\vartheta_{allowed}$. Clearly, the Fabry-Perot fringes are produced by the air gap cavity. The modulation depth decreases with increasing thickness h of the air gap. As discussed earlier, the decrease in the modulation depth is associated to the leakage of the cavity, which allows the light to escape. Close to the glass surface, a drastic decrease in intensity is observed. This is similar to our observation on the glass plate. Figure 5.12 b gives the transmitted light in the forbidden angles larger than ϑ_c. Note that light can only be

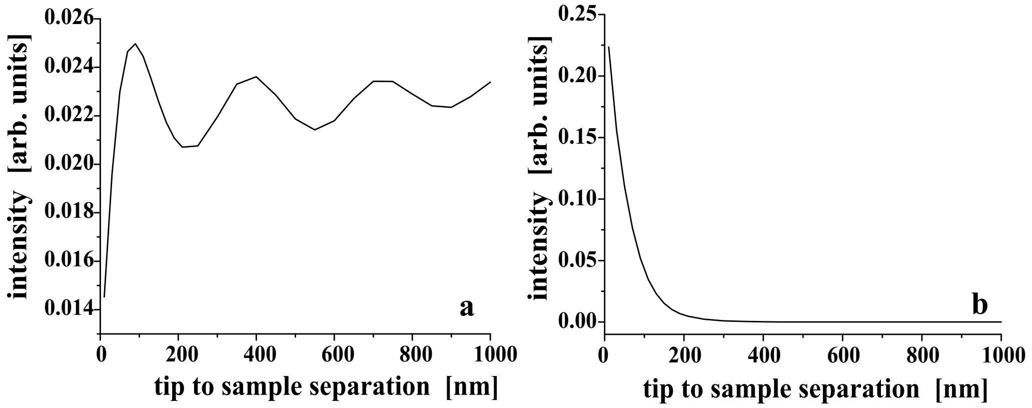

Figure 5.12: Calculated approach curves for the geometry of Fig. 5.11. a) depicts an approach curve when light is only detected in the allowed angles. b) shows an approach curve of light detected at forbidden angles.

coupled to these angles in the near-field regime (imaginary wavevectors). As a result, it is clear that the contribution decays exponentially with increasing tip to sample separation. Apparently, the total transmitted power in our experiments consists of the sum of light in the allowed angle and light in the forbidden angles. Such a sum shows the Fabry-Perot fringes as well as an increase in intensity in the near-field regime, due to the contributions from the forbidden angles resulting from evanescent field components. For samples that do not exhibit diffuse light propagation a NSOM can be designed to measure the approach curves for forbidden and allowed angles separately [40].

We conclude that the approach curves on a glass plate (Fig. 5.10) show only the light coupled to the glass plate at the allowed angles. Of course, light at forbidden angles is coupled into the glass as well. However, the light is trapped in the glass plate by total internal reflection and its contribution is not detected,because of our detection configuration. For $\lambda_0 = 647\,\mathrm{nm}$, a slight increase for smaller distances is observed that could indicate a small contribution of the evanescent fields.

For the approach curves on the opals shown in Fig. 5.9, we observed an increase in intensity in the near-field regime compared to the transmission observed in the far-field regime. This is an effect of the diffuse scattering of light in the opal. The mean free path of the opal is smaller than the sample thickness, whereas for a glass plate, the mean free path is much longer than the sample thickness. As a result, light that is coupled into the opals under a forbidden angle reaches the detector. Thus, much more light becomes available in the near-field regime and an increase in intensity is observed in the approach curves.

5.4.4 Discussion and interpretation

Based on the results gained from the intuitive model, we construct a function suitable to fit the the approach curves. We define

$$f(h) = A_{near} \cdot exp(\frac{-h}{t_{near}}) + A_{far} \cdot exp(\frac{-h}{t_{far}}) \cdot sin(\frac{\pi(h-\alpha)}{\lambda}) + f(\infty) \ , \quad (5.2)$$

where the first term represents the near-field decay with a decay length t_{near} and an amplitude A_{near}. The second term consists of a sine that produces the far-field characteristic with the Fabry-Perot fringes. The envelope of the fringe pattern decays with a decay rate t_{far}, A_{far} is the amplitude of the far-field term and α is the phase of the sine. Finally, $f(\infty)$ is the far-field transmission of light through the crystal. Since $f(\infty)$ is not normalised to the input power and the far-field throughput of the fibre probe no direct conclusions about the far-field transmission may be derived. For the relative comparison of the amplitudes obtained from fits of different approach curves at different frequencies, we will normalise the values to $f(\infty)$. Also for the determination of the absolute near-field transmission of light through the crystal (see section 5.5), we used $f(\infty)$ for normalisation.

The fitting procedure was performed on several approach curves at different frequencies as shown in Fig. 5.9. Figure 5.13 collects the resulting fit parameters as a function of frequency. For most frequencies different approach curves have been measured and fitted. Therefore, we show the average values of the parameters obtained.

Fig. 5.13 a depicts the phase α of the sine, that fits to the Fabry-Perot fringes. The gray regions indicate the first and second order Γ - L stopgaps. The phase becomes negative at frequencies in or slightly above the first order stopgap. For the other frequencies, the phase is more or less constant. It seems that the interference pattern in the approach curves is strongly influenced by the existence of the first order stopgap. The negative phase indicates that the phase jump that the light incurs when it is reflected at the crystal surface reverses its sign. It is reasonable that this property is affected by a Γ - L stopgap, since it is related to the cavity made of the tip and the crystal, whose cavity axis is parallel to Γ - L.

The normalised near-field amplitude $\mathrm{A}_{near}\,/\,\mathrm{f}(\infty)$ depicted in Fig. 5.13 b reveals no clear frequency dependence. For the near-field exponential decay t_{near} that is depicted in Fig 5.13 d, we find that the decay length decreases for increasing frequency. It is well-known, that the decay length decreases with decreasing wavelength (see Eq. 3.2). For the frequency slightly below the first band edge the decay length is found to be two times longer than in for the other frequencies.

The normalised far-field amplitude $\mathrm{A}_{far}\,/\,\mathrm{f}(\infty)$ is depicted in Fig. 5.13 c. We find in an increased normalised amplitude A_{far} for the frequency in the first order stopgap. This is consistent with an increased reflectivity due to Bragg diffraction

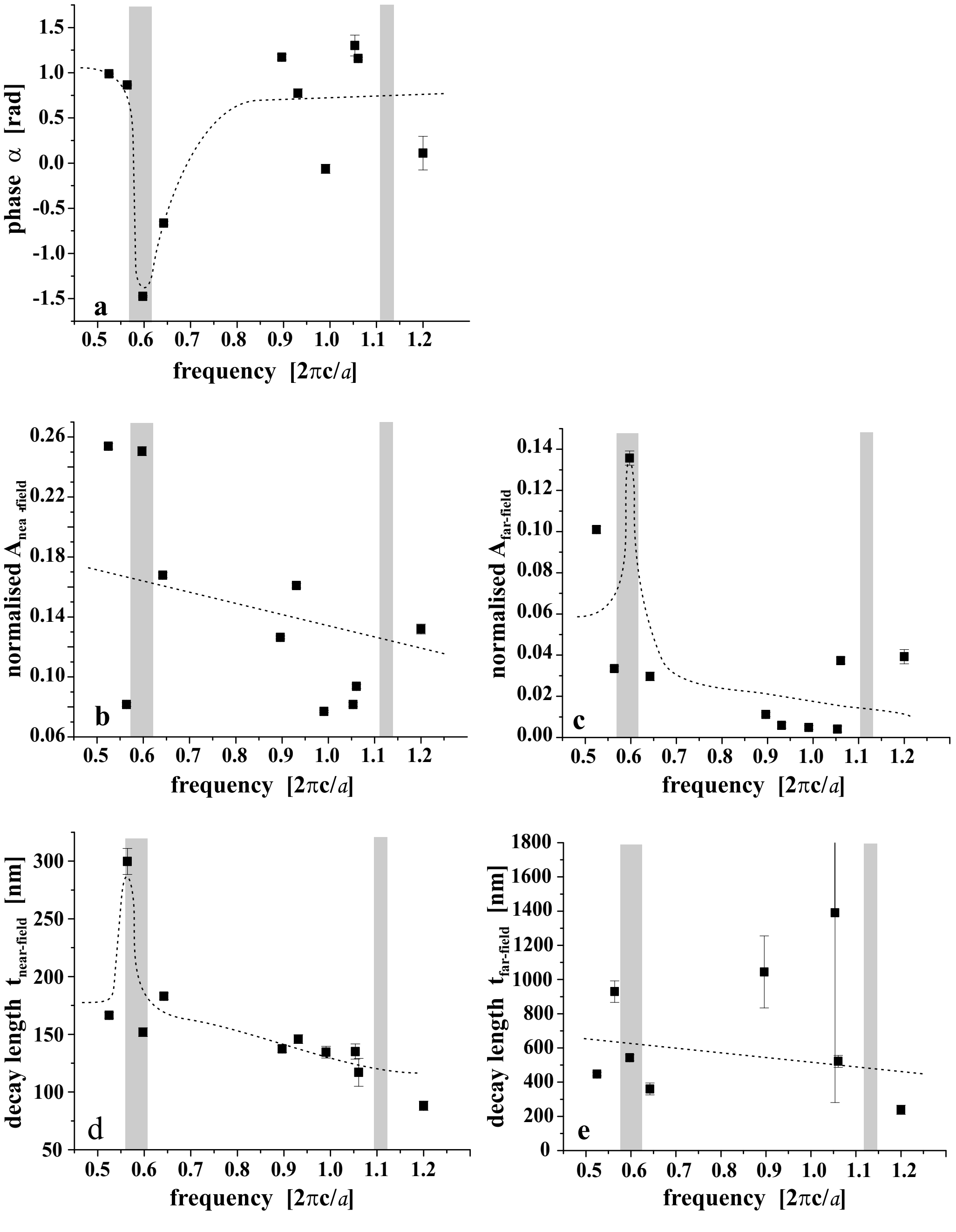

Figure 5.13: Fit parameters obtained by fitting of the approach curves by using Eq. 5.2. The dashed lines act as guides to the eye. An effect of the first order stopgap is found in the phase of the Fabry-Perot fringes. Moreover, the amplitude of the far-field term is higher at the gap frequency. The near-field decay rate also indicates the position of the stopgap.

(see section 5.2). In Fig. 5.13 e, the far field decay length t_{far} is shown. We observe no clear frequency dependency. A longer decay length is found at the low frequency side of the first order stopgap.

The quantitative analysis of approach curves on polystyrene opals shows indication of the stopgap in the phase of the Fabry-Perot fringes. The decay length of the near-field term is increased at the low frequency edge of the first order stopgap along the Γ - L direction.

5.5 Near-field transmission

In the previous sections the relative amount of light transfer to the photonic crystal was investigated as a function of x-, y- and z-position of the fibre probe and as a function of frequency. Now, we determine the absolute values of transmitted light through the crystal for different frequencies when the tip is in contact. We call this the near-field transmission. The measured throughput of light through the crystal needs to be normalised to the amount of light coming directly from the near-field aperture probe. To this end the fibre probe is positioned next to the crystal by lateral movements only. In order to prevent damage to the fragile probe, the probe is first retracted over roughly 50 μm with respect to the in-contact position. Now, all the light coming from the probe is collected by the detector. This provides a far-field determination of the output of our near-field probe. Subsequently, the tip is moved back on top of the crystal. When the tip is positioned on top of the crystal (by x-y displacements only), we go into contact by decreasing the z-distance down to $\sim$10 nm. A small scan similar to those in section 5.3 is performed and a near-field coupling signal is obtained. To check the stability of the in-coupling of light to the fibre probe the direct throughput of the tip is measured again next to the crystal.

Figure 5.14 shows the absolute throughput of the near-field transmission on top of the spheres. The gray areas indicate the first and second order L-gaps at $\omega = 0.60$ and $\omega = 1.13$. We see for low frequencies the highest transmission. The reason for this rather high transmission can be found in the normalisation. The far-field throughput of a near-field probe is much lower then when all the emitted light in both, the forbidden and the allowed angles would be detected, as a result of the crystal's diffraction.

In Fig. 5.14 we see that around $\omega = 0.78$ the throughput increases again. No clear indications of the Γ - L gaps is found in the near-field transmission. As our probe launches more than just normal incident wavevectors into the crystals, i.e., also wavevectors that do not lie in the Γ - L direction, this observation confirms the hypothesis that the present near-field experiments are mostly sensitive to other

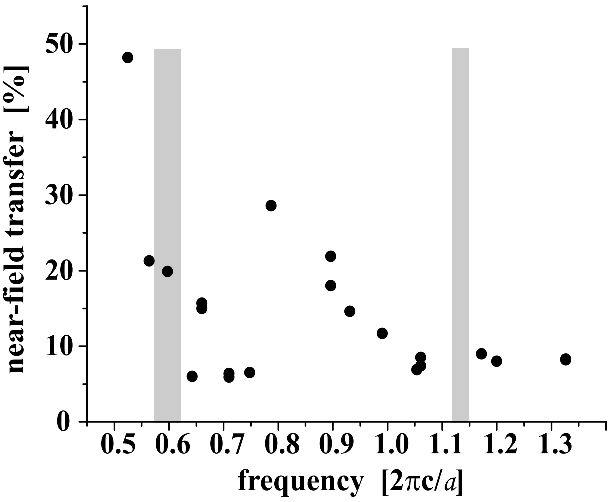

Figure 5.14: Near-field transfer for different frequencies. The gray areas indicate the first and second order stopgap of the polystyrene crystal.

stopgaps, that have been rarely or not studied before.

5.6 Conclusions

We show for the first time that the coupling of light from an external source into a three-dimensional photonic crystal depends both on position and frequency. We have presented local investigation of the coupling mechanism of light coming from a point-like light source to a three-dimensional photonic crystal. Our NSOM setup allows the determination of the position-dependent transfer of light with nanometer accuracy, which is much less than the period of the photonic crystal. On larger sphere size crystals it is observed that more light is launched into the photonic crystal if the probe is located directly above the spheres. The intensity maxima shift and change their shape for different frequencies of light situated near the second order L - gap of the artificial opal. Investigation on small sphere size crystals show inversion of the optical pattern, i.e., more light is transmitted when the near-field probe is positioned in between the spheres. The contrast inversion of the optical near-field pattern is associated to first order stopgaps at the U, K and W points.

We have imaged the light transfer through defects in the <111> surface. We find for large frequencies that less light is coupled, whereas for small frequencies more light is transferred. For a frequency inside the first order L-gap, less light is transmitted at the location of a defect. The obtained near-field measurement show for the first time that coupling of light from an external point-like light source into a three-dimensional photonic crystal depends on the relative launching position with respect to the crystal lattice as well as on the optical frequency. This position dependent transfer of the light through three-dimensional photonic crystals has to our knowledge never been observed before.

Investigation on approach curves performed at different optical frequencies reveal indications on the first order stopgap. At the stopgap frequency, the decay length associated to evanescent light from the tip is two times longer than at all other frequencies. From the interference pattern of the Fabry-Perot fringes, a shift of the cosine at the crystal surface is determined. We observe a change in this shift while tuning the frequency through the stopgaps indicating a reversal of the phase change incurred by the reflection at the crystal surface. In the near-field regime the transmitted intensity increases. Comparison to approach curves obtained on a glass plate confirms that we also detect light that is coupled under forbidden angles into the crystal. Thanks to the diffusion of light in the crystal, detection of this light becomes possible. The increase in intensity due to the forbidden angles is of the order of 10% to 20%.

Near-field transmission measurements were performed. We find that the stopgaps of the crystals do not significantly influence the near-field transmission. We think that the near-field technique can not resolve the influence of the stopgap, because the probe launches light with different wavevectors k into the crystal. As a result, light of all frequencies can find an allowed propagation directions in the crystal and will reach the detector. We propose that our method could be very useful to determine whether a crystals shows a complete three-dimensional photonic bandgap.

The obtained position- and frequency-dependent information of the light transfer consists of different contributions, e.g., coupling of external light to crystal modes, multiple scattering of light or propagation of light through air and crystal. The measurements shown include information about the LDOS at the crystal interface. As a next step, it is desirable to perform theoretical modelling to understand the couplings mechanism and if possible, to separate the various contributions in the measurements. New theoretical models, e.g., [77], [106] as well as FDTD simulations [107] may contribute to the understanding of the new insight about the light transfer, which is gained from the measurements presented in this chapter.

References

[1] in *J. Microscopy* (Blackwell Science, Oxford, 2001), No. 1 & 2.

[2] in *J. Microscopy* (Blackwell Science, Oxford, 2003), No. 3.

[3] *Nano-Optics*, 1st ed., edited by S. Kawata, M. Ohtsu, M. Irie, and M. Ohtsu (Springer Verlag, Berlin, 2002).

[4] J. D. Joannopoulos, R. D. Meade, and J. N. Winn, in *Photonic crystals: Molding the flow of light*, edited by J. D. Joannopoulos (Princeton University press, Princeton, 1995).

[5] K. Sakoda, in *Optical properties of photonic crystals*, edited by K. Sakoda (Springer Verlag, New York, 2001).

[6] *Photonic crystals and light localization in the 21st century*, edited by C. M. Soukoulis (Kluwer Academic Publishers, Dordrecht, 2000).

[7] S. Noda, A. Chutinan, and M. Imada, *Trapping and emission of photons by a single defect in a photonic bandgap structure*, Nature **407**, 608 (2000).

[8] A. F. Koenderink, P. M. Johnson, J. F. Galisteo López, and W. L. Vos, *Three-dimensional photonic crystals as a cage for light*, C. R. Physique **3**, 67 (2002).

[9] O. Painter, K. Srinivas, J. D. O'Brien, A. Scherer, and P. D. Dapkus, *Tailoring of the resonant mode properties of optical microcavities in two-dimensional photonic crystal slab waveguides*, J. Opt. A **3**, 161 (2001).

[10] W. J. Wadsworth, A. Ortigosa-Blanch, J. C. Knight, T. A. Birks, T. P. M. Man, and P. S. Russell, *Supercontinuum generation in photonic crystal fibers and optical fiber tapers: a novel light source*, J. Opt. Soc. Am. B **19**, 2148 (2002).

[11] J. S. Foresi, P. R. Villeneuve, J. Ferrera, E. R. Thoen, G. Steinmeyer, S. Fan, J. D. Joannopoulos, L. C. Kimerling, H. I. Smith, and E. P. Ippen, *Photonic-bandgap microcavities in optical waveguides*, Nature **390**, 143 (1997).

[12] T. Yoshie, J. Vučković, A. Scherer, H. Chen, and D. Deppe, *High quality two-dimensional photonic crystal slab cavities*, Appl. Phys. Lett. **79**, 4289 (2001).

[13] M. Lončar, T. Doll, J. Vučković, and A. Scherer, *Design and fabrication of*

silicon photonic crystal optical waveguides, IEEE J. Lightwave Technol. **18**, 1402 (2000).

[14] E. Yablonovitch, *Photonic crystals: Semiconductors of light*, Scientific American **285**, 46 (2001).

[15] Y. Sugimoto, N. Ikeda, N. Carlsson, K. Asakawa, N. Kawai, and K. Inoue, *Fabrication and characterization of different types of two-dimensional AlGaAs photonic crystal slabs*, J. Appl. Phys. **91**, 922 (2002).

[16] L. Wu, M. Mazilu, T. Karle, and T. F. Krauss, *Superprism phenomena in planar photonic crystals*, IEEE J. Quantum Electron. **38**, 915 (2002).

[17] T. F. Krauss, R. M. De La Rue, and S. Brand, *Two-dimensional photonic-bandgap structures operating at near infrared wavelengths*, Nature **383**, 699 (1996).

[18] J. E. G. J. Wijnhoven and W. L. Vos, *Preparation of photonic crystals made of air spheres in titania*, Science **281**, 802 (1998).

[19] S. Noda, K. Tomoda, N. Yamamoto, and A. Chutinan, *Full three-dimensional photonic bandgap crystals at near-infrared wavelength*, Science **289**, 604 (2000).

[20] C. Kittel, *Einführung in die Festkörperphysik* (Oldenbourg, München, 2002).

[21] N. W. Ashcroft and N. D. Mermin, *Solid State Physics* (Harcourt Brace College Publishers, New York, 1976).

[22] W. L. Vos, R. Sprik, A. Lagendijk, G. H. Wegdam, A. van Blaaderen, and A. Imhof, *Influence of optical band structures on the diffraction of photonic colloidal crystals*, Photonic Band Gap Materials , edited by C.M. Soukoulis (Kluwer, 1996, Dordrecht) 107 (1996).

[23] E. Yablonovitch, *Inhibited spontaneous emission in solid-state physics and electronics*, Phys. Rev. Lett. **58**, 2059 (1987).

[24] F. Koenderink, *Emission and Transport of Light in Photonic Crystals* (Ph.D. Thesis, University of Amsterdam, 2003).

[25] K. Busch and S. John, *Photonic Band Gap Formation in Certain Self-Organizing Systems*, Phys. Rev. E **58**, 3896 (1998).

[26] J. Vučković, M. Lončar, H. Mabuchi, and A. Scherer, *Design of photonic crystal microcavities for cavity QED*, Phys. Rev. E **65**, (2001).

[27] F. Romanato, L. Businaro, E. D. Fabrizio, A. Passaseo, M. D. Vittorio, R. Cingolani, M. Patrini, M. Galli, D. Bajoni, L. C. Andreani, F. Giacometti, M. Gentili, D. Peyrade, and Y. Chen, *Fabrication by means of X-ray lithography of two-dimensional GaAs/AlGaAs photonic crystals with an unconvetional unit cell*, Nanotechnol. **13**, 644 (2002).

[28] W. Bogaerts, V. Wiaux, D. Taillaert, S. Beckx, B. Luyssaert, P. Bienstman, and R. Baets, *Fabrication of photonic cyrstals in silicon-on-insulator using 248-nm deep UV lithography*, IEEE J. Select. Topics Quantum Electron. **8**,

928 (2002).

[29] L. Vogelaar, W. Nijdam, H. A. G. M. van Wolferen, R. M. de Ridder, F. B. Segerink, E. Flück, L. Kuipers, and N. F. van Hulst, *Large area photonic crystal slabs for visible light with waveguiding defect structures: Fabrication with focused ion beam assisted later interference lithography*, Adv. Mater. **13**, 1551 (2001).

[30] J. G. Fleming, S. Y. Lin, I. El-Kady, R. Biswas, and K. M. Ho, *All-metallic three-dimensional photonic crystals with a large infrared bandgap*, Nature **417**, 52 (2002).

[31] M. Campbell, D. N. Sharp, M. T. Harrison, R. G. Denning, and A. J. Turberfield, *Fabrication of photonic crystals for the visible spectrum by holographic lithography*, Nature **404**, 53 (2000).

[32] A. Blanco, E. Chomski, S. Grabtchak, M. Ibisate, S. John, S. W. Leonard, C. Lopez, F. Meseguer, H. Miguez, J. P. Mondia, G. A. Ozin, O. Toader, and H. M. van Driel, *Large-scale synthesis of a silicon photonic crystal with a complete three-dimensional bandgap near 1.5 micrometres*, Nature **405**, 437 (2000).

[33] Y. A. Vlasov, X.-Z. Bo, J. C. Sturm, and D. J. Norris, *On-chip natural assembly of silicon photonic bandgap crystals*, Nature **414**, 289 (2001).

[34] Y.-H. Ye, T. S. Mayer, I.-C. Khoo, I. B. Divliansky, N. Abrams, and T. E. Mallouk, *Self-assembly of three-dimensional photonic-crystals with air-core line defects*, J. Mater. Chem. **12**, 3637 (2002).

[35] S. N. Kurilkina and M. V. Shuba, *Propagation and transformation of light waves in magnetically active periodic structures*, Opt. and Spectrosc. **93**, 913 (2002).

[36] K. Kempa, B. Kimball, J. Rybczynski, Z. P. Huang, P. F. Wu, D. Steeves, M. Sennett, M. Giersig, D. V. G. L. N. Rao, D. L. Carnahan, D. Z. Wang, J. Y. Lao, W. Z. Li, and Z. F. Ren, *Photonic crystals based on periodic arrays of aligned carbon nanotubes*, Nano Lett. **3**, 13 (2003).

[37] J. R. Krenn, *Nanoparticle waveguides - Watching energy transfer*, Nature Mater. **2**, 210 (2003).

[38] M. Kranskar, P. Paddon, V. Pacradouni, R. Morin, A. Busch, J. F. Young, S. R. Johnson, J. MacKenzie, and T. Tiedje, *Observation of leaky slab modes in an air-bridge semiconductor waveguide with a two-dimensional photonic lattice*, Appl. Phys. Lett. **70**, 1438 (1997).

[39] J. E. G. J. Wijnhoven, L. Bechger, and W. L. Vos, *Fabrication and characterization of large macroporous photonic crystals in titania*, Chem. Mater. **13**, 4486 (2001).

[40] B. Hecht, D. W. Pohl, H. Heinzelmann, and L. Novotny, *Tunnel near-field optical microscopy: TNOM-2*, Ultramicroscopy **61**, 99 (1995).

[41] M. H. P. Moers, N. F. van Hulst, A. G. T. Ruiter, and B. Bölger, *Optical contrast in near-field techniques*, Ultramicroscopy **57**, 298 (1995).

[42] M. L. M. Balistreri, J. P. Korterik, G. J. Veldhuis, L. Kuipers, and N. F. van Hulst, *Quantitative photon tunelling and shear-force microscopy of planar waveguide splitters and mixers*, J. Appl. Phys. **89**, 3307 (2001).

[43] E. Betzig and R. J. Chichester, *Single molecules observed by near-field scanning optical microscopy*, Science **262**, 1422 (1993).

[44] A. Hartschuh, E. J. Sanches, X. S. Xie, and L. Novotny, *High-resolution near-field raman microscopy of single-walled carbon nanotubes*, Phys. Rev. Lett. **90**, 095503 (2003).

[45] R. M. Stockle, N. Schaller, V. Deckert, C. Fokas, and R. Zenobi, *Brighter near-field optical probes by means of improving the optical destruction threshold*, J. Microscopy **194**, 378 (1999).

[46] S. Fan, I. Appelbaum, and J. D. Joannopoulos, *Near-field scanning optical microscopy as a simultaneous probe of fields and band structure of photonic crystals: A computational study*, Appl. Phys. Lett. **75**, 3461 (1999).

[47] J.-A. Veerman, A. M. Otter, L. Kuipers, and N. F. van Hulst, *High definition aperture probes for near-field optical microscopy fabricated by focused ion beam milling*, Appl. Phys. Lett. **72**, 3115 (1998).

[48] M. Spajer, G. Parent, C. Bainier, and D. Charraut, *Shaping the reflection near-field optical probe: finite domain time difference modelling and fabrication using a focused ion beam*, J. Microscopy **202**, 45 (2001).

[49] A. Naber, D. Molenda, U. C. Fischer, H. J. Maas, C. Hoppener, N. Lu, and H. Fuchs, *Enhanced light confinement in a near-field optical probe with a triangular apterture*, Phys. Rev. Lett. **89**, 210801 (2002).

[50] N. F. van Hulst, F. B. Segerink, F. Achten, and B. Bölger, *Evanescent-field optical microscopy: effects of polarization, tip shape and radiative waves*, Ultramicroscopy **42–44**, 416 (1992).

[51] K. Karrai and R. D. Grober, *Piezoelectric tip-sample distance control for near field optical microscopes*, Appl. Phys. Lett. **66**, 1842 (1995).

[52] M. Vaez-Iravani and R. Toledo-Crow, *Phase contrast and amplitude pseudo-heterodyne interference near field scanning optical microscopy*, Appl. Phys. Lett. **62**, 1044 (1993).

[53] M. L. M. Balistreri, J. P. Korterik, L. Kuipers, and N. F. van Hulst, *Phase mapping of optical fields in integrated optical waveguide structures*, IEEE J. Lightwave Technol. **19**, 1169 (2001).

[54] A. G. T. Ruiter, J.-A. Veerman, K. O. van der Werf, and N. F. van Hulst, *Dynamic behavior of tuning fork shear-force feedback*, Appl. Phys. Lett. **71**, 28 (1997).

[55] E. B. McDaniel, J. W. P. Hsu, L. S. Goldner, R. J. Tonucci, E. L. Shirley,

and G. W. Bryant, *Local characterization of transmission properties of a two-dimensional photonic crystal*, Phys. Rev. B **55**, 10878 (1997).

[56] C. Chicanne, T. David, R. Quidant, J. C. Weeber, Y. Lacroute, E. Bourillot, and A. Dereux, *Imaging the local density of states of optical corrals*, Phys. Rev. Lett. **88**, 097402 (2002).

[57] B. Hecht, H. Bielefeldt, Y. Inouye, and D. W. Pohl, *Facts and artifacts in near-field optical microscopy*, J. Appl. Phys. **81**, 2492 (1997).

[58] M. L. M. Balistreri, J. P. Korterik, L. Kuipers, and N. F. van Hulst, *Photon scanning tunneling optical microscopy with a three-dimensional multiheight imaging mode*, Appl. Phys. Lett. **77**, 4092 (2000).

[59] Y. Sugimoto, N. Ikeda, N. Carlsson, K. Asakawa, N. Kawai, and K. Inoue, *Light-propagation characteristics of Y-branch defect waveguides in AlGaAs-based air-bridge-type two-dimensional photonic crystal slabs*, Opt. Lett. **27**, 388 (2002).

[60] S. Boscolo, M. Midrio, and T. F. Krauss, *Y junctions in photonic crystal channel waveguides: high transmission and impedance matching*, Opt. Lett. **27**, 1001 (2002).

[61] M. Notomi, K. Yamada, A. Shinya, J. Takahashi, C. Takahashi, and I. Yokohama, *Extremely large group-velocity dispersion of line-defect waveguides in photonic crystal slabs*, Phys. Rev. Lett. **87**, 253902 (2001).

[62] M. D. Rahn, A. M. Fox, M. S. Skolnick, and T. F. Krauss, *Propagation of ultrashort nonlinear pulses through two-dimensional AlGaAs high-contrast photonic crystal waveguides*, J. Opt. Soc. Am. B **19**, 716 (2002).

[63] S. Fan and J. D. Joannopoulos, *Analysis of guided resonances in photonic crystal slabs*, Phys. Rev. B **65**, 235112 (2002).

[64] V. N. Astratov, I. S. Culshaw, R. M. Stevenson, D. M. Whittaker, M. S. Skolnick, T. F. Krauss, and R. M. De La Rue, *Resonant coupling of near-infrared radiation to photonic band structure waveguides*, IEEE J. Lightwave Technol. **17**, 2050 (1999).

[65] V. Pacradouni, W. J. Mandeville, A. R. Cowan, P. Paddon, J. F. Young, and S. R. Johnson, *Photonic band structures of dielectric membranes periodically textured in two dimensions*, Phys. Rev. B **62**, 4204 (2000).

[66] M. Galli, M. Agio, L. C. Andreani, L. Atzeni, D. Bajoni, G. Guizzetti, L. Busnaro, E. D. Fabrizio, F. Romanato, and A. Passaseo, *Optical properties and photonic bands of GaAs photonic crystal waveguides with tilted square lattice*, Europhys. J. B **27**, 79 (2002).

[67] M. S. Thijssen, R. Sprik, J. E. G. J. Wijnhoven, M. Megens, T. Narayanan, A. Lagendijk, and W. L. Vos, *Inhibited light propagation and broadband reflection in photonic air-sphere crystals*, Phys. Rev. Lett. **83**, 2730 (1999).

[68] A. G. Choo, M. H. Chudgar, H. E. Jackson, G. N. De Brabander, M. Kumar,

and J. T. Boyd, *Photon scanning tunneling microscopy on optical waveguides*, Ultramicroscopy **57**, 124 (1995).

[69] H. E. Jackson, S. M. Lindsay, C. D. Poweleit, D. H. Naghski, G. N. De Brabander, and J. T. Boyd, *Near field measurements of optical channel waveguide structures*, Ultramicroscopy **61**, 295 (1995).

[70] M. L. M. Balistreri, D. J. W. Klunder, J. P. Korterik, F. C. Blom, A. Driessen, H. W. J. M. Hoekstra, L. Kuipers, and N. F. van Hulst, *Visualizing the whispering gallery modes in a cylindrical optical microcavity*, Opt. Lett. **24**, 1829 (1999).

[71] A. Nesci, R. Dändliker, and H. P. Herzig, *Quantitative amplitude and phase measurements by use of a heterodyne scanning near-field optical microscope*, Opt. Lett. **26**, 208 (2001).

[72] G. H. Vander Rhodes, M. S. Ünlü, B. B. Goldberg, J. M. Pomeroy, and T. F. Krauss, *Characterisation of waveguide microcavities using high-resolution transmission spectroscopy and near-field scanning optical microscopy*, IEE Proc.-Optoelectron. **145**, 379 (1998).

[73] A. L. Campillo, J. W. P. Hsu, C. A. White, and A. Rosenberg, *Mapping the optical intensity distribution in photonic crystals using a near-field scanning optical microscopy*, J. Appl. Phys. **89**, 2801 (2001).

[74] S. I. Bozhevolnyi, V. S. Volkov, T. Søndergaard, A. Boltasseva, P. I. Borel, and M. Kristensen, *Near-field imaging of light propagation in photonic crystal waveguides: Explicit role of Bloch harmonics*, Phys. Rev. B **66**, 235204 (2002).

[75] J. R. Krenn, A. Dereux, J. C. Weeber, E. Bourillot, Y. Lacroute, J. P. Gourdonnet, G. Schider, W. Gotschy, A. Leitner, F. R. Aussenegg, and C. Girard, *Squeezing the optical near-field zone by plasmon coupling of metallic nanoparticles*, Phys. Rev. Lett. **82**, 2590 (1999).

[76] P. Kramper, A. Birner, M. Agio, C. M. Soukoulis, F. Müller, U. Gösele, J. Mlynek, and V. Sandoghdar, *Direct spectroscopy of a deep two-dimensional photonic crystal microresonator*, Phys. Rev. B **64**, 233102 (2001).

[77] G. Colas des Francs, C. Girard, J.-C. Weeber, C. Chicanne, T. David, A. Dereux, and D. Peyrade, *Optical Analogy to Electronic Quantum Corrals*, Phys. Rev. Lett. **86**, 4950 (2001).

[78] R. Riehn, A. Charas, J. Morgado, and F. Cacialli, *Near-field optical lithography of a conjugated polymer*, Appl. Phys. Lett. **82**, 526 (2003).

[79] T. Tamir, *Integrated Optics* (Springer-Verlag, Berlin, 1975).

[80] M. Lohmeyer and R. Stoffer, *Integrated optical cross strip polarizer concept*, Opt. Quantum Electron. **33**, 413 (2001).

[81] M. Lohmeyer, *Mode expansion modeling of rectangular integrated optical microresonators*, Opt. Quantum Electron. **34**, 541 (2002).

[82] M. L. M. Balistreri, J. P. Korterik, L. Kuipers, and N. F. van Hulst, *Local observation of phase singularities in optical fields in waveguide structures*, Phys. Rev. Lett. **85**, 294 (2000).

[83] M. L. M. Balistreri, A. Driessen, J. P. Korterik, L. Kuipers, and N. F. van Hulst, *Quasi interference of perpendicularly polarized guided modes observed with a photon scanning tunneling microscope*, Opt. Lett. **25**, 637 (2000).

[84] M. Patrini, M. Galli, F. Marabelli, M. Agio, L. C. Andreani, D. Peyrade, and Y. Chen, *Photonic Bands in patterned silicon-on-insulator waveguides*, IEEE J. Quantum Electron. **38**, 885 (2002).

[85] I. S. Culshaw, V. N. Astratov, R. M. Stevenson, D. M. Whittaker, M. S. Skolnick, T. F. Krauss, and R. M. De La Rue, *Determination of the band structure of photonic crystal waveguides*, Physica E **7**, 650 (2000).

[86] U. Fano, *Effects of configuration interaction on intensities and phase shifts*, Phys. Rev. **124**, 1866 (1961).

[87] B. Kim and K. Yoshihara, *Multichannel quantum interference in the predissociation of Cs_2: Observation of q-reversal in complex resonance*, J. Chem. Phys. **99**, 1433 (1993).

[88] V. N. Astratov, D. M. Whittaker, I. S. Culshaw, R. M. Stevenson, M. S. Skolnick, T. F. Krauss, and R. M. De La Rue, *Photonic band-structure effects in the reflectivity of periodically patterned waveguides*, Phys. Rev. B **60**, 16255 (1999).

[89] J. Mouette, C. Seassal, X. Letartre, P. Rojo-Romeo, J.-L. Leclerq, P. Regreny, P. Viktorovitch, E. Jalaguier, P. Perreau, and H. Moriceau, *Very low threshold vertical emitting laser operation in InP graphite photonic crystal slab on silicon*, Electron. Lett. **39**, 526 (2003).

[90] J. M. Pottage, E. Silvestre, and P. S. Russell, *Vertical-cavity surface-emitting resonances in photonic crystal films*, J. Opt. Soc. Am. A **18**, 442 (2001).

[91] T. J. Karle, D. H. Brown, R. Wilson, M. Steer, and T. F. Krauss, *Planar photonic crystal coupled cavity waveguides*, IEEE J. Select. Topics Quantum Electron. **8**, 909 (2002).

[92] M. L. M. Balistreri, H. Gersen, J. P. Korterik, L. Kuipers, and N. F. van Hulst, *Tracking femtosecond laser pulses in space and time*, Science **294**, 1080 (2001).

[93] J. D. Jackson, *Classical electrodynamics* (John Wiley and Sons, Berkeley, 1998).

[94] P. Mach, P. Wiltzius, M. Megens, D. A. Weitz, K. H. Lin, T. C. Lubensky, and A. G. Yodh, *Electro-optic response and switchable Bragg diffraction for liquid crystals in colloid-templated materials*, Phys. Rev. E **65**, 031720 (2002).

[95] R. Sprik, B. A. van Tiggelen, and A. Lagendijk, *Optical emission in periodic*

dielectrics, Europhys. Lett. **35**, 265 (1996).

[96] K. Busch, N. Vats, S. John, and B. C. Sanders, *Radiating dipoles in photonic crystals*, Phys. Rev. E **62**, 4251 (2000).

[97] Y. A. Vlasov, M. Deutsch, and D. J. Norris, *Single-domain spectroscopy of self-assembled photonic crystals*, Appl. Phys. Lett. **76**, 1627 (2000).

[98] J. F. Galisteo L**ò**pez and W. L. Vos, *Angle-resolved reflectivity of single-doain photonic crystals: Effects of disorder*, Phys. Rev. E **66**, 036616 (2002).

[99] W. L. Vos and H. M. van Driel, *Higher order Bragg diffraction by strongly photonic fcc crystals: onset of a photonic bandgap*, Phys. Lett. A **272**, 101 (2000).

[100] A. F. Koenderink, M. Megens, G. van Soest, W. L. Vos, and A. Lagendijk, *Enhanced backscattering from photonic crystals*, Phys. Lett. A **268**, 104 (2000).

[101] *The optical principles of the diffraciton of x-rays*, edited by R. W. James (OX Bow Press, Woodbridge, Connecticus, 1982).

[102] R. D. Meade, A. M. Rappe, K. D. Brommer, and J. D. Joannopoulos, *Nature of the photonic band-gap: some insights from a field analysis*, J. Opt. Soc. Am. B **10**, 328 (1993).

[103] O. Y. Kolensychenko, R. de Kort, M. I. Katsnelson, A. I. Lichtenstein, and H. van Kempen, *Real-space imaging of an orbital Kondo resonance on the Cr(001) surface*, Nature **415**, 507 (2002).

[104] H. A. McKay, R. M. Feenstra, P. J. Poole, and G. C. Aers, *Cross-sectional scanning tunneling microscopy studies of lattice-matched InGaAs/InP quantum wells: variations in growth switching sequence*, J. Cryst. Growth **249**, 437 (2003).

[105] R. Valleé, N. Tomczak, H. Gersen, E. M. H. P. van Dijk, M. F. Garcia-Parajó, G. J. Vancso, and N. F. van Hulst, *On the role of electromagnetic boundary conditions in single molecule fluorescence lifetime studies of dyes embedded in thin films*, Chem. Phys. Lett. **348**, 161 (2001).

[106] R. Carminati and J. J. Sáenz, *Scattering Theory of Bardeen's Formalism for Tunneling: New Approach for Near-Field Microscopy*, Phys. Rev. Lett. **84**, 5156 (2000).

[107] J. S. Kole, M. T. Figge, and H. De Raedt, *Unconditionally stable algorithms to solve the time-dependent Maxwell equations*, Phys. Rev. E **64**, 066705 (2001).

Acknowledgements

I would like to thank everyone who contributed directly or indirectly to the success of this work. It is obvious that such results can be only achieved in teamwork and with lots of feedback of colleagues and friends. Many thanks to my friends, who supported me especially in not so easy times of the last four years. You are indispensable for me!

The work in the Applied Optics group at the University of Twente was very intriguing for me and the task to combine two fields of research (near-field microscopy and photonic crystals) was exciting and challenging. The good atmosphere in the group motivated me a lot during the four years. I very much appreciated to work with all the people of the group and I would like to thank them very much for the nice time. I would like to thank in particular my supervisors Niek van Hulst and Kobus Kuipers. Their enthusiasm and ideas have led to the results presented in this thesis.

For the fabrication of the one-dimensional structures, produced by focussed ion beam, I would like to thank Bert Otter from the MESA$^+$ Research Institute. He managed to deal with charging effects as well as to overcome the steering limits of the focused ion beam, which makes him an essential assistant of focused ion beam work. The two-dimensional photonic crystal slabs were fabricated by Laura Vogelaar (master student of our group). She developed a new technique based on laser interference lithography that enables fabrication of large area photonic crystals. Further, I thank Lydia Bechger from the group of Complex Photonic Systems (COPS) for the fabrication of the polystyrene opals and for her support and expertise in the handling of the small crystals. Also many thanks to Peter Lodahl (COPS) for his help with the Biorad Fourier-Transform spectrometer. The fabrication of the near-field optical fibre probes was performed in the MESA$^+$ cleanroom, where I am grateful for the assistance of Johnny Sanderink and Hans Mertens for the evaporation of the metal coating. For the fabrication of the waveguide ridges and for calculations of leaky modes, I would like to thank the colleagues of the Lightwave Device Group.

Some measurements presented in this thesis were performed by master students of our group. I would like to acknowledge them for their contributions. These are Casper Peeters for the measurements on the single slit in a waveguide (section 3.1.1), Erik van Dijk for the three-dimensional measurements on the two slits in a waveguide (section 3.2.3) and Gijs van Duinen for the angle-dependent reflectivity measurements on the two-dimensional photonic crystal slabs (section 4.1.2).

The theoretical band structure calculations for the two-dimensional photonic crystal slab have been provided by Christian Hermann and Heiko Pittner of the group for Theoretical Quantum Electronics at the Institute of Technical Physics (DLR) in Stuttgart. Thanks to them for their endeavour and for many discussions. For the three-dimensional photonic crystals, Femius Koenderink from the group COPS calculated the band structure. He was always ready to answer my questions. The two-dimensional calculations used for the interpretation of the optical field distributions obtained by PSTM on the 15 slit and 15 air rod structures were performed by Manfred Hammer of the group AAMP. Thanks to many discussions we finally understood the interference pattern behind the 15 slit structure. For the collaboration on three-dimensional photonic crystals, I would like to thank Willem Vos (COPS) for the fruitful discussions and his help in analysing and interpreting the near-field data.

For the technical support on the measurement setups I would like to thank Jeroen Korterik and Frans Segerink. They always helped very quickly and improved the setups over time. Many thanks to Erik van Dijk for the implementation of the three-dimensional measurement mode in the near-field setups. I thank Klaas Smit from the mechanical workshop at the University for fabrication of the vacuum holders, that had to be fabricated very accurately. I would like to thank all the staff members of the MESA$^+$ for their help and enthusiasm, which made it very pleasant experience to work in the cleanroom.

Finally, I would like to thank the members of the thesis jury for their constructive suggestions and for the motivating discussions in the last months.

Eliane Flück
Enschede, May 2003

Summary

Photonic crystals are structures with a strong relation between geometry and optical properties. The application of near-field methods is a new and challenging approach to investigate the local optical properties of photonic crystals. The optical signals obtained in crystal structures of various dimensionalities can be directly related to the local geometry of the structure. In contrast to this local probe technique that enables sub-wavelength resolution, far-field approaches return information that is spatially averaged. Reflectivity experiments, for example, reveal the long-range quality of a crystalline structure or the effect of stopgaps on the overall light propagation. By combining the complementary near-field and far-field results, a complete picture of the optical properties in a photonic crystal structure emerges.

A theoretical introduction on photonic crystals is provided in chapter 1. For the infinite one-dimensional case the dispersion relation is introduced. Subsequently, the two specific cases of a photonic crystal slab and a three-dimensional polystyrene opal are discussed in detail. The second part of the chapter deals with the methods used to fabricate the photonic crystal structures investigated in this thesis. To fabricate different sub-wavelength features of any size and in a periodic arrangement, we use a focused ion beam (FIB). High-energy heavy ions locally sputter material away to create a nanoscale arrangement of alternating refractive indices. For the fabrication of a large two-dimensional periodic structure, a holographic method is applied to illuminate photo resist. After lift-off and etching processes a freestanding membrane containing a hexagonal arrangement of air rods is produced. Three-dimensional photonic crystals are made by self-assembly of polystyrene spheres. The close packed face centred cubic lattice crystals (artificial opals) show photonic stopgaps along different crystalline directions.

Different methods, both near-field and far-field, have been used to investigate photonic structures. In the most frequently used methods both the light source and the detector are in the far-field. We have used such far-field methods to determine the stopgaps of the two-dimensional photonic crystal slab and the three-dimensional photonic crystals. Moreover, top reflection measurements on

the two-dimensional freestanding membrane allow so-called resonant modes to be probed. The method is elucidated theoretically in chapter 2. Moreover, the working principle of near-field detection is explained as well as the fabrication process of near-field probes. In this thesis, two different near-field optical instruments are used: a photon scanning tunnelling microscope (PSTM) and a near-field scanning optical microscope (NSOM). In the PSTM the sub-wavelength aperture fibre probe is used as detector, whereas in the NSOM, the probe provides a point-like light source. Both setups can be operated in a three-dimensional (3D) measurement mode, such that retraction and approach curves can be measured. Moreover, the PSTM enables the measurement of the optical phase simultaneously with the local intensity of light and the topography of the structure.

In chapter 3 different one-dimensional photonic structures produced by FIB milling are investigated with the PSTM. The optical field distribution of light around 15 air rods and 15 slits in a waveguide ridge show a standing wave in front of the structure. Inside the arrays themselves, the decay of the optical intensity is measured. The losses of the array are determined from the intensity decay as a function of position. The decay inside the array is found to be wavelength dependent. A faster decay rate for shorter wavelength of light suggests that losses arising from scattering processes produce the decay in intensity. Behind the 15 slit array an unexpected, wavelength-dependent recovery process is observed. The underlying interference is caused by light propagating through the array and light reflected by substrate layers underneath the waveguide. The fact that reflections from underlying substrate layers can find their way back into photonic structures, bypassing photonic crystal regions, may have repercussions for cross-talk in photonic crystal circuits based on, for example, silicon-on-insulator technology. On the 15 air rod structure the phase information of light is analysed as well. In the air rod region, we find indications of a local change in the effective refractive index. Overall, the air rod array produces circularly shaped scattered waves that interfere with the propagating waves. As a result, in a complex interference pattern is built up, which shows a network of phase singularities and phase jumps. These field and phase measurements show that a PSTM can reveal complex local scattering phenomena, which remain hidden in far-field investigations. In the last part of chapter 3 we demonstrate the importance of the three-dimensional measurement mode. Thus, the evanescent fields and propagating scattered light can be separated, as is illustrated on scattering by two slits in a waveguide ridge. The 3D measurement mode also allows evolution of phase singularities in space to be visualized. For a waveguide that contains 4 guided modes, we observe the creation of a pair of phase singularities as the height above the waveguide is increased.

A two-dimensional photonic crystal slab is characterised by far-field reflectivity measurements and the results are discussed in chapter 4. Through these measurements it is possible to investigate the coupling to resonant modes (or leaky modes) of the photonic crystal slab. The excitation of such a mode produces a sharp feature with a dispersive line shape in the reflectivity spectrum. The origin of the sharp features is interference between light propagating along two different pathways: a direct reflection and reflection via the resonant mode. Through a determination of the dispersion of the features part of the band structure, above the light line, of the photonic slab is reconstructed. Excellent agreement with the calculations is found. In the second part of chapter 4, the actual line shape of the resonance features is investigated in more detail. To this end, the theory introduced by Fano, for the description of inelastic scattering of electrons on Helium atoms, is translated to the photonic case to fit the data. We find that the line width of the observed resonaces is extremely narrow, which indicates the high quality of our large photonic crystal. The theory introduces a coupling parameter q that describes the ratio of two transition probabilities. For TM polarised light we observe a reversal in the sign of the coupling parameter q at certain $k_{//}$. This sign reversal signifies a phase change of light in one of the two interference pathways. A possible explanation is that a phase change occurs in the directly reflected light pathway while tuning the incident angle through a Brewster-like angle. It is remarkable that this angle is determined by an effective refractive index of the photonic crystal slab and not by its band structure.

In chapter 5, the transfer of light coming from a point-like light source, which couples to a three-dimensional photonic crystal and subsequently propagates through it, is investigated by using the NSOM. For different normalised frequencies we find a position dependence of the transfer. For high frequencies more light is transmitted through the crystals when the fibre probe is positioned on top of a sphere, whereas less light is transmitted in between the spheres. For low normalised frequencies, the near-field transfer pattern is inverted in intensity, thus more light is transmitted in between the spheres and less light through the spheres. The inclusion of a defect in the <111> surface affects the local coupling of light strongly. For low frequencies (except for a frequency in the first order L-gap) we find a high throughput at the defect. For high frequencies and a frequency in the first order L-gap less light enters through defects. We find that the near-field investigations have the potential to locate defects underneath the first layer of polystyrene spheres. Investigations on approach curves performed at different optical frequencies indicate the effect of the first order stopgap on the near-field coupling. At the stopgap frequency, the decay length associated to evanescent light from the crystal is two times longer than for other frequencies. In addition, a high modulation of Fabry-Perot fringes is found for frequencies near the stopgap. The near-field technique reveals the complex coupling of light at the interface of a three-dimensional photonic crystal.

Summary

This thesis describes a rich variety of optical behaviour in photonic crystal structures. Local visualization of light propagation allows the direct determination of losses and refractive indices and the observation of complex interference phenomena like the formation of phase singularity networks. Both local and spatially averaging techniques have been used to investigate the coupling of light to photonic crystals. We find that coupling to resonant modes can exhibit so-called q-reversal. The near-field coupling of light coming from a point-like light source is found to be both position-dependent and frequency dependent. This coupling is strongly influenced by local defects in the crystal.

Samenvatting

Fotonische kristallen zijn optische materialen met structuur op de schaal van de golflengte waardoor de optische eigenschappen zeer sterk van de geometrie afhangen. In dit proefschrift worden de lokale optische eigenschappen van een fotonische kristal onderzocht met een nabije-veld methode. De op deze manier verkregen optische informatie van licht binnenin de structuur wordt direct gerelateerd aan de geometrie. Tegenover een dergelijke lokale meettechniek, die een resolutie oplevert kleiner dan de golflengte van licht, staan verre-veld methoden, die de optische eigenschappen ruimtelijk middelen en dus globale informatie meten. Metingen van gereflecteerd licht openbaren bijvoorbeeld de kwaliteit van de kristal structuur of effecten van een verboden frequentie band (in een richting) op de voortplanting van het licht. Door de twee technieken, de nabije- en de verre-veld methode, gecombineerd te gebruiken, wordt het mogelijk om een compleet beeld van het gedrag van licht in een fotonisch kristal te verkrijgen.

In hoofdstuk 1 is the theorie van fotonische kristallen beschreven. De optische dispersie relatie wordt eerst toegelicht aan de hand van een oneindig lange een-dimensionale structuur. Vervolgens worden de specifieke gevallen van een fotonische kristal plak en een drie-dimensionaal polystyreen opaal besproken. In het tweede deel van dit hoofdstuk worden de gebuikte methodes voor het vervaardigen van de kristallen toegelicht. Voor het maken van verschillende zeer kleine periodieke structuren is een gefocusseerde ionenbundel (FIB) gebruikt. De ionen worden met een hoge energie op het substraat geschoten, waardoor het mogelijk is om lokaal vormpjes op een schaal van nanometers in het materiaal te boren. Voor de fabricage van grote twee-dimensionale periodieke structuren is van een interferometrische opstelling gebruik gemaakt om fotoresist te belichten. Na een lift-off en een ets proces ontstaat een vrijhangende membraan met een hexagonaal gatenpatroon. De drie-dimensionale fotonische kristallen zijn gemaakt op basis van kleine polystyreen bolletjes, die door zelforganisatie een kristal vormen. Dit kristal heeft verboden frequentie banden in verschillende richtingen.

Verschillende methoden, zowel nabije- als ook verre-veld technieken gebruikt, om fotonische kristallen te bestuderen, worden beschreven in hoofdstuk 2. Meestal bevinden zich de lichtbron en ook de detector in het verre-veld. Wij hebben een dergelijke methode gebruikt, om de verboden frequentie banden van de tweedimensionaal fotonische kristal plak en van de drie-dimensionale opaal te bepalen. Bovendien zijn er hoekafhankelijke reflectiviteitsmetingen aan de vrijhangende membraan uitgevoerd. Daarmee is het mogelijk aan resonante modi van het kristal te koppelen. Dit wordt schematisch toegelicht. Verder wordt in dit hoofdstuk uitgelegd, hoe nabije-veld methodes werken en hoe de scherpe nabije-veld tipjes worden gemaakt. Wij gebruiken twee verschillende nabije-veld methodes: een "photon scanning tunnelling microscope (PSTM)" en een "near-field scanning optical microscope (NSOM)". In een PSTM word het scherpe tipje gebruikt als detector en in een NSOM wordt een dergelijke tipje gebruikt als optische puntbron. In beide opstellingen zijn zogeheten drie-dimensionale metingen mogelijk, waarmee retractie- en naderingscurven gemeten worden. De PSTM geeft bovendien de mogelijkheid om de optische fase van het licht binnenin in een structuur te meten. Dit wordt dan simultaan gedaan met een meting van de lokale intensiteit van het licht en de topografie van de structuur.

In hoofdstuk 3 worden de resultaten van het onderzoek met de PSTM aan verschillende, met FIB vervaardigde structuren besproken. In de veldverdelingen van licht in een golfgeleider met 15 gaten of 15 spleten vinden we staande golven voor het begin van de gaten of spleten. In de periodieke structuur zelf is een afname van de intensiteit te herkennen. Uit deze afname kan het verlies van licht worden berekend. Wij stellen vast, dat de afname van intensiteit (en dus de hoeveelheid verloren licht) golflengte afhankelijk is. Aangezien het verlies groter wordt voor kortere golflengten lijkt het erop dat het verlies wordt veroorzaakt door verstrooiing. Achter de 15 spleten vinden we een onverwacht golflengte afhankelijk verschijnsel bij de opbouw van de golfgeleider mode. Het is een interferentie die wordt opgebouwd uit licht, dat zich direct door de periodieke structuur heeft voortgeplant en licht, dat aan het onderliggend substraat word weerkaatst. Het feit dat er licht om de structuur heen komt zonder deze te voelen is een belangrijke ontdekking omdat het laat zien dat er eventueel overspraak kan ontstaan in optische circuits op basis van fotonische kristallen die gemaakt zijn met een silicium-op-isolator technologie. Aan de structuur met 15 gaten bekijken we de fase van het licht. De lokale verandering van de effectieve brekingsindex van het materiaal wordt zichtbaar in de metingen. De gaten verstrooien het licht in bolgolven, welke interfereren met het inkomende licht. Het resultaat ervan is een ingewikkeld netwerk van fasesingulariteiten en fasesprongen. De met de PSTM gemeten lokale optische veldverdelingen en de faseevolutie laten optische verschijnselen zien die met verre-veld methodes onmogelijk te zien zijn. In het laatste deel van hoofdstuk 3 wordt gedemonstreerd, hoe belangrijk de drie-dimensionale meetmethode is. Met behulp van retractie- en naderingscurven kan evanescent licht van verstrooid licht worden onderscheiden. Dit wordt aan de hand van verstrooiing aan twee spleten in een golfgeleider duidelijk gemaakt. Bovendien wordt de vorm van een fasesingulariteit voor verschillende tip-substraat afstanden bekeken. Wanneer 4 modi in de golfgeleider aangeslagen worden, kan de creatie van een paar tegengestelde fasesingulariteiten worden gevisualiseerd.

In hoofdstuk 4 is een twee-dimensionaal fotonisch kristal plak met behulp van verre-veld methodes onderzocht. Met de methode is het mogelijk om zogeheten resonante modi van de structuur aan te slaan. Als gevolg is er in het spectrum van het gereflecteerde licht een scherp piekje te zien. De vorm van de piek wordt bepaald door interferentie van licht dat zich langs twee verschillende kanalen voortplant: directe weerkaatsing aan de fotonische kristal plak en weerkaatsing via een resonante mode. De bepaling van de optische frequentie van de resonantie wordt gebruikt om een deel van de dispersie relatie van de fotonische kristal plak te reconstrueren. De resultaten komen goed overeen met modelberekeningen. In het tweede deel van hoofdstuk 4 wordt de vorm van de resonanties beter bekeken. Daarvoor hebben we een theorie gebruikt, die oorspronkelijk voor de beschrijving van verstrooiingsexperimenten van elektronen aan een Helium atoom is ontwikkeld. De lijnbreedte van de pieken blijkt zeer smal te zijn, wat duidt op een hoge kwaliteit van onze grote fotonische kristallen. De theorie maakt ook gebruik van een koppelingparameter q, die is gedefiniëerd als de verhouding tussen twee overgangswaarschijnlijkheden. Voor TM gepolariseerd licht wordt een omslag van het teken van de koppelingparameter q gevonden. Deze omslag van het teken betekent dat er een verandering is opgetreden in de fase van het licht in een van de twee interferentie kanalen. Een mogelijke verklaring kan zijn dat er een Brewster hoek bestaat voor de fotonische kristal plak. Als de hoek van het inkomende licht wordt verdraaid door de Brewster hoek heen, dan zal het teken in de directe weerkaatste lichtbundel omslaan. Het feit dat er een Brewster hoek zou kunnen bestaan voor een fotonisch kristal plak is een interessante ontdekking.

In hoofdstuk 5 onderzoeken we licht dat uit een optische puntbron komt, in een drie-dimensionaal fotonisch kristal wordt ingekoppeld en daar vervolgens doorheen beweegt om tenslotte aan de ander kant van het kristal weer te worden uitgekoppeld. Om de overdracht van dit licht te meten gebruiken we de NSOM. Voor verschillende frequenties wordt er een ruimtelijke afhankelijkheid van deze overdracht gevonden. Zo is voor hoge frequenties de overdracht groter, als het tipje boven een bolletje staat dan als het tipje zich tussen de bolletjes bevindt. Andersom komt voor lage frequenties meer licht door het kristal als de tip tussen de bolletjes is dan wanneer ze er bovenop staat. Als er zich een defect in het <111> oppervlak bevindt, dan wordt de lokale inkoppeling van het licht sterk beïnvloed. Het onderzoek laat zien, dat voor lage frequenties (behalve voor een frequentie in het verboden band) meer licht in het kristal kan worden gekoppeld. Voor hoge frequenties, en ook voor de frequenties in het verboden band, wordt er minder licht ingekoppeld. De nabije-veld methode laat zien, dat zelfs defecten die in een paar lagen onder het oppervlak zitten nog een invloed op de koppeling hebben.Verder zijn er retractie- en naderingscurven voor verschillende frequenties gemeten. Ook daar zijn indicaties voor het effect van de eerste orde verboden frequentie band op de lichtkoppeling te vinden. Zo is voor een frequentie in het verboden band de afval van het nabije-veld twee keer langer dan voor andere frequenties. Bovendien laten Fabry-Perot oscillaties een grotere modulatie zien voor frequenties rond het verboden band; er wordt dus meer licht weerkaatst. De NSOM geeft nieuwe informatie over hoe het licht van een puntbron aan een drie-dimensionaal kristal koppelt.

In dit proefschrift zijn verschillende mogelijkheden beschreven om de optische eigenschappen van een fotonisch kristal te onderzoeken. Het locale meten van lichtvelden en de optische fase maken het mogelijk om verliezen en de effectieve brekingsindex van het materiaal te bepalen. Bovendien zijn er interferentie fenomenen zoals fase- singulariteiten en -sprongen onderzocht. Beide technieken, de locale nabije-veld methode en de ruimtelijk middelende verre-veld methode, zijn gebruikt om koppeling van licht met een fotonisch kristal te onderzoeken. Wij ontdekken, dat de koppeling naar resonante modi met een teken omslag van de koppelingparameter q kan worden verklaard met een soort Brewster hoek. Verder vinden we, dat de koppeling van licht uit een puntbron naar een drie-dimensionaal kristal niet alleen ruimtelijke afhankelijkheid heeft, maar ook van de optische frequentie afhangt. Deze koppeling wordt sterk beïnvloed als er een lokaal defect in het kristal is.

Zusammenfassung

Photonische Kristalle sind eine neue Sorte von Materialien, deren Brechungsindex mindestens entlang einer Richtung periodisch variiert (Gitter). Die optischen Eigenschaften von Licht (elektromagnetische Wellen) mit einer Wellenlänge von der Grössenordnung der Gitterkonstante sind somit direkt abhängig von der Kristallgeometrie. Die Periodizität des Brechungsindexes verursacht eine so genannte Bandstruktur mit verbotenen Frequenzbändern, in einer oder mehreren Richtungen, für welche das Licht perfekt reflektiert wird. Die Erforschung lokaler optischer Eigenschaften wird durch Nahfeldmethoden ermöglicht, welche das sich im Kristall befindende Licht messen können. Mit dieser Methode kann der direkte Einfluss der Kristallgeometrie auf die Ausbreitung des Lichtes gemessen werden. Im Gegensatz zu solch lokalen Messtechniken liefern Fernfeldmethoden ein räumlich gemitteltes optisches Signal. Zum Beispiel können die Qualität des Kristalls sowie Effekte von verbotenen Frequenzbändern mit Reflektionsmessungen bestimmt werden. Die mit den zwei komplementären Messtechniken errungenen Erkenntnisse, Nahfeld- und Fernfeldmethode, liefern ein Gesamtbild der optischen Eigenschaften der photonischen Kristalle.

In Kapitel 1 wird eine Einführung in die Theorie der photonischen Kristalle gegeben. Anhand des einfachen Beispiels eines unendlich ausgedehnten, eindimensionalen photonischen Kristalls wird die Bandstruktur erklärt, welche die optischen Eigenschaften des Lichtes im Material beschreibt. Danach werden zwei spezielle Strukturen, eine freihängende zweidimensionale photonische Kristallmembran und ein dreidimensionaler Kristall, aufgebaut aus Latexkugeln, erläutert. Im zweiten Teil des Kapitels werden die Methoden diskutiert, womit die Kristalle, die in dieser Arbeit untersucht worden sind, hergestellt wurden. Für die Fabrikation von verschiedenen Strukturen von jeglicher Grösse (im Nanometerbereich) und Form und in gewünschter periodischer Anordnung, wird ein fokussierter Ionenstrahl (FIB) genutzt. Die hochenergetischen Ionen prallen auf die Oberfläche und schiessen Material weg. Somit kann eine Struktur bestehend aus einer periodischen Anordnung von zwei verschiedenen Materialien (z.B. Luft und Glas) hergestellt werden. Zur Herstellung von grossflächigen und vor allem zweidimensionalen Kristallen werden

meistens holographische Methoden genutzt. Mit diesen wird der Photoresist belichtet und mit weiteren Verarbeitungsvorgängen kann eine freihängende Membran mit periodisch angeordneten Löchern hergestellt werden. Die dreidimensionalen Kristalle bestehen aus Latexkugeln, die selber einen Kristall formen. Die Kristalle weisen ein dicht gepacktes Gitter (flächenzentriert kubisch) auf und zeigen verbotene Frequenzbänder in verschiedenen Kristallrichtungen.

Photonische Kristalle können mit verschiedenen Methoden, Nahfeld- und Fernfeldmethoden, untersucht werden. Meistens befinden sich beide, Detektor und Lichtquelle, im fernen Feld. Wir haben solche Fernfeldmethoden genutzt um die verbotenen Frequenzbänder sowohl in der zweidimensionalen photonischen Kristallmembran als auch im dreidimensionalen Kristall zu vermessen. Ausserdem wurde eine vom Einfallswinkel des Lichtes abhängige Reflektionsmethode genutzt, um Licht an so genannte resonante Kristallmoden der photonischen Kristallmembran zu koppeln. Desweiteren werden in dieser Dissertationsarbeit zwei verschieden Nahfeldmethoden angewandt: ein "photon scanning tunnelling microscope (PSTM)" und ein "near-field scanning optical microscope (NSOM)". In der ersten Methode wird eine zugespitzte Glasfaser als Detektor genutzt, in der zweiten Methode dient sie als punktförmige Lichtquelle. Die Herstellung der nahfeld Glasfasern (Spitzen) wird beschrieben. Danach werden die zwei Nahfeldmethoden im Detail erklärt. In beiden Messaufstellungen ist ein dreidimensionaler Messmodus eingebaut, so dass Näherungs- und Zurückziehkurven gemessen werden können. Als Besonderheit ist es mit unserem PSTM möglich, die Phase des Lichtes in einem Material zu messen. Somit werden zugleich drei Signale detektiert: die Intensität und die Phase des Lichtes in der Struktur sowie die Topographie der Struktur.

In Kapitel 3 werden verschieden mit FIB hergestellte eindimensionale photonische Strukturen mit dem PSTM untersucht. Das optische Feld von Licht rund um 15 Löcher und 15 Schlitze in einem Wellenleiter wird gezeigt. Wir finden eine stehende Welle im Wellenleiter vor der periodischen Struktur, die durch Interferenz zwischen einkommendem und reflektiertem Licht aufgebaut wird. In der Struktur selber nimmt die Intensität ab. Der Verlust des Lichtes durch die Struktur kann positionsabhängig bestimmt werden. Der Abfall der Intensität in der Struktur zeigt eine Wellenlängenabhängigkeit. Wir finden, dass die Intensität schneller abnimmt für kürzere Wellenlängen als für längere. Diese Verhalten lässt vermuten, dass die Verluste durch Beugung erzeugt werden. Hinter den 15 Schlitzen wird ein unerwarteter wellenlängenabhängiger Wiederaufbau der Intensität im Wellenleiter beobachtet. Auch hier ist Interferenz verantwortlich für dieses aperiodische Intensitätsmuster des Lichtes. Die Interferenz entsteht zwischen Licht, welches sich durch die periodische Struktur hindurch ausbreitet und Licht, welches am unterliegenden Substrat reflektiert wird. Die Tatsache, dass Licht am Substrat reflektiert wird und somit den photonischen Kristall umgeht, ist eine wichtige Erkenntnis für die Silizium-auf-Isolator Technologie, da photonische Kristalle basierend auf dieser Technologie Übersprachеffekte aufweisen könnten. Als nächster Schritt wurde die Phase des Lichtes rund um 15 Löcher in einem Wellenleiter gemessen. Im Bereich der Löcher verändert die lokale Phase wegen der Änderung des Brechungsindexes (Luft anstelle Glas). Allgemein sieht man, dass die Löcher das Licht in Kugelwellen zurückstreuen. Diese Kugelwellen interferieren mit dem einkommenden Licht, wodurch ein komplexes Phasenmuster mit Singularitäten und Sprüngen hervorgerufen wird. Anhand der gemessenen komplexen Intensitäts- und Phasenmuster wird die Wichtigkeit der Nahfeldmethoden (PSTM) deutlich, denn für Fernfeldmethoden bleiben diese Informationen des Lichtes verborgen. Im letzten Abschnitt von Kapitel 3 wird die dreidimensionale Messmöglichkeit demonstriert. Am Beispiel von Lichtbeugung an zwei Schlitzen werden abfallende (evanescente) und laufende Wellenanteile voneinander getrennt. Die dreidimensionale Messtechnik ermöglicht es, die Entstehung von Phasensingularitäten zu beobachten. Für einen Wellenleiter der 4 Moden leitet, bilden wir die Entstehung von zwei gekoppelten Singularitäten für zunehmenden Spitze zu Substrat Abstand ab.

In Kapitel 4 wird eine freihängende photonische Kristallmembran mit Fernfeldmethoden untersucht. Die Messmethode ermöglicht die Kopplung von einfallendem Licht an resonante Moden der Membran. Wird ein solcher Mode angeschlagen, ist ein schmales Kennzeichen im Reflexionsspektrum zu erkennen. Ein solches Kennzeichen wird durch Interferenz zwischen Licht, welches verschieden optische Wege zurücklegt, hervorgerufen. Die zwei verschiedenen optischen Wege sind die direkte Reflektion des Lichtes an der Membran und Reflektion von Licht, welches für kurze Zeit an einen resonanten Mode koppelt. Aus der Frequenzposition des Kennzeichens kann ein Teil der Bandstruktur der photonischen Kristallmembran rekonstruiert werden. Wir finden eine ausgezeichnete Übereinstimmung der Messresultate mit Simulationen. In der zweiten Hälfte von Kapitel 4 wird die Form des Kennzeichens genauer untersucht. Dafür wenden wir eine Theorie an, welche ursprünglich für inelastische Streuung von Elektronen an einem Heliumatom entwickelt wurde. Wir haben diese Theorie für Photonen (Licht) umgeschrieben und können damit die Messdaten beschreiben. Wir finden, dass die Kennzeichen sehr schmal sind, was auf eine hohe Qualität der Struktur zurückschliessen lässt. Zusätzlich führt die Theorie einen Kopplungsparameter q ein, welcher als das Verhältnis zweier Übergangswahrscheinlichkeiten definiert ist. Für parallel (TM) polarisiertes Licht beobachten wir eine Umkehrung des Vorzeichens von q. Die Umkehrung bedeutet, dass sich die Phase in einem der zwei optischen Wege ändert. Eine mögliche Erklärung wäre eine Phasenänderung von Licht im direkt reflektierten optischen Weg. Wenn der Einfallswinkel von Licht durch den sogenannten Brewster-Winkel gedreht wird, ändert sich die Phase von TM polarisiertem Licht. Bemerkenswert ist, dass unsere mögliche Erklärung die Annahme eines effektiven Brechungsindexes und eines Brewster-Winkels für eine photonische Kristallmembran macht.

In Kapitel 5 untersuchen wir die Übertragung von Licht aus einer punktförmigen Lichtquelle, welches in einen dreidimensionalen Kristall eingekoppelt wird, sich darin fortpflanzt und schliesslich auf einen Detektor im Fernfeld fällt. Diese Übertragung ist mit dem NSOM für verschiedene Wellenlängen (optische Frequenzen) gemessen worden. Für hohe Frequenzen wird das Licht besser in den Kristall gekoppelt, wenn die NSOM Spitze sich über einer Kugel befindet. Für tiefe Frequenzen beobachten wir das Umgekehrte, mehr Licht kommt durch den Kristall wenn die Spitze zwischen den Kugeln ist. Wenn sich ein Defekt in der Kristalloberfläche befindet, wird die lokale Kopplung vom Licht stark beeinträchtigt. Für tiefe Frequenzen (ausgenommen Frequenzen im verbotenen Frequenzband) wird mehr Licht durch den Defekt in den Kristall gekoppelt, für hohe Frequenzen und für Frequenzen im verbotenen Frequenzband wird wenig Licht an der Stelle des Defekts in den Kristall gekoppelt. Ausserdem beobachten wir, dass es möglich ist mit einem NSOM Defekte, welche sich einige Lagen unter der Kristalloberfläche befinden, aufzuspüren. Untersuchungen der Nahfeldkopplung in Näherungs- und Zurückziehkurven weisen auf verbotene Frequenzbänder hin. Für Frequenzen im verbotenen Frequenzband finden wir einen zweimal längeren exponentiellen Abfall des Lichtes gegenüber dem Abfall von Licht mit andere Frequenzen. Ausserdem zeigen die Kurven eine grössere Amplitudenmodulation für Frequenzen rund um das verbotene Frequenzband. Die Nahfeldmethode erlauben Untersuchungen des komplexen Kopplungsmechanismus von Licht zu einem dreidimensionalen photonischen Kristall.

In dieser Dissertationsarbeit beschreiben wir verschiedene optische Eigenschaften von photonischen Kristallstrukturen. Durch Beobachtungen der lokalen Fortpflanzung des Lichtes können Verluste in Intensität und Brechungsindex des Materials bestimmt werden. Messungen der Phase des Lichtes enthüllen ein komplexes Netzwerk von Interferenzen, wodurch unter anderem Phasensingularitäten entstehen. Beide Methoden, Nahfeld und Fernfeld, wurden genutzt zur Untersuchung der Kopplung des Lichtes in einen photonischen Kristall. Resonante Moden, welche in zweidimensionalen Kristallen angeschlagen werden können, zeigen eine sogenannte q-Umkehrung des Kopplungsparameters q. Die Nahfeldkopplung von Licht aus einer punktförmigen Lichtquelle ist orts- und frequenzabhängig. Diese Kopplung kann durch Kristalldefekte stark beeinflusst werden.